

Quantitative Electron Tomography for Nanostructured Materials

KWANTITATIVE ELEKTRONEN TOMOGRAFIE AAN NANOGESTRUKTUREERDE MATERIALEN

(met een samenvatting in het Nederlands)

PROEFSCHRIFT

ter verkrijging van de graad van doctor aan de Universiteit Utrecht
op gezag van de rector magnificus, prof. dr. J.C. Stoof, ingevolge het
besluit van het college voor promoties in het openbaar te verdedigen
op woensdag 26 augustus 2009 des ochtends te 10:30 uur

door

HEINER FRIEDRICH

geboren op 1 juli 1974, te Chemnitz, Duitsland

Promotoren: Prof. dr. ir. K. P. de Jong

Prof. dr. A. J. Verkleij

Co-promotor: Dr. P. E. de Jongh

Dit onderzoek werd gefinancierd door de NRSCC (National Research School
Combination Catalysis).

“What we observe is not nature in itself but nature exposed to our method of questioning.”

Werner Heisenberg

ISBN: 978-90-393-5110-9

Printed by Gildeprint Drukkerijen BV.

Contents

1. General Introduction	7
2. Electron Tomography for Heterogeneous Catalysts and Related Nanostructured Materials	11
3. An Electron Tomography Study of NiO supported on SBA-15 obtained by thermal Decomposition of Nickel Nitrate in different Gas Atmospheres.	45
4. Measuring Location, Size, Distribution, and Loading of NiO Crystallites in Individual SBA-15 Pores by Electron Tomography	63
5. Quantifying the 3D Structure of Nanomaterials by Threshold-based Segmentation of Electron Tomograms.	77
6. Quantitative Structural Analysis of Binary Nanocrystal Superlattices by Electron Tomography	101
7. Summary and Outlook	123
Samenvatting	126
Appendix	129
List of publications	141
Acknowledgements	143
Curriculum vitae	145

Chapter 1

General Introduction

1.1 Nanostructured Materials

The controlled assembly of materials on the nanoscale has been a major focus of research across many scientific disciplines.¹⁻⁶ Important representatives of nanostructured materials are catalysts which are nowadays involved in the industrial manufacture of approximately 80% of all chemical products.⁷ A catalyst is a substance that when added to a reaction mixture increases the rate of the reaction without being consumed. Depending on whether a catalyst exists in the same phase as the reactants it is classified as homogeneous (in the same phase) or heterogeneous (in a different phase). Most heterogeneous catalysts are solids while the reactants are in the liquid or gas phase. In supported heterogeneous catalysts, the active components such as transition metals and metal oxides are finely dispersed on a high surface area support to maximize the number of catalytically active sites per unit mass of material. The high surface area support anchors the active components to prevent sintering at elevated temperatures. Furthermore, the support material itself can contribute to the catalytic activity of the combined system. Today, most solid catalysts can be considered as complex three-dimensional (3D) nanostructured materials.

While classical concepts like maximizing the surface area of a catalyst by decreasing the particle size are often applied, the nanometer dimension concerns a size range in which a gradual transition from condensed matter to molecular structures occurs.⁸ Recent interest in nanostructured materials originates from phenomena such as the quantum size effect, bridging the gap between the discrete density of states in atoms/molecules and the continuous band structure of the bulk solid.⁹ In the nanometer size range, materials characteristics can be tuned not only by composition but more importantly by size and shape of constituent phases, giving rise to exceptional optical^{10,11}, magnetic^{12,13}, electric^{14,15}, mechanical¹⁶ and catalytic^{17,18} properties. Judging from the multitude of participating research areas, the nanoscale seems to be the length scale at which science has become truly interdisciplinary.¹⁹ To gain insight into the relation between a structure and its properties, dedicated characterization techniques are required that provide detailed 3D information with nanometer resolution.²⁰⁻²² One of the most promising and rapidly developing techniques, in this respect, is electron tomography (ET), a method for obtaining 3D structural information from a series of electron micrographs. ET delivers a resolution of approximately 1 nm, intermediate to that of atom probe tomography²³ (<0.3 nm) and X-ray tomography²⁴ (~ 50 nm), which makes it ideal for the 3D characterization of nanostructure materials.^{25,26} A strong advantage of ET is that it does not analyze the spatial Fourier Transform, as in electron crystallography,²⁷ and thus can resolve truly unique 3D morphologies. Furthermore, being able to resolve the local morphology of materials offers the possibility to extract quantitative information on constituent phases.

1.2 Scope and Outline

The research described in this thesis focused on the development of ET towards a quantitative imaging tool for nanostructured materials. For this purpose ET experiments were performed on a range of nanostructures which were subsequently quantified by image analysis. In **chapter 2** the general methodology of ET is presented with particular emphasis on the basic principle, resolution, workflow, and imaging modes. Besides introducing the technical aspects of ET, applications are reviewed following the materials classes of zeolites, ordered mesoporous materials, disordered oxide supported catalysts, carbon materials, and miscellaneous materials (ceramics, polymers, and nanocomposites). **Chapters 3 and 4** address the preparation of heterogeneous catalysts to gain a better understanding of how thermal treatments, commonly referred to as calcination, affect the final distribution of active components. To this end NiO particles supported on ordered mesoporous silica SBA-15, prepared by thermally decomposing nickel nitrate inside the pores of the support in air, He, and NO/He atmospheres, were investigated. ET provided structural insight into the NiO size, distribution, and overall morphology as a function of the gas atmosphere. Microscopic observations on the level of individual SBA-15 mesopores are discussed in context of bulk characterization by N₂-physisorption and X-ray diffraction. In **Chapter 5** a criterion for automated threshold-based segmentation of electron tomograms is proposed. Experiments on a model system of colloidal gold particles, complemented by numerical simulations of the imaging and reconstruction process, demonstrate the achievable accuracy in measuring particle sizes down to 1 nm. The suitability of the method for nanostructured materials is tested on ruthenium/carbon nanotube and gold@zirconia catalysts. **Chapter 6** deals with the quantitative structural analysis of binary nanoparticle superlattices. Electron tomograms were analyzed in terms of particle positions, sizes, nearest neighbor distances, crystallographic ordering and lattice defects. Furthermore, an anisotropic deformation of some nanocrystal superlattices after drying and clues to the crystallization pathway were also found. ET results on four superlattices consisting of thousands of PbSe, CdSe and Au nanoparticles (all less than 10 nm in size) illustrate the versatility of the method. The thesis ends with **chapter 8** that presents a summary and outlook.

References

- (1) Treacy, M. M. J.; Newsam, J. M. *Nature* **1988**, *332*, 249.
- (2) Iijima, S. *Nature* **1991**, *354*, 56.
- (3) Kresge, C. T.; Leonowicz, M. E.; Roth, W. J.; Vartuli, J. C.; Beck, J. S. *Nature* **1992**, *359*, 710.
- (4) Zhao, D. Y.; Feng, J. L.; Huo, Q. S.; Melosh, N.; Fredrickson, G. H.; Chmelka, B. F.; Stucky, G. D. *Science* **1998**, *279*, 548.
- (5) de Jong, K. P.; Geus, J. W. *Cat. Rev. - Sci. Eng.* **2000**, *42*, 481.
- (6) Lin, Y.; Boker, A.; He, J. B.; Sill, K.; Xiang, H. Q.; Abetz, C.; Li, X. F.; Wang, J.; Emrick, T.; Long, S.; Wang, Q.; Balazs, A.; Russell, T. P. *Nature* **2005**, *434*, 55.

- (7) van Santen, R. A.; van Leeuwen, P. W. N. M.; Moulijn, J. A.; Averill, B. A.; (Eds.) *Catalysis: An Integrated Approach, Second, Revised and Enlarged Edition*; Elsevier: Amsterdam, 1999.
- (8) Ostwald, W. *Die Welt der vernachlässigten Dimensionen*; 7th and 8th ed.; Verlag von Theodor Steinkopff: Dresden und Leipzig 1922.
- (9) Weller, H. *Angew. Chem., Int. Ed.* **1993**, *32*, 41.
- (10) Murray, C. B.; Norris, D. J.; Bawendi, M. G. *J. Am. Chem. Soc.* **1993**, *115*, 8706.
- (11) Rogach, A. L.; Katsikas, L.; Kornowski, A.; Su, D.; Eychmüller, A.; Weller, H. *Ber. Bunsen Ges. Phys. Chem. Chem. Phys.* **1997**, *101*, 1668.
- (12) Chen, Q.; Zhang, Z. *J. Appl. Phys. Lett.* **1998**, *73*, 3156.
- (13) Salabas, E. L.; Rumpelcker, A.; Kleitz, F.; Radu, F.; Schüth, F. *Nano Lett.* **2006**, *6*, 2977.
- (14) Talapin, D. V.; Murray, C. B. *Science* **2005**, *310*, 86.
- (15) Urban, J. J.; Talapin, D. V.; Shevchenko, E. V.; Kagan, C. R.; Murray, C. B. *Nat. Mater.* **2007**, *6*, 115.
- (16) Champion, Y.; Langlois, C.; Guerin-Mailly, S.; Langlois, P.; Bonnetien, J. L.; Hytch, M. J. *Science* **2003**, *300*, 310.
- (17) Haruta, A. *Chem. Rec.* **2003**, *3*, 75.
- (18) Bezemer, G. L.; Bitter, J. H.; Kuipers, H. P. C. E.; Oosterbeek, H.; Holewijn, J. E.; Xu, X. D.; Kapteijn, F.; van Dillen, A. J.; de Jong, K. P. *J. Am. Chem. Soc.* **2006**, *128*, 3956.
- (19) Mathur, N. *Nature* **2002**, *419*, 573.
- (20) Koster, A. J.; Ziese, U.; Verkleij, A. J.; Janssen, A. H.; de Jong, K. P. *J. Phys. Chem. B* **2000**, *104*, 9368.
- (21) Weyland, M.; Midgley, P. A.; Thomas, J. M. *J. Phys. Chem. B* **2001**, *105*, 7882.
- (22) de Jong, K. P.; Koster, A. J. *Chemphyschem* **2002**, *3*, 776.
- (23) Kelly, T. F.; Miller, M. K. *Rev. Sci. Instrum.* **2007**, *78*, 031101.
- (24) Withers, P. J. *Mater. Today* **2007**, *10*, 26.
- (25) Midgley, P. A.; Weyland, M. *Ultramicroscopy* **2003**, *96*, 413.
- (26) Möbus, G.; Doole, R. C.; Inkson, B. J. *Ultramicroscopy* **2003**, *96*, 433.
- (27) Sakamoto, Y.; Kaneda, M.; Terasaki, O.; Zhao, D. Y.; Kim, J. M.; Stucky, G.; Shin, H. J.; Ryoo, R. *Nature* **2000**, *408*, 449.

Chapter 2

Electron Tomography for Heterogeneous Catalysts and Related Nanostructured Materials

Abstract

One of the most promising and rapidly developing techniques for the three-dimensional (3D) structural analysis of heterogeneous catalysts is electron tomography (ET). This chapter presents the general methodology of ET with particular emphasis on the basic principle, resolution, workflow, and imaging modes. Furthermore, applications to heterogeneous catalysts and related nanostructured materials are reviewed following the materials classes of zeolites, ordered mesoporous materials, disordered oxide supported catalysts, carbon materials, and miscellaneous materials (ceramics, polymers, nanocomposites).

Adapted with permission from H. Friedrich, P.E. de Jongh, A. J. Verkleij, and K. P. de Jong, *Electron Tomography for Heterogeneous Catalysts and Related Nanostructured Materials*. Chem. Rev. **2009**, *109*, 1613-1629. Copyright 2009 American Chemical Society.

2.1 Introduction

The full potential in catalyst development will only be realized if characterization techniques are available that can probe materials with sub-nanometer resolution. One of the most employed techniques to image heterogeneous catalysts at the nanometer and sub-nanometer scale is transmission electron microscopy (TEM). As suggested by the name, TEM uses electrons transmitted through the object for imaging. Since the interaction between electrons and matter is very strong, only thin parts, commonly much less than a micron in thickness, are imaged. Since heterogeneous catalysts are in most cases structured on a much smaller length scale, the sample thickness can be reduced to TEM requirements by appropriate preparation techniques, and is therefore no limitation.

The major advantage of electron microscopy is that a variety of modes to probe the sample can be employed, of which conventional TEM (TEM), diffraction mode, scanning TEM (STEM), and spatially resolved elemental analysis are only a few examples. For a detailed description of available TEM techniques we refer to the books by Williams & Carter¹, Reimer², and Yao & Wang³. Focusing on the use of electron microscopy in heterogeneous catalysis, the book by Gai & Boyes⁴ provides a wealth of information. Shorter reviews focusing on catalysis related applications of TEM⁵⁻¹⁰, environmental TEM¹¹, and electron energy-loss spectroscopy¹² are also available.

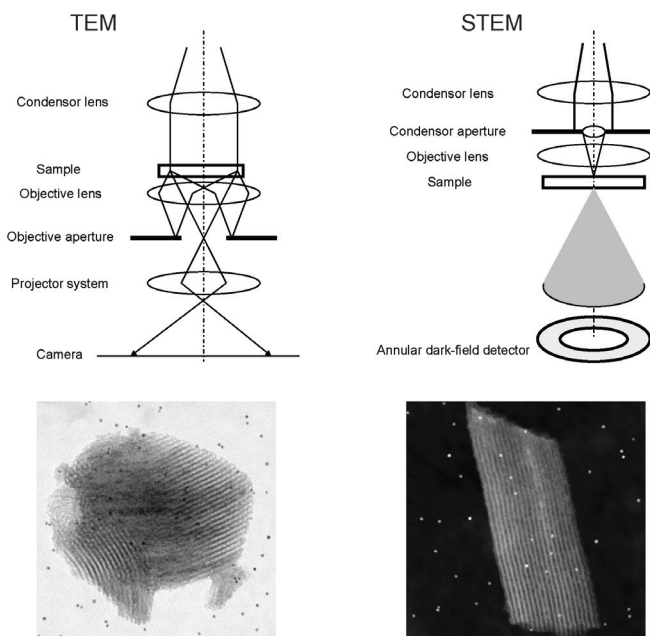


Figure 1 Schematic beam path in TEM and STEM. The images below, acquired in the corresponding imaging mode, show SBA-15 particles on a carbon support film with 5 nm gold spheres attached.

The principal beam paths for imaging in TEM and STEM mode are sketched in Figure 1. In TEM the sample is probed by a parallel electron beam, resulting in a bright-field image. Electrons that are scattered onto the contrast forming objective aperture blade are removed from the beam and will not be recorded in the image. Thus, thick objects and objects of high mass-density will appear dark in such an image (scattering or absorption contrast). In STEM a focused electron beam is rastered across the sample. The electrons recorded at each point of the raster then form the image. When a ring detector (annular dark-field detector) is used to collect deflected electrons, thick objects and objects of high mass-density will appear bright in such images. This scheme explains the most basic connection between contrast in an image and the imaged structure. Other sources of contrast, which may dominate depending on the nature of the specimen, include diffraction contrast (associated with the orientation of a crystalline specimen with respect to the electron beam) and TEM phase contrast (tunable by defocusing). When going from nanometer resolution to atomic details only accurate control of beam condition, sample orientation, and defocus setting yields interpretable results.

The above paragraph already hints towards one of the difficulties when interpreting TEM and STEM images. Since images are a two-dimensional (2D) representation of an originally three-dimensional (3D) structure it is hard to distinguish between thick objects and objects of high mass-density (e.g. metals). Nevertheless, in some cases it is possible to extract sample thickness or chemical information.¹² This should not distract from the fact that the resolution in the third dimension is usually not better than the thickness of the sample, which might be several hundred nanometers. Thus, from a single image the position of a metal particle with respect to its support, e.g. on the surface or on the inside, can only be inferred in rare cases. To overcome the issue, two or more images¹³⁻¹⁵ or serial sectioning of the sample by microtomy¹⁶ have been applied. Recent developments in optical sectioning by aberration-corrected STEM, which is in a way similar to confocal optical microscopy, hold great promise for the future.¹⁷ For samples with a periodic architecture, electron crystallography can elucidate the 3D structure accurately.^{5,7,18,19}

A general approach to 3D imaging of complex materials with a non-periodic 3D structure is provided by electron tomography (ET). The growing importance of ET has been previously reviewed with emphasis on materials science^{20,21}, biological sciences²²⁻²⁵, and in context with other nanotomographic techniques.^{26,27} This review presents, after introducing the technical aspects of ET, a comprehensive overview to the rapidly emerging field of ET for the study of heterogeneous catalysts and related nanostructured materials. Chapters are organized following the materials classes of zeolites, ordered mesoporous materials, disordered oxide supported catalysts, carbon materials, and miscellaneous materials (ceramics, polymers, nanocomposites).

2.2 Technical Aspects

In ET a series of 2D images (commonly 50-150 images) is collected by tilting the specimen in the electron beam and recording an image at each tilt step. Subsequently the series of images (tilt-series) is aligned with respect to a common origin and tilt axis. Finally, the 3D morphology of the object is reconstructed using numerical algorithms. Details of the workflow from data acquisition to visualization are given in section 2.2.3, page 17.

2.2.1 Basic principle

The mathematical framework underlying tomography was developed by Johan Radon and forms the basis for what has come to be known as the Radon transform.²⁸ It applies to many situations where it is practicable to determine structural properties of an object from data that leave the object complete, e.g. by using transmitted waves or particles.²⁹ Applications range from X-ray tomography^{30,31} to electron tomography in catalysis.^{32,33} The Radon transform maps a real space object by its projections, which is equivalent to probing of a sample by a transmitted signal such as an electron beam. From these projections the object structure can be reconstructed by applying the inverse Radon transform. To which extend TEM and STEM images can be considered to be projections will be discussed in section 2.2.4, page 20.

For a more intuitive understanding, a connection between the information in a series of projections and the 3D object structure is needed. To highlight this connection we make use of the close relationship between the probably better known Fourier transform and the Radon transform. It can be shown that the Fourier transform of a 2D projection is equal to a central slice through the 3D Fourier transform of the object. For a detailed discussion of this theorem, the Projection-Slice Theorem, we refer to the book by Deans.²⁹ A schematic representation of the tomographic reconstruction using the Projection-Slice-Theorem is depicted in Figure 2. By combining multiple projections, i.e. multiple central slices at different tilts, the 3D Fourier space of the object is sampled, and an inverse Fourier transform reconstructs the 3D object.

First strides towards tomography using electron micrographs date back to 1968.³⁴⁻³⁶ Historically the application of ET has been the domain of biology where it is used to image the 3D structure of molecules to entire cells.²²⁻²⁴ In the last decade, the range of materials studied by ET has extended dramatically. Enabling factors include the availability of large-area CCD cameras and microscope automation.³⁷ Nowadays a number of academic and commercial tools for automated data acquisition exist, such as, UCSF tomography³⁸, SerialEM³⁹, TOM software toolbox⁴⁰, EMMenu (TVIPS GmbH, Gauting, Germany), Xplore3D (FEI company, Eindhoven, The Netherlands), TEMography (JEOL Ltd., Tokyo Japan), and Digital Micrograph 3D ET (Gatan Inc., Pleasanton, USA).

With the increasing diversity of samples examined by ET, imaging modes other than bright-field TEM gain importance. Which mode to choose, e.g. TEM vs. STEM, will depend upon the combination of material and scientific question. A comprehensive list of imaging modes that have been used for tomography is given in section 2.2.4, page 20. At present mainly bright-field (BF) TEM tomography and high-angle annular dark-field (HAADF) STEM tomography are applied for studying catalysis-related nanostructured materials.

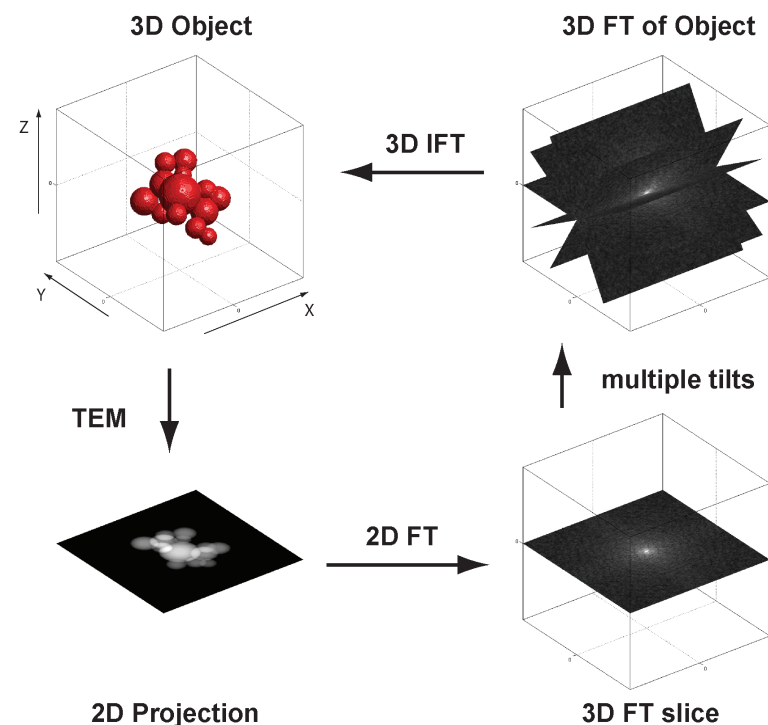


Figure 2 ET reconstruction scheme using the Projection-Slice-Theorem. FT denotes the Fourier Transform, and IFT denotes the Inverse Fourier Transform. By combining projections recorded at multiple tilts (here shown for single-axis tilting around X) the 3D FT of the object is probed. An inverse Fourier Transform then reconstructs the 3D object.

2.2.2 Resolution

In principle, electron tomograms can be reconstructed from any set of projections taken along different directions. However, mechanical and technical constraints prevent accurate and reproducible sample movement with six degrees of freedom thus limiting the variety of practicable data acquisition schemes. At this point it has to be noted that the applied data acquisition scheme largely determines the obtainable resolution. Here we will restrict the discussion to single-axis tilting, although alternative approaches, such as, conical tilting⁴¹, and dual-axis tilting^{42,43} are also employed.

In single-axis tilting the object is tilted in increments about the rotation axis of the microscope goniometer from one extreme of the tilt range to the other, e.g. from -70° to $+70^\circ$. Assuming a perfect alignment, the resolution along the rotation axis (x-axis in Figure 2) is equal to the resolution in the original micrographs. The resolution in the direction perpendicular to the holder and beam axis (y-axis in Figure 2) is determined by the number of projections, N , and the diameter, D , of the reconstructed volume:⁴⁴

$$d_y = \frac{\pi D}{N} \quad (1)$$

Equation 1, referred to as Crowther criterion, assumes that the images are acquired over a range of ± 90 degrees. The resolution parallel to the beam direction (z-axis in Figure 2) is further affected as a result of the limited tilt range of the microscope goniometer or shadowing of the imaged area by the sample holder at high tilt-angles. Angular limitations lead to a ‘missing wedge’ of information which causes an elongation (e_x) of the reconstruction point-spread function.⁴⁵ The elongation factor can be estimated from the maximum tilt angle (α) to:

$$d_z = d_y \cdot e_x = d_y \cdot \sqrt{\frac{\alpha + \sin \alpha \cos \alpha}{\alpha - \sin \alpha \cos \alpha}} \quad (2)$$

Based on the above equations and Figure 2 it becomes clear that increasing the tilt range while decreasing the tilt increment will improve the resolution. A graphical representation of the effect of tilt increment and maximum tilt angle on reconstruction results is given in Figure 3. In practice resolutions better than predicted by the Crowther criterion have been obtained, but not understood.^{20,46-49}

Alternatively to geometrical considerations as brought forward in the Crowther criterion, progress is made defining standards for resolution estimation.⁵⁰⁻⁵² Unfortunately, a straightforward quantitative verification of resolution is not available for electron tomography.²⁵

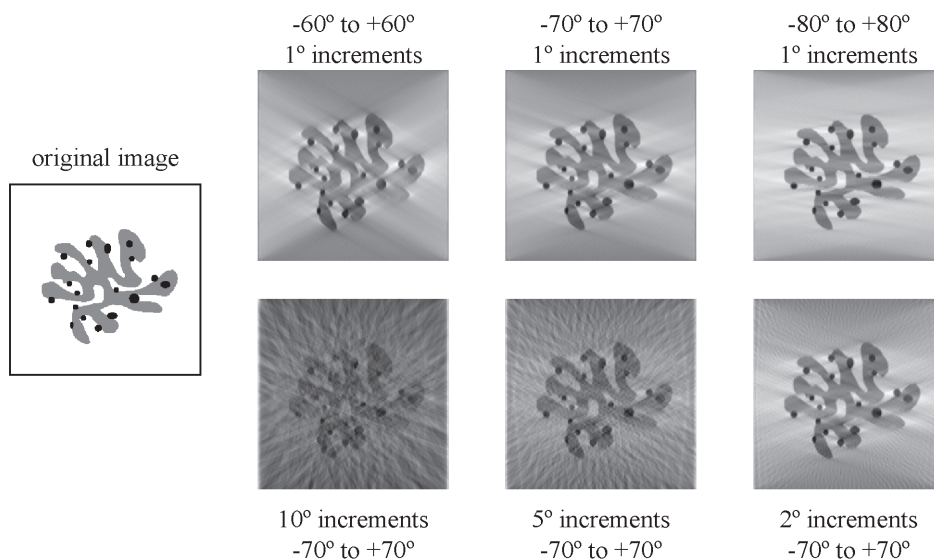


Figure 3 Effects of maximum tilt angle and tilt increment on the tomographic reconstruction. In general, increasing the maximum tilt angle and decreasing the tilt increment improves results. Bright zones to the left and right of dark objects result from the reconstruction point spread function (weighted backprojection) and dark zones on the bottom and top are caused by the limited maximum tilt angle.

2.2.3 Workflow

First, a few comments about sample holders and sample preparation are necessary. As a result of the high tilts required for ET, typically $\pm 70^\circ$, a high-tilt sample holder and a suitably prepared sample have to be used. The high-tilt sample holder allows for tilting of the specimen in the microscope to high angles without touching the objective lens pole piece or the objective aperture blade. Its construction also prevents shadowing of the viewable grid area by the holder edges. Single-tilt and tilt-rotate holders are commercially available.

The specimen grid should be chosen such that shadowing of the viewable area by the grid bars is minimal. In general, large mesh grids or parallel bar grids are best suited. In the first step, colloidal gold particles of 5 – 15 nm size, depending on the desired magnification, are deposited onto the TEM grid. The gold particles serve as markers and aid in the alignment of the tilt series. Gold markers are not mandatory but have proven to be a successful and straightforward approach.⁵³ In the second step the sample material is placed on the (carbon) support film in form of a fine powder or an ultra-microtome section.

Powders are commonly applied by ethanol suspension in an ultrasonic bath, subsequent application of a droplet of the suspension onto the grid, followed by drying. For ET samples dilute suspensions are favorable since a lower density of particles on the support film prevents shadowing by neighboring structures at high tilts. In case of microtome sections tilting to high angles causes the effective beam path through the sample to increase. One should keep in mind while cutting the sections that the effective path length at 70° tilt is approximately 3 times the section thickness.

Having the sample ready, further steps and parameters from tilt-series acquisition to visualization of final results are outlined in Figure 4. Acquisition is aided by automated corrections for specimen drift and focus during tilting.^{38-40,54} As discussed in section 2.2.2, increasing the tilt range while decreasing the tilt increment will improve results. For acquisition of the tilt-series three main parameters are important: tilt range ($\sim \pm 70^\circ$ or higher), tilt increments ($\sim 1^\circ$ to 3°) and electron dose commonly controlled by the image acquisition time ($\sim 1-4$ s in TEM and 10-80 s in STEM). Since beam settings (e.g. spot size, condenser aperture, etc.) may differ significantly between TEM and STEM, a comparison of applied electron doses based on the acquisition times alone is inappropriate. In fact, one has to calculate for the given settings the total number of electrons imparted on the sample per unit area throughout tilt series acquisition.

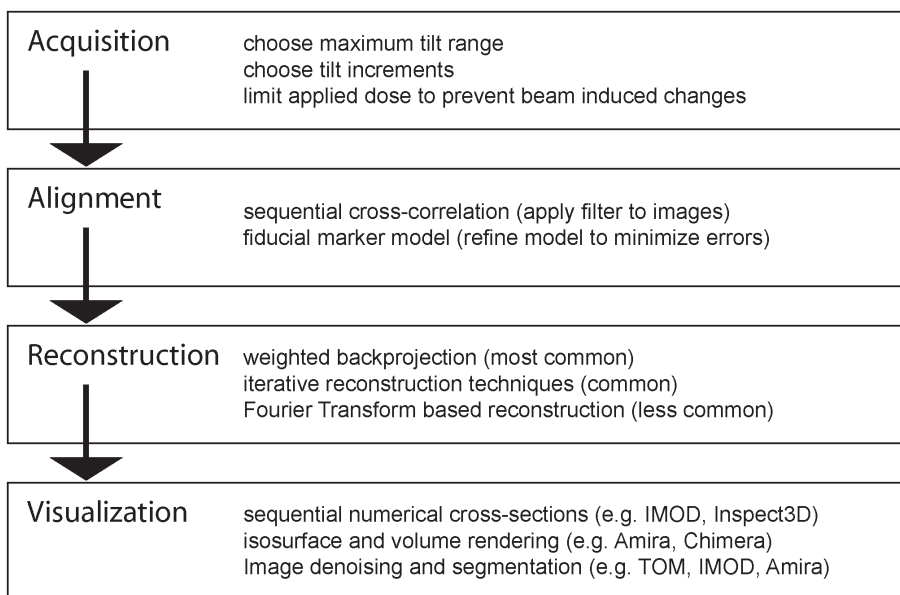


Figure 4 Workflow scheme.

The limiting factor for acquisition, in many cases, is electron beam induced damage to the specimen.^{55,56} Care has to be taken that changes in the specimen are negligible and do not hamper the reconstruction. This does, however, not preclude ET to be applied to beam sensitive materials such as frozen-hydrated (cryo) samples in life sciences. As pointed out by Hegerl and Hoppe in the dose fractionation theorem, the electron dose required to detect structural features at a given level of statistical significance and resolution is the same for 2D and 3D imaging.⁵⁷ More recent computer simulations confirmed that the theorem is applicable to realistic experimental conditions.⁵⁸ For a more detailed discussion of Cryo-ET we refer to the recent literature.^{25,59}

To conclude the comments on acquisition, a cautioning remark on the amount of data that is acquired and will have to be processed seems appropriate. One tilt series recorded on a 2048 x 2048 pixel CCD camera over an angular range of $\pm 70^\circ$ at 1° increments will have a file size of approximately 1.1 GB (8 MB \times 141 images).

While automated data collection is able to compensate for the major movements during acquisition, accurate alignment of the set of 2D images to a common origin and rotation axis has to be performed after data collection. Preceding alignment, TEM images are commonly corrected for pixels with unusually high values - "hot pixel" - that can be attributed to X-rays.⁶⁰ The two principal approaches to align a tilt series are alignment by cross-correlation⁶¹ and alignment by tracking fiducial markers, i.e. colloidal gold.⁵³ In case that the tilt-axis direction is known or can be determined, cross-correlation is a straightforward means for translational alignment. It is based on an overall match between image features common to two projections. To optimize results, appropriate numerical filters are employed to enhance image features that can be easily cross-correlated to each other and to reduce noise sensitivity.^{21,61}

Alignment by tracking fiducial markers determines both translational alignment and the tilt-axis direction.⁵³ For a set of gold markers, commonly 10-30, a fiducial model is generated by tracking their centers either manually or by automated procedures throughout the entire image series. This model is then used to determine relative shifts and rotations between images, by applying least square minimization.⁵³ In general, fiducial models from automated tracking have to be refined. Finally, by applying the translational and rotational corrections an aligned tilt series is obtained, from which the tomogram can be reconstructed.

Common academic and commercial software packages for alignment and reconstruction of ET data include IMOD⁶², TOM software toolbox⁴⁰, EMMenu (TVIPS GmbH, Gauting, Germany), Inspect3D (FEI company, Eindhoven, The Netherlands), TEMography (JEOL Ltd., Tokyo Japan), and Digital Micrograph 3D ET (Gatan Inc., Pleasanton, USA). Tomographic reconstruction is carried out using numerical algorithms of which weighted back-projection techniques (WBP) are most common.⁶³ With increasing processing speed of desktop computers, iterative methods gain importance.⁶⁴⁻⁷⁰ For a detailed discussion of reconstruction algorithms we refer to the literature.^{29,71}

The last step in the workflow is visualization of 3D results. This is a rather broad topic and approaches will differ depending on the structures under investigation or the imaging technique used. In general, the tomogram will contain intensity variations that are interpretable as variations in imaged object property, e.g. mass-density. Common ways of presenting 3D data include the display of consecutive numerical cross-sections as movie, rendering of a surface belonging to a specific intensity value, and rendering of the object volume with a color scheme where each color represents a certain range of intensities. While most of the above mentioned alignment and reconstruction software packages include tools for visualization, often dedicated programs such as UCSF Chimera⁷² and Amira (Mercury Computer Systems, Inc.) are utilized.

Another very interesting and relevant approach, that provides quantitative structural information from ET data, is image analysis by segmentation.⁷³⁻⁷⁵ Image segmentation is the process of dividing an image (here the tomogram) into its parts for further analysis. The type of analysis applied will differ depending on the scientific question, but can include the particle size distribution^{49,76}, the particle location^{77,78}, and the local curvature of surfaces^{56,79} of which examples will be given later in the article.

2.2.4 Imaging modes

Electron microscopy provides a variety of modes to probe the sample and as a result there are a considerable number of possible ET modes too. For a comprehensive overview, tested approaches are listed corresponding to the two most distinct modes for forming an image, i.e. parallel (TEM) or convergent (STEM) illumination, as outlined in Figure 1. For parallel illumination, bright-field (BF) ET^{32,33,49,78,80}, annular dark-field (ADF) ET⁸¹, energy-filtered (EF) ET^{20,82-86}, holographic ET⁸⁷⁻⁸⁹, weak-beam dark-field (WBDF) ET⁹⁰, and diffraction ET^{91,92} are reported in the literature. Using convergent illumination high-angle hollow-cone dark-field (HAADF) ET⁹³, annular dark-field (ADF) ET^{94,95}, energy-dispersive X-ray (EDX) ET⁸³, and high-angle annular dark-field (HAADF) ET^{20,96} have been applied. In the following we will restrict our discussion to BF TEM ET and HAADF STEM ET since they are the most common techniques for studying catalysts. An example of EF TEM ET will be given in section 2.3.4 on page 33.

For application to inorganic materials, care has to be taken that the images of the tilt-series fulfill the projection requirement mentioned in section 2.2.1, page 14. A detailed assessment of the validity for BF TEM ET is given by Hawkes.⁹⁷ It is concluded that for weakly scattering materials, where mass-thickness (absorption) is the dominant contrast mechanism, electron microscope images are essentially projections on which a tomographic reconstruction can be based. Alternatively, phase contrast images are used for very weakly scattering objects, such as unstained life science specimens and polymers. However, in the case of crystalline materials, where Bragg diffraction significantly contributes to image formation, BF ET has been suggested to be of only limited value.^{20,98} In contrast, many successful applications

of BF ET to crystalline materials are reported in the literature.⁹⁹⁻¹⁰² The observation that orientation, i.e. diffraction condition, dependent contrast does not strongly effect the tomographic reconstruction can be rationalized by the fact that diffraction contrast is only present in a few images of the tilt-series, while ET averages over a much larger number of images. An evaluation of the effect of Bragg diffraction on the reconstruction quality of BF TEM ET is given by Feng *et al.*¹⁰³ and a direct comparison of TEM and STEM reconstructions of a crystalline object by Friedrich *et al.*⁹⁴ As a rule of thumb, crystalline domains should be small to prevent, e.g., thickness fringes and bend contours and use of an objective aperture reduces the occurrence of displaced diffracted images, but also the spatial resolution. In summary, it can be concluded that for weakly scattering crystalline materials (zeolites) or highly scattering small crystallites (supported catalysts) BF TEM ET provides reliable 3D structural information.⁴⁷

For 3D imaging of crystalline materials predominantly incoherent signals, such as HAADF STEM and EF TEM, improve the projection relationship between mass density and image intensity.^{20,83} HAADF STEM images (Z-contrast images) are formed by electrons scattered close to the nucleus of the atom. This causes the scattering cross section for Z-contrast to approach the unscreened Rutherford potential⁹⁶ which is approximately proportional to the square of the atomic number Z .² To avoid effects from Bragg scattered electrons the required inner collection angle of the detector can be estimated from the atomic thermal vibrations, which gives ~ 40 mrad for silicon at 200kV.^{26,104} In addition, dynamical channeling effects may lead to changes in image intensity. The main advantage of HAADF STEM to be exceptionally sensitive to high Z elements, leads on the other hand to difficulties when imaging high and low Z elements together. In HAADF STEM ET, optimized for reducing the Bragg effects of high Z elements, low Z elements are hard to detect, since they do almost not scatter electrons into large angles. For imaging of metal particles and carbon supports, combined approaches utilizing the bright field and low-angle annular dark field signals in addition to HAADF have been suggested.⁹⁵

If one keeps the limitations of each technique in mind, in context with the composition and structure of the studied material as well as the scientific question, electron images are in first approximation projections suitable for tomographic reconstruction. As a guide, low Z materials containing small high Z crystalline domains can be readily imaged in 3D by BF TEM and HAADF STEM ET. Furthermore, HAADF STEM ET increases the contrast for high Z elements and reduces diffraction effects for large crystallites.

2.3. Applications

Applications of ET to catalyst materials are very broad and the following sections are organized corresponding to the materials classes of zeolites, ordered mesoporous materials, disordered oxide supported catalysts, carbon materials, and miscellaneous materials.

2.3.1. Zeolites

Zeolites are crystalline microporous materials that are widely applied as catalysts in the chemical industry.¹⁰⁵ The first applications of ET to a zeolite system, and the first to heterogeneous catalysts in general, were published by Koster *et al.*^{32,106} Characterization of an Ag/NaY crystal in 3D showed unequivocally the location of 10-40 nm Ag particles inside and outside the NaY structure. In addition, first results on the viability of 3D imaging of mesopores in zeolites are given.³² The special interest in imaging of mesopores can be concluded from recent reviews.^{107,108} For applications like cracking of heavy oil fractions, cumene production, alkane hydroisomerization and, more recently, fine chemicals synthesis, the shape and connectivity of mesopores in zeolite crystals is of major importance. The mesopores ensure an optimal accessibility and transport of reactants and products, while the zeolite micropores induce the preferred shape selective properties.

ET has been used to study various strategies to introduce mesopores in zeolites, namely steaming, acid leaching, base leaching, and secondary templating during synthesis. Main objectives of these studies were to determine how the post or pretreatments effect the three dimensional location, shape and connectivity of the mesopores. In two papers from our group a detailed formation mechanism of mesopores was proposed by studying a series of steam treated and acid-leached zeolite Y.^{80,109} The tomograms in Figure 5 directly show that steaming and acid leaching treatments are successful to obtain highly mesoporous zeolite Y crystals. It was concluded that mild treatments result in many cavities inside the crystals (Figure 5 a,b), while more severe treatments cause a loss of crystallinity and a decrease of micropore volume. After a special hydrothermal treatment (U.S. patent 5601798 (PQ Corp)), zeolite Y crystals with very high mesopore volumes (Figure 5c) and networks consisting predominantly of interconnected cylindrical mesopores were obtained.

An alternative approach, first studied by Jacobsen *et al.*, utilizes a secondary carbon template for creating intracrystalline mesopores during zeolite synthesis.¹¹⁰ ET results showed that both carbon nanofibers and carbon black aggregates were capable to act as a template for cylindrical mesopores that start at the external surface of the zeolite crystals.¹¹¹ The tortuosity of the mesopores templated by the carbon black aggregates was much higher than the cylindrical mesopores templated by the carbon nanofibers.

The most recent approach introduces mesoporosity in zeolites by desilication also referred to as base leaching.¹¹² In a study on the controlled desilication of ZSM-5, details of obtained 3D structures are reported.¹¹³ While Al gradients lead to a rather uniform mesoporosity development in the interior of the crystal, the outer Al-rich surface remained relatively unaffected. Desilication coupled to ET is seen as a suitable tool to elucidate aluminum gradients, which in the future will enable the fabrication of highly porous particles with tunable void volumes, sizes, and accessibility.

As a last example we would like to highlight the quantitative structural analysis of mesopores inside single zeolite crystals.¹¹⁴ The results of the image analysis, displayed in Figure 6, confirm that quantification from ET is possible and agreed well with physisorption measurements of the bulk material.¹⁰⁹ While physisorption methods prevail in the characterization of the bulk mesopore properties, analysis of individual objects by ET does not assume a specific pore shape, which makes both approaches complementary.

The results presented in this section illustrate that bright-field TEM ET provides reliable 3D structural information of low *Z* crystalline materials. Detailed insight into shape and connectivity of mesopores will contribute to enable a rational design of zeolite-based systems that display improved catalytic properties.

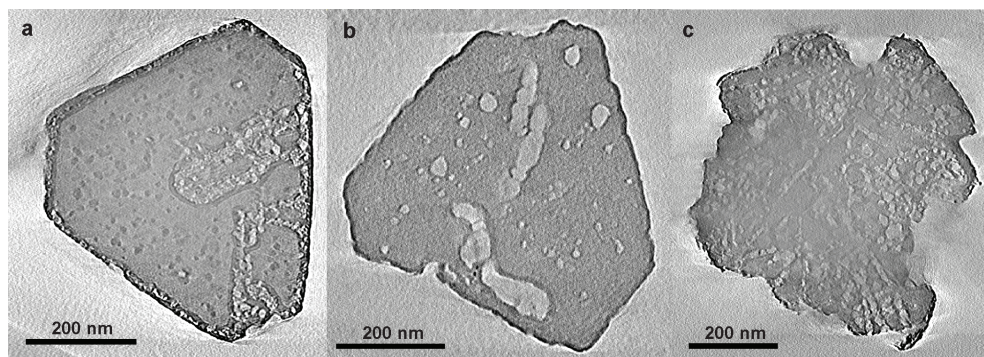


Figure 5 Slices through 3D reconstructions of steamed zeolite Y (a), steamed and acid leached zeolite Y (b), and high-meso zeolite Y (c) showing the formation and connectivity of mesopores.^{80,109}

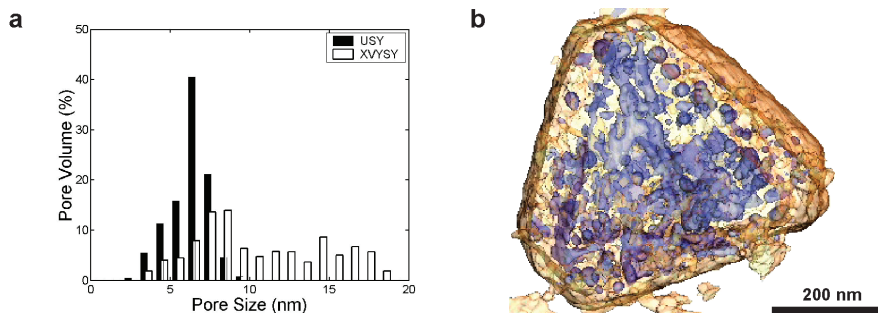


Figure 6 Mesopore size distributions of steamed zeolite Y (USY) and steamed and acid leached zeolite Y (XVUSY) obtained by image analysis of electron tomograms (a), and 3D representation of steamed and acid leached zeolite Y (b) showing the mesopores through the transparent surface of the particle.¹¹⁴

2.3.2 Ordered mesoporous materials

The introduction of ordered mesoporous materials (OMM) has opened up a completely new field of research.^{115,116} OMMs show great potential for applications ranging from chromatography¹¹⁷ over drug delivery¹¹⁸ to catalysis.¹¹⁹ OMM self-assembly is carried out by sol-gel synthesis in aqueous solution with various surfactants or polymer templates to allow a wide range of pore sizes, pore morphologies and chemical compositions.

Structural elucidation of OMMs, commonly carried out by model based analysis of electron micrographs, X-ray diffraction (XRD) and physisorption data, can be aided by ET in particular for complex non-repeating morphologies that deviate from ideal geometry. To illustrate this point, in Figure 7 the pore structure of the two most prominent ordered mesoporous silicas (OMS), namely MCM-41 and SBA 15, are shown. While both OMS expose a 2D hexagonal pore ordering^{115,116} (Figure 7a), MCM-41 mesopores (Figure 7b) can have a hexagonal to round pore shape^{120,121}, and SBA-15 mesopores (Figure 7c) are corrugated and interconnected.¹²²⁻¹²⁴ In particular, the pore corrugation of SBA-15 requires a local description which was recently provided by combining ET and image analysis.¹²⁵ Pore corrugation was modeled in terms of a locally variable pore radius and center and results compared well with the corona model used to analyze XRD and physisorption data. Also the mesoscopic ordering of SBA-15 pore has been examined by ET.¹²⁶ Although a 2D hexagonal lattice of mesopores existed on a microscopic scale, irregularly curved pores (U-shaped) on the mesoscopic length scale were also observed. Thus the diffusion path length in curved pores may be much larger than commonly estimated from the particle size.

A second example in this field revealed the local morphology of submicron MSU-type particles.¹²⁷ It could be shown that the structure was composed of folded ribbons of hexagonally packed mesoporous silica, enclosing cavities inside the particle. The material (consisting of small particles, large pores, and cavities) was found to have very similar separation properties than commercial powders used in high performance liquid chromatography. A detailed quantitative analysis of the 3D pore structure of chromatographic adsorbents can be found in Yao *et al.*¹²⁸

More recent studies investigated macroporous ordered siliceous foams (MOSF)¹²⁹, chiral mesoporous silica (CMS)¹³⁰, silica possessing a concentric circular mesostructure¹³¹, cage-type mesoporous silica FDU-12¹³², and periodic mesoporous organosilicas (PMO).¹³³ The MOSF forms a honeycomb structure where each silica vesicle (~ 100 nm diameter) is a hexagonal prism linked with three adjacent cells from the next layer.¹²⁹ For the CMS, prepared from achiral cationic surfactants, mesopores running spiral within the particle could be visualized. Particle morphology and the helical pitch could be systematically controlled by varying the ammonia concentration during preparation and ET indicated that a particle can be composed of two helical rods of opposite handedness.¹³⁰ In contrast, silica with a concentric circular mesostructure were composed of hexagonally ordered pores without helical pitch thus forming closed rings.¹³¹ For the ordered cage-type mesoporous silica FDU-12, intergrowth between cubic and hexagonal close-packed structures was observed and ET enabled the direct visualization of stacking faults.¹³² Also in the PMO material stacking faults could be visualized but, most interestingly, changes in pore length and ordering could be tuned by the acidity of the reaction mixture.¹³³

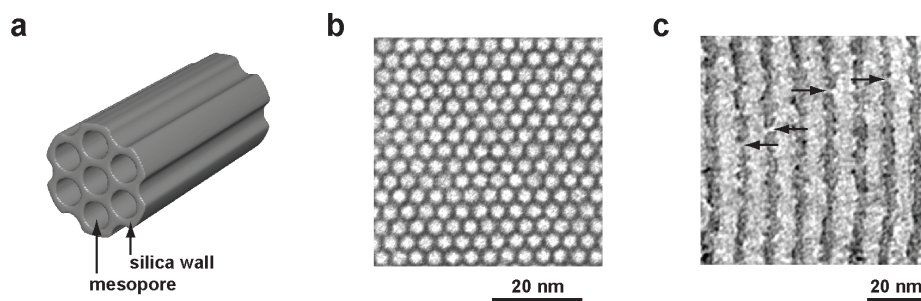


Figure 7 Model of 2D hexagonal pore ordering in MCM-41 and SBA-15 (a), TEM image of MCM-41 with a hexagonal pore shape (b), numerical cross-section through reconstruction of SBA-15 showing corrugated mesopore walls in dark grey and pore connections are indicated by arrows (c).

While the above examples utilized bright-field TEM ET, OMM materials can also be imaged using HAADF STEM ET as shown by the Midgley group. In an approach, referred to as real-space crystallography, the MCM-48 lattice structure was modeled.¹³⁴ ET results of the complex gyroid-like 3D pore network were consistent with the proposed space group of $Ia\bar{3}d$,¹³⁵ but showed differences along the $[111]$ zone axis. Based on the findings a new pore model was suggested. Most notably a grain boundary could be imaged in the MCM-48 particle, since ET resolves non-periodic structures. This should not distract from the fact that electron crystallography of OMMs, pioneered by the Terasaki group, is an increasingly important technique in the field.^{7,136,137}

For applications in catalysis the ordered pore arrangement in combination with a very narrow pore-size distribution makes OMM excellent model supports for active phases and reference systems to study catalyst preparation.¹³⁸ In particular for MCM-41, the first representative of ordered mesoporous silica (OMS), isomorphous substitution of metal ions into the silica framework or deposition of metal particles onto the mesopore surfaces have been extensively studied.¹³⁹ Not surprisingly, first applications of ET to this field dealt with MCM-41 supported metal particles. In a series of papers from the Midgley group the dispersion of Pd_6Ru_6 ^{20,96,140} and $Ru_{10}Pt_2$ ¹⁴¹ in MCM-41 were studied. An account on the catalytic performance of bimetallic nanoparticles for hydrogenations is given by Thomas.¹⁴² ET results of the Pd_6Ru_6 system proved that the mesoporous structure of the silica could be faithfully reconstructed with little sign of beam damage. The bimetallic particles did have a definite size distribution as a result of coalescence, with larger particles present outside the mesopores and the smaller ones inside. For $Ru_{10}Pt_2$ /MCM-41 a high particle density combined with good dispersion of the bimetallic phase inside the mesopores was observed (Figure 8).¹⁴¹ Moreover, the local catalyst loading was calculated to $1.4 \cdot 10^{-5} \text{ g} \cdot \text{m}^{-2}$ by counting the number of $Ru_{10}Pt_2$ particles and measuring the internal surface of the silica inside a subvolume of the reconstruction. From the fact that imaging of 12 atom clusters, known to be less than 1 nm in diameter, was successful, a tomographic resolution of $\sim 1 \text{ nm}$ in all three dimensions could be inferred.^{140,141} This value exceeds the resolution predicted by the Crowther criterion discussed in section 2.2.2 on page 16.

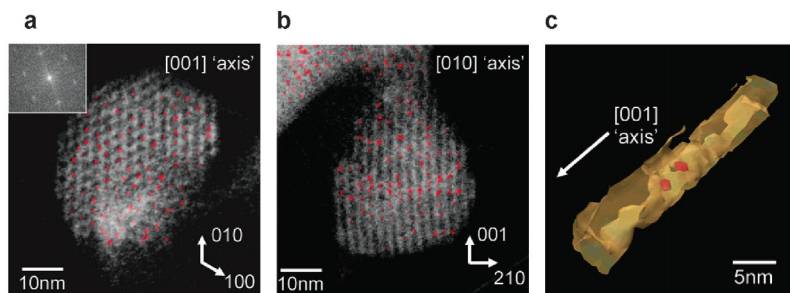


Figure 8 Two perpendicular voxel projections of MCM-41 supported Pt/Ru nanoparticles (a,b), and surface render of single mesopore segment with two nanoparticles inside (c). Reprinted with Permission from ref 141. Copyright 2004 American Chemical Society.

Although MCM-41 has quite unique structural properties, its thin pore walls are prone to collapse in boiling water. In contrast, SBA-15 exhibits better hydrothermal stability as a result of its thicker silica walls.¹¹⁶ Thus SBA-15 can be applied over a larger range of reactions conditions and therefore is a suitable support material for heterogeneous catalysts. In a series of papers from our group structural properties of SBA-15 model catalysts containing ZrO_2 ¹⁴³, Au^{46,143}, and NiO^{49,144} particles were investigated. ET provided unequivocal information on the location and size of the metal (oxide) particles inside of the support. Microscopic observations, namely blocking of mesopores by incorporated particles, could be directly correlated with features in the desorption isotherm of N_2 -physisorption experiments.^{143,144} For all guest phases (ZrO_2 , Au, NiO) a non-uniform distribution of particles in the mesopores of the support was found. While in some pores many particles were present, others did not contain any.

The effect of an inhomogeneous distribution on the local loading in filled pores was studied in detail for NiO/SBA-15 model catalyst.⁴⁹ Quantification by image analysis showed that locally a loading twice the average bulk loading was present (Figure 9). The ET derived NiO particle size distribution was in agreement with the diameter obtained by XRD and statistical analysis of the nearest-neighbor distances is only one possibility to utilize the information provided by ET for the study of catalysts. Further details of this study are presented in chapter 4, page 63. Additional examples for the quantitative analysis of electron tomograms are given by Ersen *et al.*¹⁴⁵

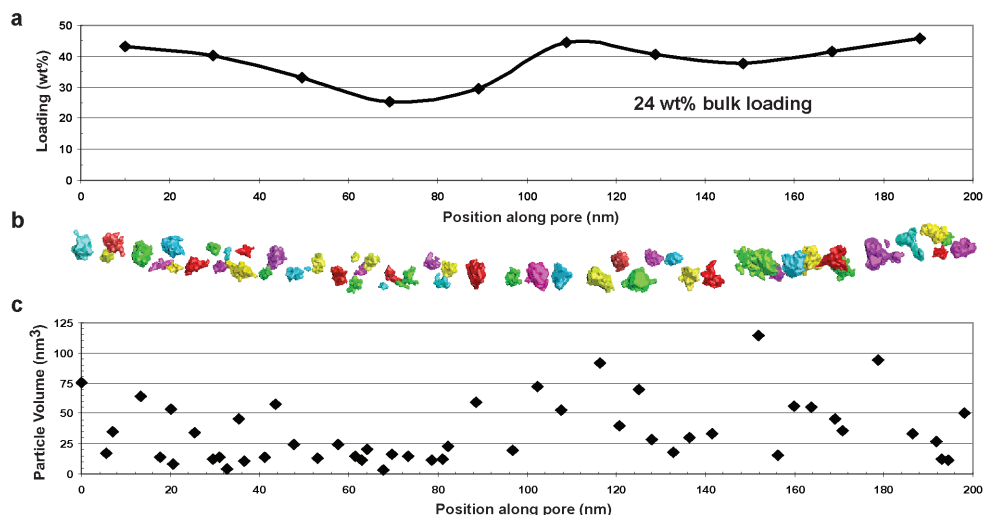


Figure 9 Local NiO loading in one SBA-15 mesopore (a), surface view of NiO crystallites in mesopore (b), and volume of crystallites plotted vs. position along the mesopore (c). Reprinted with permission from ref 49. Copyright 2007 American Chemical Society.

The presented examples show that ET has become an indispensable technique for the 3D structural investigation of OMMs and OMM-based heterogeneous catalysts. It is also expected to facilitate understanding of OMS templated nanostructures¹⁴⁶, such as gold nanorods with tunable aspect ratios synthesized in SBA-15 by a seed mediated growth.¹⁴⁷ Here we also would like to mention applications of ET to nanostructures formed by alternative routes, such as Pt fibers grown by guided deposition of nanoparticles in a physically confined self-assembly of surfactants¹⁴⁸, nanoporous gold fabricated by chemically dealloying AuAg films¹⁴⁹, heterostructured GaP-GaAs nanowires grown by metal-organic vapor-phase epitaxy¹⁵⁰, and helical or zigzagged GaN, ZnGa₂O₄, Zn₂SnO₄ nanowires grown by the vapor-liquid-solid mechanism.¹⁵¹

2.3.3 Disordered oxide supported catalysts

Disordered oxide supported catalysts are often applied in industry since they combine a relatively high dispersion (amount of active surface) with a high degree of thermostability of the catalytically active component. In this section silica and alumina supports are discussed while other ceramics (ceria, zirconia, and titania) are presented in section 2.3.5, page 35. The first example in this section investigated the 3D localization of Pd particles in two Pd/SiO₂ cogelled catalysts.⁷⁶ Structural differences were quantified by image analysis and an illustration of the results are presented in Figure 10. For a Pd loading of 1.1 wt% an earlier simplified geometrical model could be confirmed, in which the Pd particles (4.4±1.1 nm diameter) are located in the center of the primary silica particles (12.5±4.8 nm diameter). When the Pd loading increased to 3.1 wt% the diameter of the Pd particles increased slightly (4.8±1.3 nm diameter), while the diameter of the silica skeleton decreased (10.3±4.8 nm). ET proved that for the higher loading also a significant fraction of the metal was located outside the silica.

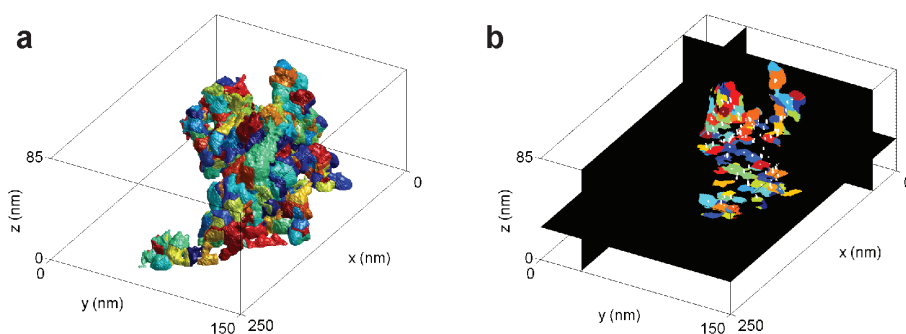


Figure 10 Quantitative analysis of 1.1 wt% Pd on SiO₂ cogelled catalyst by Voronoi tessellation of the silica skeleton. Each colored region corresponds to the silica shell around a specific Pd nanoparticle. Outer surface of the silica skeleton (a), three numerical cross-sections showing Pd particles in white (b). Reprinted with permission from ref 76. Copyright 2005 American Chemical Society.

Alternatively to cogellation deposition of the active metal phase inside the silica, deposition of a catalyst precursor on the silica surface (i.e. by impregnation with a precursor-containing solution followed by drying and calcination) is also extensively used in catalyst preparation. In a case study by the Midgley group, ET was applied to image the dispersion in a highly effective $\text{Ru}_5\text{PtSn}/\text{SiO}_2$ catalyst for single step hydrogenation.¹⁵² The Ru_5PtSn phase had a tendency to be evenly distributed, mainly close to the surface of the silica particles and no sintering occurred during exothermic hydrogenation. Further work of the same group on the dispersion of $\text{Ru}_8\text{Pt}_2\text{C}_2$ in silica gel combined ET with image analysis.⁷⁹ By determining the location of catalyst particles as a function of the local curvature of the support, as seen in Figure 11, preferential sites were classified. Nanoparticles within the interior preferred the saddle-shaped surfaces of the support, while nanoparticles at the support exterior were mainly located in saddle- and cup-like regions. Such detailed 3D analysis of the metal particle location is key in improving the properties of hierarchically ordered systems.

Alternatively to silica, alumina is one of the most commonly used supports for preparation of e.g. oil refining or Fischer-Tropsch (FT) catalysts. Two ET examples of oil refining catalysts are given by Kübel *et al.*⁴⁷ The studied catalysts were composed of a high surface area alumina support with well dispersed small MoO_3 or Pt particles inside the structure. For the Pt containing system the resolution in the reconstruction was sufficient to analyze the Pt particle size distribution by means of line profiles. Pt particles had a diameter between 1 and 3 nm with a distribution maximum at ~ 1.8 nm.

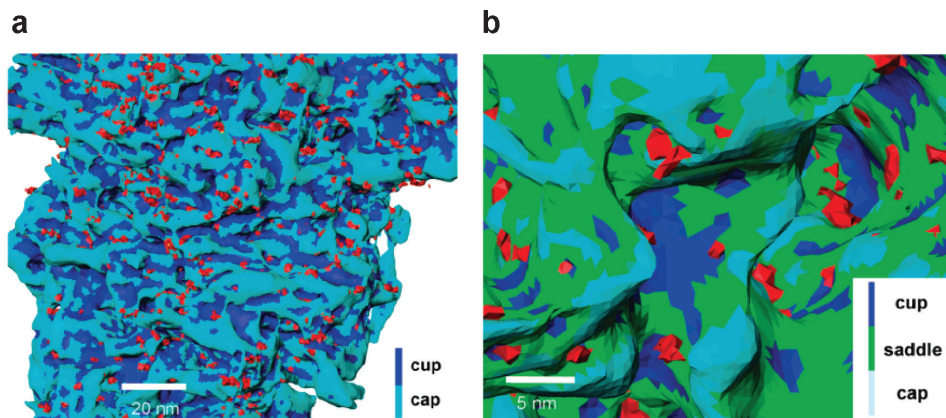


Figure 11 Region of the exterior silica surface colored according to its local curvature and Ru/Pt particles shown in red (a,b). The metal particles appear to be situated preferentially in positions with saddle to cup-like geometry. Reprinted with permission from ref 79. Copyright 2007 American Chemical Society.

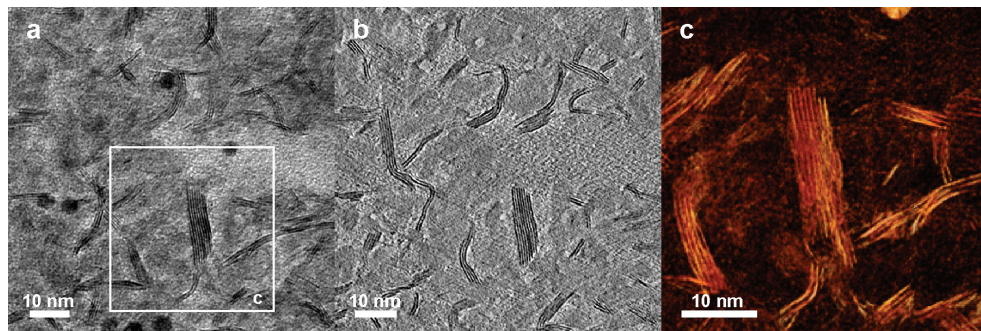


Figure 12 TEM image of a $\text{MoS}_2 / \gamma\text{-Al}_2\text{O}_3$ catalyst with 5 nm gold particle (dark spots) attached to the thin section (a), slice through reconstruction showing the 0.6 nm spaced MoS_2 crystal planes (b), and voxel projection displaying only the complex interconnected MoS_2 network (c). Reprinted with permission from ref 153. Copyright 2006 American Chemical Society.

Further work by our group extended the use of ET to a commercial, sulfided Ni-Mo/ $\gamma\text{-Al}_2\text{O}_3$ hydrotreating catalyst.¹⁵³ As seen in Figure 12, the MoS_2 particles in the pores of the support were imaged with sufficient accuracy to resolve the 0.6 nm spaced MoS_2 crystal planes. The MoS_2 particles form a complex interconnected structure within the mesopores and their individual shape largely deviates from simple models as derived from studies on model catalysts. Without a doubt such information is extremely valuable to aid in first principle modeling of sulfide catalysts.¹⁵⁴ This includes recent strides towards atomic resolution tomography of MoS_2 based fullerene-like nanostructure by the combination of low voltage electron microscopy with aberration-corrected phase contrast imaging.¹⁵⁵

The last example in this section deals with catalysts for the Fischer-Tropsch (FT) process that receives much attention both in academia and industry. In work by Arslan *et al.* the structure of two unreduced Re promoted Co_3O_4 /alumina FT catalysts was investigated.¹⁵⁶ It was concluded that the less C_{5+} selective catalyst consisted of fully interlocking metaloxide/ γ -alumina aggregates. When a Ni impregnated and high temperature heat treated γ -alumina support is used, a fine distribution of nickel aluminate within a coarser α alumina skeleton is observed. In this catalyst the Co_3O_4 shows a preference to form nanocages around the nickel aluminate. After reduction the metallic Co might display a more open local environment, which is believed to be responsible for the higher C_{5+} selectivity of this catalyst. The case studies cited in this section illustrate the potential of ET for investigating systems with a complexity approaching industrial catalysts at (sub)-nanometer resolution.

2.3.4. Carbon materials

Carbon materials are widely used as catalyst supports, absorbents, and additives in the chemical, pharmaceutical, food, and agricultural industry because of their high surface area, low cost, and good chemical stability in liquid media. The most commonly used structures are activated carbons, carbon black, graphite, and carbon fibers/tubes. One of the advantages of carbon based catalysts relates to the facile reclaim of noble metals simply by combusting the carbon. Since ET studies of non-functionalized carbon materials are sparse, existing examples will be given prior to the functionalized structures. At the end of this section carbon nanotube/polymer composites and the morphology of carbon black emissions, in context with its environmental impact, will be discussed.

First ET studies of carbon-based catalysts were carried out by the Midgley group using HAADF STEM ET on a Pd/C system.^{67,157} The carbon support (400-600 nm in diameter) and the Pd nanoparticle aggregates larger than 6-10 nm could be successfully resolved in 3D. In some instances clear clustering of the 1-20 nm sized particles was observed. Further work of the same group on a Pt/C system showed that down to a size of 5 nm the shape and size of the Pt particles was well resolved.¹⁵⁸ However, characterization of the carbon matrix by HAADF STEM ET was difficult and a combination with low-angle annular dark imaging was suggested⁹⁵ to improve results (see also section 2.2.4, page 20).

Two additional examples of ET to study the 3D structure of Pt/C catalysts are given by Wikander *et al.*¹⁵⁹ and Abrosimov *et al.*⁴⁸ In the former case ~ 3 nm sized Pt particles on an ordered mesoporous carbon (KIT 6 replica), and in the latter ~ 2-4 nm sized Pt particles on a poorly crystallized carbon support (Sibunit) were imaged. In both instances ET confirmed that the particles were distributed both at the interior and exterior surfaces of the support and some larger agglomerates were present. For the Sibunit support (hollow carbon globules) BF TEM ET resolved a gap of 15 nm in the globule structure rationalizing dispersion of the Pt particles in the inside.

Applications of Pd/C and Pt/C systems range from hydrogenations¹⁶⁰ to electrodes in fuel cells.¹⁶¹ In a polymer electrolyte membrane (PEM) type fuel cell, a polymer electrolyte (commonly Nafion) separates the two carbon electrodes. The Pd or Pt nanoparticulate catalyst is deposited inside the pores of the carbon. Therefore, efficient penetration of the pores by the polymer electrolyte, and hence effective electrical contact, is essential for the fuel cell performance. An ET study linked the performance of the PEM type fuel cell to the Pt and the Nafion distribution.¹⁶² It could be shown that an autoclave treatment promoted the penetration of the Nafion into carbon black pores smaller than 100 nm, where 90% of the Pt was located, thus improving utilization of the catalyst. Such detailed insight can also aid in evaluating the long-term stability of fuel cell systems.¹⁶³

In context of mobile power sources we also would like to mention ET results on carbon nanospheres (CNS) used in Li-ion battery cathodes. An important strategy to improve the charge/discharge rate of the batteries is to interpenetrate the negative electrode and electrolyte on the nanoscale, thus increasing the effective interface area. An ET study showed that CNS can have a heterogeneous core-shell structure.¹⁶⁴ In combination with high-resolution TEM it was concluded that the outside consisted of a series of ~10 nm thick faceted carbon walls, while the inside did not show graphitic ordering. Structure defects seemed to be concentrated along the ridgelines of the CNS particles and are possibly the ion paths causing improved battery performance. Application of ET to study the 3D structure of batteries has been suggested previously¹⁶⁵ and now, with the first application showing success, a more extensive use can be expected.

Another carbon structure with great potential as catalyst support¹⁶⁶ are carbon nanotubes (CNT).¹⁶⁷ In the first ET study of CNTs the hollow core could be resolved in 3D, which until then was only inferred from 2D imaging.¹⁶⁸ In a recent paper by Bals *et al.* the morphology and composition of bamboo-like CNTs including the catalyst particle were investigated.¹⁶⁹ ET results showed that the hollow compartments had a cone-like 3D structure, and that cavities were present in the catalyst particle. Intensity variations between different parts of the catalyst particle indicated an inhomogeneous composition which was identified to Cu and Cu₂O by EF TEM. Reconstruction of the 3D structure was carried out by an algorithm that combines reconstruction and segmentation, which allowed quantitative information on the individual phases to be obtained in a straightforward manner.

From an application point of view, interfaces between nanotubes and metals are of considerable interest. In work by the Muller group, the buried interfaces between nanotubes and the metal were studied by ET.¹⁷⁰ Samples were prepared by electron-beam evaporation of metals onto commercially purchased nanotubes. Gold was found to deform the nanotubes creating flat contact surfaces. As one goes from poorly wetting gold to a gold-palladium alloy to palladium and finally to strongly wetting titanium, a decreasing tendency for nanotube deformation was observed.

Alternatively to outer surface functionalization, deposition of an active metallic phase inside CNT could open up new possibilities in catalysis as a result of a synergetic confinement effect.¹⁷¹ In this context, locating the position of the deposited particles with respect to the tube wall is crucial. In work by Ersen *et al.* the filling of multi wall CNT by Pd particles (prepared from a nitrate precursor using aqueous impregnation) was investigated.⁷⁸ As seen in Figure 13, acid treated tubes of 30 nm inner diameter had more than 50% of the Pd particles located on the inside. At 10 wt% loading a homogeneous deposition on the inside of the multi-wall (MW) CNT by 3-4 nm Pd particles with a density of 0.13 particles per nanometer tube length was derived. When decreasing the inner tube diameter to 15 nm, almost exclusive deposition on the outside was found. Interestingly, the diameter of the palladium particles was not affected by their location, i.e. inside or outside of the nanotube.

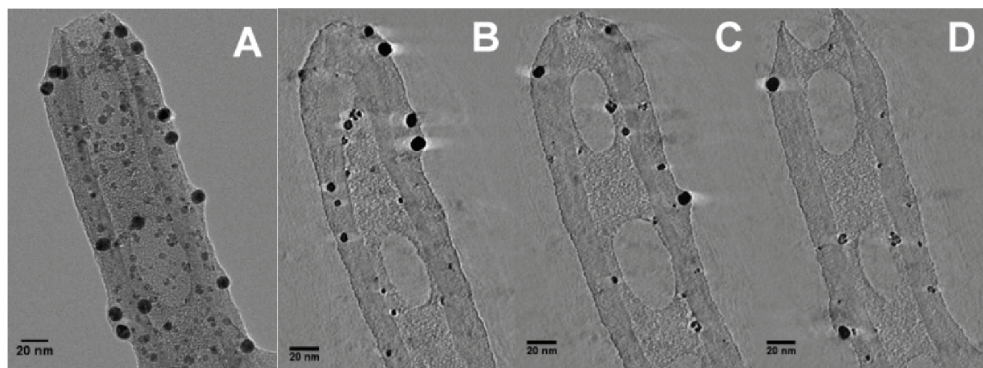


Figure 13 Palladium nanoparticles on the inside and the outside of a multiwalled carbon nanotube. TEM image from the tiltseries (A), and numerical cross-sections through reconstruction (B-D). The presence of an amorphous phase (from suspension in ethanol for TEM sample preparation) wetting both the inside and outside could be observed. The 10 nm sized spots on the outside are colloidal gold particles deposited to aid in alignment of the dataset. Reprinted with permission from ref 78. Copyright 2007 American Chemical Society.

Further work of the same author on $\text{CoFe}_2\text{O}_4/\text{CNTs}$ related preparation effects (incipient wetness impregnation followed by calcination) to the average crystallite size and position in the CNT.¹⁷² An example of the 3D morphology of a carbon nanofiber supported Fischer-Tropsch catalyst can be found in reference 173.

The next paragraph leaves catalysis-related applications and turns briefly to CNT/polymer composites. Despite their unique properties, research on CNTs is complicated by their strong cohesive nature which limits dispersability. When wrapping single-wall CNTs with a water-soluble polymer the dispersability increases, facilitating purification. Also from an application point of view good dispersability is highly desired, since addition of a relatively small concentration of nanotubes to polymers significantly increases the electrical, thermal, and mechanical properties of the composite material. In a study on the wrapping of CNTs it could be concluded that the polymer (in this case polysaccharide) existed as a uniform layer around the CNTs.¹⁷⁴ An ET example on the incorporation of sodium dodecyl sulfate coated MWCNTs in a polystyrene matrix showed no CNT aggregation.¹⁷⁵ A potential problem when trying to image such composites is the similar contrast between the two carbon-based components. To enhance the contrast EF TEM tomography can be employed.⁸⁵ Ratio images of the energy-filtered tomographic reconstructions clearly differentiate the MWCNT and the polymer (nylon) region. Low-loss spectra extracted from the bulk nylon, the nylon surface, a hole in the nylon, and the CNT hinted towards subtle differences in the corresponding electronic structure. One can envision further developments to obtain 3D information on the local bonding, which would be highly desired for catalytic applications. Additional studies by EF TEM ET can be found in the references of section 2.2.4, page 20.

The end of this section dedicated to carbon materials deals with a topic of general interest closely related to catalysis, namely air pollution generated from automotive engines. Despite the great improvements that fuel producers, car manufactures and legislation have made towards the abatement of pollution, certain limitations of combustion engines are hard to overcome. One important aspect is the incomplete combustion of fossil fuels which in turn creates soot particles that are emitted in large quantities, ~ 8 Tg/year.¹⁷⁶ It was estimated that the overall contribution of soot to global warming may be only second to that of CO₂.^{177,178} Soot typically aggregates into clusters (also referred to as mass fractals) that consist of numerous small primary particles. ET studies by the Buseck group investigated the 3D shapes of soot aggregates.^{179,180} Two examples are displayed in Figure 14. It could be shown that morphological parameters (fractal dimension, radius of gyration, surface area) captured in 3D more accurately than 2D TEM values estimate atmospheric lifetimes utilized in global distribution models. Most importantly, the light-scattering properties of the complex aggregates were found to be up to 30 times larger than the values of un-aggregated spheres commonly assumed to model the climate impact of soot.¹⁸⁰ In the future such results are expected to be applied not only to improve climate models but also to minimize high impact pollution.

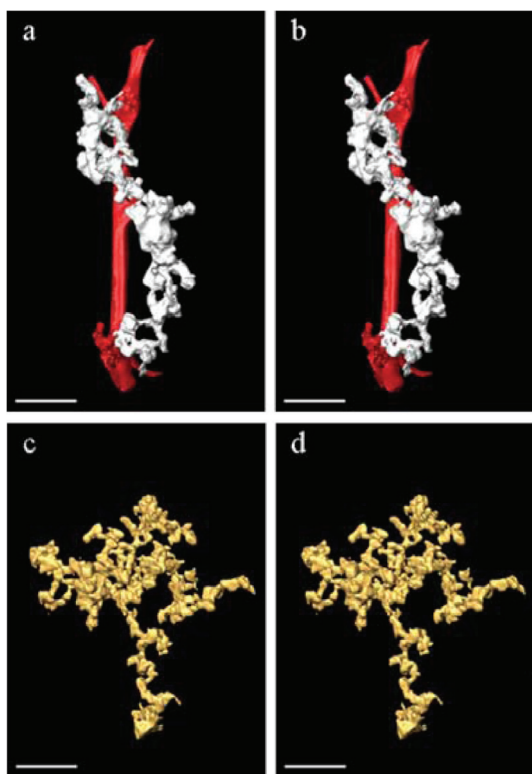


Figure 14 Stereo pairs (wide-eyed) of soot aggregates produced by incomplete combustion of biomass (a,b), and from a diesel engine (c,d) illustrating the complex fractal geometry of the structures. The vertical red bar in the top pair is the support for TEM imaging. Scale bars are 200 nm. Reproduced by permission of American Geophysical Union from ref 179. Copyright 2005 American Geophysical Union.

2.3.5. Miscellaneous materials

In this section, other materials like ceramics, polymers and nanocomposites that have been investigated by ET are reviewed. While ceramic supports are often supposed to be inert (section 2.3.3.) they can also expose catalytic properties.^{181,182} Titanium dioxide in the anatase form, for example, is a photocatalyst under ultraviolet light (UV). A combined ET, in-situ TEM and EELS study observed structural changes from single crystalline TiO₂ to polycrystals during photocatalytic oxidation of hydrocarbons.¹⁸³ When introducing extrinsic metals, UV activated decomposition of organic and inorganic pollutants can be improved. To determine the 3D morphology of an Ag/TiO₂ catalyst manufactured by spray pyrolysis, ET was employed.¹⁸⁴ It could be shown that silver particles of less than 10 nm were uniformly dispersed on the inside and on the outside of the titania agglomerate. The spherical titania agglomerate, with a diameter of 150 nm, was composed of 10 -20 nm titania particles.

Also ceria and zirconia show properties that go beyond an inert support.^{185,186} The application of ceria-zirconia mixed oxides to the three way catalysts considerably reduced pollution by increasing the oxygen storage capacity and thermal stability of the system.¹⁸⁷ Enhanced redox properties can be induced by severe reduction followed by a mild oxidation.¹⁸⁸ This process has been associated with a transition from rounded crystallites to well-faceted oxide particles.¹⁸⁹ ET revealed a final particle shape very close to that of an octahedron. The observed change in morphology was also accompanied by an increase of Zr-rich, {111}-type surfaces, which could be key factors in understanding the distinct chemical behavior of the ceria-zirconia nanocrystals.¹⁸⁹ Further studies investigated the 3D structure of ceria nanocrystals in context of their application as oxygen conductor in solid oxide fuel cells.¹⁹⁰ Crystals prepared by hydrothermal synthesis predominantly exposed {200} cubic facets, which offer the largest number of active sites. In combination with an average particle size of 6.7 nm, ensuring a high surface area, a high activity is expected.¹⁹⁰ To conclude the field of ceramics, we also would like to mention a recent materials science example in which ET was used to explore the morphology of ceria nanodendrites in an alkali-borosilicate glass matrix following a glass melting and annealing procedure.¹⁹¹

The next class of materials discussed in this section are polymers. Their main application in catalysis is as supports, e.g. for immobilization of homogeneous catalysts to improve catalyst recovery.^{192,193} From a structural point of view, block copolymers, which self-organize into microphase-separated nanostructures, are of particular interest. ET studies of diblock copolymers show assembly into 3D structures composed of hexagonally stacked cylinders¹⁹⁴⁻¹⁹⁶ and lamellar structures.¹⁹⁷⁻¹⁹⁹ Triblock copolymers have been shown to form microdomain structures composed of cylinders with polygonal cross-sections packed in square lattices²⁰⁰ and in hexagonal lattices.²⁰¹ Porous supports can be obtained from the microphase-separated block copolymer by selective degradation of one of the microdomain phases.²⁰²

A detailed 3D structural analysis of a porous polymer support containing Pd particles was carried out by Jinnai *et al.*⁷⁷ ET results unambiguously resolved the porous polymer network with most of the Pd particles located at the polymer/pore interface (Figure 15). Using image analysis, quantitative structural information such as the number of Pd particles per surface area ($490 \mu\text{m}^{-2}$), the Pd particle size distribution ($\sim 4.2 \text{ nm}$ radius), and the penetration of the Pd particles into the surface ($\sim 1.2 \text{ nm}$) could be obtained. For a detailed account on the 3D structural characterization of polymers we refer to a recent review.⁵⁵

Closely related to many of the above materials is the field of nanocomposites which was briefly discussed for carbon nanotubes in section 2.3.4 on page 32. Nanocomposites are created by introducing nanoparticulate fillers into a matrix material to tune electrical, thermal, and mechanical properties of the resulting system. Here we would like to mention ET studies on polymer nanocomposites containing silica^{203,204}, carbon black²⁰⁴, carbon nanotubes^{85,175}, and ceramics^{205,206} as a few examples from the literature.

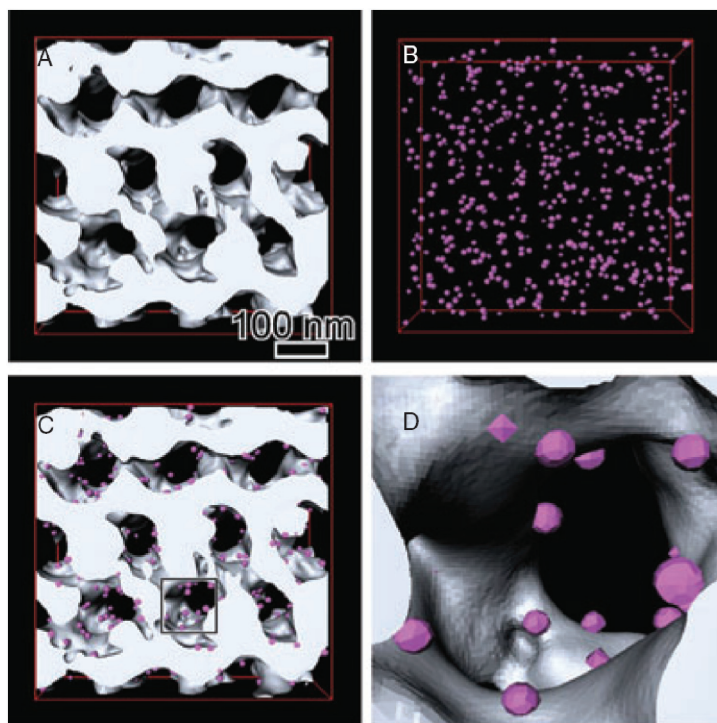


Figure 15 Surface visualization of porous polymer (A), Pd nanoparticles (B), superposition of porous polymer and Pd (C), and close up view (D) of the region boxed in (C). Reprinted with permission from ref 77. Copyright 2006 John Wiley and Sons, Inc. and The Japan Chemical Forum.

2.4 Conclusions and Outlook

The controlled assembly of functional materials on the nanoscale has been a major focus of research across many scientific disciplines over the last decades.^{115,116,167,207,208} These developments were in part fueled by the availability of characterization techniques, such as TEM, that can probe obtained structures with high spatial resolution. With the increasing complexity of nanomaterials and to gain precision in synthesis and assembly, elucidation of their full 3D morphology becomes more and more important.^{33,209} Facilitated by automated ET data collection systems and high performance desktop computing, ET is now used as a tool for the 3D structural characterization of inorganic materials.^{20,32} At present, mainly bright-field TEM ET and high-angle annular dark-field STEM ET are applied, depending on sample composition, degree of crystallinity, and crystallite size. With the advent of aberration-correctors for electron microscopy^{210,211} new opportunities for materials characterization arise²¹², potentially providing 3D information at atomic resolution.^{17,155,213} In this review we have given a number of examples that highlight the importance of ET in the field of catalysis. When studying hierarchical materials, such as mesoporous zeolites or supported catalysts, accurate knowledge of the 3D morphology significantly aids in understanding their physico-chemical properties. To obtain unbiased quantitative structural information image analysis can be considered as the next key step.^{49,56,76,78,79,156} However, one can not emphasize enough the linking of ET derived results to bulk characterization techniques to ensure that statistically significant sample properties are described. Now the first examples using image segmentation (measuring porosity, particle size distributions, or tortuosity) provide a microscopic explanation for bulk properties. With a wealth of nanostructural data at hand, the challenge ahead lies in relating this information to the catalytic properties of materials. ET delivers fundamental insights into the 3D structure of complex hierarchical materials and is expected to contribute significantly to rational catalyst design in the future.

References

- (1) Williams, D. B.; Carter, C. B. *Transmission electron microscopy: a textbook for materials science*; Springer Science+Business Media, Inc. A Division of Plenum Publishing Corporation: New York, 1996.
- (2) Reimer, L. *Transmission Electron Microscopy*; 4th ed.; Springer-Verlag: Berlin, 1997.
- (3) Yao, N.; Wang, Z. L. Eds. *Handbook of Microscopy for Nanotechnology*; Kluwer (now Springer): Boston, 2005.
- (4) Gai, P. L.; Boyes, E. D. *Electron Microscopy in heterogeneous catalysis*; Institute of Physics Publishing: Bristol, 2003.
- (5) Thomas, J. M.; Terasaki, O. *Top. Catal.* **2002**, *21*, 155.
- (6) Datye, A. K. *J. Catal.* **2003**, *216*, 144.
- (7) Anderson, M. W.; Ohsuna, T.; Sakamoto, Y.; Liu, Z.; Carlsson, A.; Terasaki, O. *Chem. Commun.* **2004**, 907.
- (8) Thomas, J. M.; Midgley, P. A. *Chem. Commun.* **2004**, 1253.
- (9) Stroud, R. M.; Long, J. W.; Pietron, J. J.; Rolison, D. R. *J. Non-Cryst. Solids* **2004**, *350*, 277.

- (10) Diaz, I.; Alfredsson, V.; Sakamoto, Y. *Curr. Opin. Colloid Interface Sci.* **2006**, *11*, 302.
- (11) Gai, P. L. *Top. Catal.* **2002**, *21*, 161.
- (12) Egerton, R. F. *Top. Catal.* **2002**, *21*, 185.
- (13) Arbiol, J.; Rossinyol, E.; Cabot, A.; Peiro, F.; Cornet, A.; Morante, J. R.; Chen, F. L.; Liu, M. L. *Electrochem. Solid-State Lett.* **2004**, *7*, J17.
- (14) Heinrichs, B.; Geus, J. W.; Lambert, S.; Pirard, J.-P. *J. Catal.* **2006**, *241*, 229.
- (15) Li, F.; Wang, Z.; Ergang, N. S.; Fyfe, C. A.; Stein, A. *Langmuir* **2007**, *23*, 3996.
- (16) Bovin, J. O.; Alfredsson, V.; Karlsson, G.; Carlsson, A.; Blum, Z.; Terasaki, O. *Ultramicroscopy* **1996**, *62*, 277.
- (17) Borisevich, A. Y.; Lupini, A. R.; Pennycook, S. J. *Proc. Natl. Acad. Sci. U. S. A.* **2006**, *103*, 3044.
- (18) Sakamoto, Y.; Kaneda, M.; Terasaki, O.; Zhao, D. Y.; Kim, J. M.; Stucky, G.; Shin, H. J.; Ryoo, R. *Nature* **2000**, *408*, 449.
- (19) Dorset, D. L.; Roth, W. J.; Gilmore, C. J. *Acta Crystallogr., Sect. A: Found. Crystallogr.* **2005**, *61*, 516.
- (20) Midgley, P. A.; Weyland, M. *Ultramicroscopy* **2003**, *96*, 413.
- (21) Midgley, P. A.; Weyland, M.; Stegmann, H. Applications of Electron Tomography. In *Advanced Tomographic Methods in Materials Research and Engineering*; Banhard, J., Ed.; Oxford University Press: Oxford, 2008; p. 335.
- (22) Koster, A. J.; Grimm, R.; Typke, D.; Hegerl, R.; Stoschek, A.; Walz, J.; Baumeister, W. *J. Struct. Biol.* **1997**, *120*, 276.
- (23) Lucic, V.; Förster, F.; Baumeister, W. *Annu. Rev. Biochem.* **2005**, *74*, 833.
- (24) McIntosh, R.; Nicastro, D.; Mastronarde, D. *Trends Cell Biol.* **2005**, *15*, 43.
- (25) Koster, A. J.; Barcena, M. Cryotomography: Low-dose Automated Tomography of Frozen-hydrated Specimens. In *Electron Tomography: Methods for Three-Dimensional Visualization of Structures in the Cell*; Frank, J., Ed.; Springer Science+Business Media, LLC, 2006. p 113.
- (26) Midgley, P. A.; Ward, E. P. W.; Hungria, A. B.; Thomas, J. M. *Chem. Soc. Rev.* **2007**, *36*, 1477.
- (27) Möbus, G.; Inkson, B. J. *Mater. Today* **2007**, *10*, 18.
- (28) Radon, J. *Ber. Sächs. Akad. Wiss. Leipzig, Math.-Phys. Kl.* **1917**, *69*, 262.
- (29) Deans, S. R. *The Radon Transform and Some of Its Applications*; John Wiley & Sons, Inc.: New York, 1983, p vii.
- (30) Hounsfield, G. N. *Science* **1980**, *210*, 22.
- (31) Withers, P. J. *Mater. Today* **2007**, *10*, 26.
- (32) Koster, A. J.; Ziese, U.; Verkleij, A. J.; Janssen, A. H.; de Jong, K. P. *J. Phys. Chem. B* **2000**, *104*, 9368.
- (33) de Jong, K. P.; Koster, A. J. *ChemPhysChem* **2002**, *3*, 776.
- (34) Hart, R. G. *Science* **1968**, *159*, 1464.
- (35) Hoppe, W.; Langer, R.; Knesch, G.; Poppe, C. *Naturwissenschaften* **1968**, *55*, 333.
- (36) de Rosier, D. J.; Klug, A. *Nature* **1968**, *217*, 130.
- (37) Bonetta, L. *Nature Methods* **2005**, *2*, 139.
- (38) Zheng, Q. S.; Braunfeld, M. B.; Sedat, J. W.; Agard, D. A. *J. Struct. Biol.* **2004**, *147*, 91.
- (39) Mastronarde, D. N. *J. Struct. Biol.* **2005**, *152*, 36.
- (40) Nickell, S.; Forster, F.; Linaroudis, A.; Net, W. D.; Beck, F.; Hegerl, R.; Baumeister, W.; Plitzko, J. M. *J. Struct. Biol.* **2005**, *149*, 227.
- (41) Radermacher, M. PhD Thesis, Department of Physics, University of Munich, Munich, Germany, 1980.
- (42) Penczek, P. A.; Marko, M.; Buttle, K.; Frank, J. *Ultramicroscopy* **1995**, *60*, 393.
- (43) Mastronarde, D. N. *J. Struct. Biol.* **1997**, *120*, 343.

- (44) Crowther, R. A.; de Rosier, D. J.; Klug, A. *Proc. Roy. Soc. Lond. A* **1970**, *317*, 310.
- (45) Radermacher, M.; Hoppe, W. *Proc. 7th Eur. Congr. Electr. Micr.*, den Haag, The Netherlands 1980; p 132.
- (46) Ziese, U.; de Jong, K. P.; Koster, A. J. *Appl. Catal., A* **2004**, *260*, 71.
- (47) Kübel, C.; Voigt, A.; Schoenmakers, R.; Otten, M.; Su, D.; Lee, T. C.; Carlsson, A.; Bradley, J. *Microsc. Microanal.* **2005**, *11*, 378.
- (48) Abrosimov, O. G.; Moroz, E. M.; Chuvilin, A. L. *Kinet. Catal.* **2006**, *47*, 464.
- (49) Friedrich, H.; Sietsma, J. R. A.; de Jongh, P. E.; Verkleij, A. J.; de Jong, K. P. *J. Am. Chem. Soc.* **2007**, *129*, 10249.
- (50) Penczek, P. A. *J. Struct. Biol.* **2002**, *138*, 34.
- (51) Unser, M.; Sorzano, C. O. S.; Thevenaz, P.; Jonic, S.; El-Bez, C.; De Carlo, S.; Conway, J. F.; Trus, B. L. *J. Struct. Biol.* **2005**, *149*, 243.
- (52) Cardone, G.; Grunewald, K.; Steven, A. C. *J. Struct. Biol.* **2005**, *151*, 117.
- (53) Lawrence, M. C. Least-Squares Method of Alignment using Markers. In *Electron Tomography: Three-Dimensional Imaging with the Transmission Electron Microscope*; Frank, J. Ed., Plenum Press: New York, 1992; p 197.
- (54) Ziese, U.; Janssen, A. H.; Murk, J. L.; Geerts, W. J. C.; Van der Krift, T.; Verkleij, A. J.; Koster, A. J. *J. Microsc.-Oxford* **2002**, *205*, 187.
- (55) Luther, P. K. Sample Shrinkage and Radiation Damage. In *Electron Tomography: Three-Dimensional Imaging with the Transmission Electron Microscope*; Frank, J., Ed.; Plenum press: New York and London, 1992; p 39.
- (56) Jinnai, H.; Nishikawa, Y.; Ikehara, T.; Nishi, T. *Adv. Polymer Sci.* **2004**, *170*, 115.
- (57) Hegerl, R.; Hoppe, W. *Z. Naturforsch., A* **1976**, *31*, 1717.
- (58) McEwan, B. F.; Downing, K. H.; Glaeser, R. M. *Ultramicroscopy* **1995**, *60*, 357.
- (59) Plitzko, J. M.; Baumeister, W. Cryoelectron Tomography (CET). In *Science of Microscopy*; Hawkes, P. W., Spence, J. C. H. Eds.; Springer Science+Business Media, LLC: New York, 2007; Vol. 1, p 535.
- (60) Downing, K. H.; Hendrickson, F. M. *Ultramicroscopy* **1999**, *75*, 215.
- (61) Frank, J.; McEwan, B. F. Alignment by Cross-Correlation. In *Electron Tomography: Three-Dimensional Imaging with the Transmission Electron Microscope*; Frank, J., Ed.; Plenum Press: New York, 1992, p 205.
- (62) Kremer, J. R.; Mastrorade, D. N.; McIntosh, J. R. *J. Struct. Biol.* **1996**, *116*, 71.
- (63) Radermacher, M. Weighted Back-Projection Methods. In *Electron Tomography: Three-Dimensional Imaging with the Transmission Electron Microscope*; Frank, J., Ed.; Plenum Press: New York, 1992, p 91.
- (64) Gilbert, P. *J. Theor. Biol.* **1972**, *36*, 105.
- (65) Gordon, R.; Bender, R.; Herman, G. T. *J. Theor. Biol.* **1970**, *29*, 471.
- (66) Skoglund, U.; Ofverstedt, L.-G.; Burnett, R. M.; Bricogne, G. *J. Struct. Biol.* **1996**, *117*, 173.
- (67) Weyland, M. *Top. Catal.* **2002**, *21*, 175.
- (68) Batenburg, K. J. *Electr. Notes Discrete. Math.* **2005**, *20*, 247.
- (69) Tong, J.; Arslan, I.; Midgley, P. A. *J. Struct. Biol.* **2006**, *153*, 55.
- (70) Bilbao-Castro, J. R.; Merino, A.; Garcia, I.; Carazo, J. M.; Fernandez, J. J. *Parallel Comput.* **2007**, *33*, 250.
- (71) Kuba, A.; Herman, G. T. Some Mathematical Concepts for Tomographic Reconstructions. In *Advanced Tomographic Methods in Materials Research and Engineering*; Banhard, J., Ed.; Oxford University Press: Oxford, 2008, p 19.
- (72) Pettersen, E. F.; Goddard, T. D.; Huang, C. C.; Couch, G. S.; Greenblatt, D. M.; Meng, E. C.; Ferrin, T. E. *J. Comput. Chem.* **2004**, *25*, 1605.

- (73) Ribeiro, E.; Shah, M. *Mach. Vision Appl.* **2006**, *17*, 147.
- (74) Sandberg, K. *Method. Cell Biol.* **2007**, *79*, 769.
- (75) Ohser, J.; Schladitz, K. Visualization and Analysis of Tomographic Data, In *Advanced Tomographic Methods in Materials Research and Engineering*; Banhard, J., Ed.; Oxford University Press: Oxford, 2008, p 37.
- (76) Gommès, C. J.; deJong, K.; Pirard, J. P.; Blacher, S. *Langmuir* **2005**, *21*, 12378.
- (77) Jinnai, H.; Kaneko, T.; Nishioka, H.; Hasegawa, H.; Nishi, T. *Chem. Rec.* **2006**, *6*, 267.
- (78) Ersen, O.; Werckmann, J.; Houille, M.; Ledoux, M. J.; Pham-Huu, C. *Nano Lett.* **2007**, *7*, 1898.
- (79) Ward, E. P. W.; Yates, T. J. V.; Fernandez, J. J.; Vaughan, D. E. W.; Midgley, P. A. *J. Phys. Chem. C* **2007**, *111*, 11501.
- (80) Janssen, A. H.; Koster, A. J.; de Jong, K. P. *Angew. Chem., Int. Ed.* **2001**, *40*, 1102.
- (81) Bals, S.; Van Tendeloo, G.; Kiesielowski, C. *Adv. Mater.* **2006**, *18*, 892.
- (82) Möbus, G.; Inkson, B. J. *Appl. Phys. Lett.* **2001**, *79*, 1369.
- (83) Möbus, G.; Doole, R. C.; Inkson, B. J. *Ultramicroscopy* **2003**, *96*, 433.
- (84) Weyland, M.; Yates, T. J. V.; Dunin-Borkowski, R. E.; Laffont, L.; Midgley, P. A. *Scripta Mater.* **2006**, *55*, 29.
- (85) Gass, M. H.; Koziol, K. K. K.; Windle, A. H.; Midgley, P. A. *Nano Lett.* **2006**, *6*, 376.
- (86) Yurtsever, A.; Weyland, M.; Muller, D. A. *Appl. Phys. Lett.* **2006**, *89*, 151920.
- (87) Lai, G.; Hirayama, T.; Ishizuka, K.; Tanji, T.; Tonomura, A. *Appl. Optics* **1994**, *33*, 829.
- (88) Lai, G.; Hirayama, T.; Fukuhara, A.; Ishizuka, K.; Tanji, T.; Tonomura, A. *J. Appl. Phys.* **1994**, *75*, 4593.
- (89) Twitchett-Harrison, A. C.; Yates, T. J. V.; Newcomb, S. B.; Dunin-Borkowski, R. E.; Midgley, P. A. *Nano Lett.* **2007**, *7*, 2020.
- (90) Barnard, J. S.; Sharp, J.; Tong, J.; Midgley, P. A. *Science* **2006**, *313*, 319.
- (91) Kolb, U.; Gorelik, T.; Kübel, C.; Otten, M. T.; Hubert, D. *Ultramicroscopy* **2007**, *107*, 507.
- (92) Kolb, U.; Gorelik, T.; Otten, M. T. *Ultramicroscopy* **2008**, *108*, 763.
- (93) Kakibayashi, H.; Nakamura, K.; Tsuneta, R.; Mitsui, Y. *Jpn. J. Appl. Phys., Part 1* **1995**, *34*, 5032.
- (94) Friedrich, H.; McCartney, M. R.; Buseck, P. R. *Ultramicroscopy* **2005**, *106*, 18.
- (95) Cervera Gontard, L.; Dunin-Borkowski, R. E.; Chong, R. K. K.; Ozkaya, D.; Midgley, P. A. *J. Phys: Conf. Ser.* **2006**, *26*, 203.
- (96) Weyland, M.; Midgley, P. A.; Thomas, J. M. *J. Phys. Chem. B* **2001**, *105*, 7882.
- (97) Hawkes, P. W. The Electron Microscope as a Structure Projector. In *Electron Tomography: Three-Dimensional Imaging with the Transmission Electron Microscope*; Frank, J. E., Ed.; Plenum Press: New York, 1992, p 17.
- (98) Thomas, J. M.; Midgley, P. A.; Yates, T. J. V.; Barnard, J. S.; Raja, R.; Arslan, I.; Weyland, M. *Angew. Chem., Int. Ed.* **2004**, *43*, 6745.
- (99) Stegmann, H.; Engelmann, H. H.; Zschech, E. *Microelectron. Eng.* **2003**, *65*, 171.
- (100) Kaneko, K.; Nagayama, R.; Inoke, K.; Noguchi, E.; Horita, Z. *Sci. Technol. Adv. Mater.* **2006**, *7*, 726.
- (101) Park, J. B.; Lee, J. H.; Choi, H. R. *Appl. Phys. Lett.* **2007**, *90*, 093111.
- (102) Zhang, H. B.; Zhang, X. L.; Wang, Y.; Takaoka, A. *Rev. Sci. Instrum.* **2007**, *78*, 013701.
- (103) Feng, R.-J.; Watanabe, T.; Takaoka, A. *Proc. Int. Microsc. Conf. 16*, Sapporo, Japan, 2006; p 698.
- (104) Howie, A. *J. Microsc.-Oxford* **1979**, *117*, 11.
- (105) Corma, A. *Chem. Rev.* **1995**, *95*, 559.
- (106) Koster, A. J.; Ziese, U.; Verkleij, A. J.; de Graaf, J.; Geus, J. W.; de Jong, K. P. *Stud. Surf. Sci. Catal.* **2000**, *130*, 329.

- (107) van Donk, S.; Janssen, A. H.; Bitter, J. H.; de Jong, K. P. *Cat. Rev. - Sci. Eng.* **2003**, *45*, 297.
- (108) Tao, Y. S.; Kanoh, H.; Abrams, L.; Kaneko, K. *Chem. Rev.* **2006**, *106*, 896.
- (109) Janssen, A. H.; Koster, A. J.; de Jong, K. P. *J. Phys. Chem. B* **2002**, *106*, 11905.
- (110) Jacobsen, C. J. H.; Madsen, C.; Houzvicka, J.; Schmidt, I.; Carlsson, A. *J. Am. Chem. Soc.* **2000**, *122*, 7116.
- (111) Janssen, A. H.; Schmidt, I.; Jacobsen, C. J. H.; Koster, A. J.; de Jong, K. P. *Microporous Mesoporous Mater.* **2003**, *65*, 59.
- (112) Ogura, M.; Shinomiya, S. Y.; Tateno, J.; Nara, Y.; Kikuchi, E.; Matsukata, H. *Chem. Lett.* **2000**, *29*, 882.
- (113) Groen, J. C.; Bach, T.; Ziese, U.; Paulaime-van Donk, A. M.; de Jong, K. P.; Moulijn, J. A.; Perez-Ramirez, J. *J. Am. Chem. Soc.* **2005**, *127*, 10792.
- (114) Ziese, U.; Gommès, C. J.; Blacher, S.; Janssen, A. H.; Koster, A. J.; de Jong, K. P. *Stud. Surf. Sci. Catal.* **2005**, *158*, 633.
- (115) Kresge, C. T.; Leonowicz, M. E.; Roth, W. J.; Vartuli, J. C.; Beck, J. S. *Nature* **1992**, *359*, 710.
- (116) Zhao, D. Y.; Feng, J. L.; Huo, Q. S.; Melosh, N.; Fredrickson, G. H.; Chmelka, B. F.; Stucky, G. D. *Science* **1998**, *279*, 548.
- (117) Grün, M.; Kurganov, A. A.; Schacht, S.; Schüth, F.; Unger, K. K. *J. Chromatogr. A* **1996**, *740*, 1.
- (118) Mal, N. K.; Fujiwara, M.; Tanaka, Y. *Nature* **2003**, *421*, 350.
- (119) Corma, A. *Chem. Rev.* **1997**, *97*, 2373.
- (120) Schacht, S.; Janicke, M. Schüth, F. *Microporous Mesoporous Mater.* **1998**, *22*, 485.
- (121) Muroyama, N.; Ohsuna, T.; Ryoo, R. Kubota, Y. Terasaki, O. *J. Phys. Chem. C* **2006**, *110*, 10630.
- (122) Kruk, M.; Jaroniec, M.; Ko, C. H.; Ryoo, R. *Chem. Mater.* **2000**, *12*, 1961.
- (123) Ryoo, R.; Ko, C. H.; Kruk, M.; Antochshuk, V.; Jaroniec, M. *J. Phys. Chem. B* **2000**, *104*, 11465.
- (124) Liu, Z.; Terasaki, O.; Ohsuna, T.; Hiraga, K.; Shin, H. J.; Ryoo, R. *Chemphyschem* **2001**, *2*, 229.
- (125) Gommès, C. J.; Friedrich, H.; Wolters, M.; de Jongh, P. E.; de Jong, K. P. *Chem. Mater.* **2009**, *21*, 1311.
- (126) Janssen, A. H.; Van Der Voort, P.; Koster, A. J.; de Jong, K. P. *Chem. Commun.* **2002**, 1632.
- (127) Martines, M. U.; Yeong, E.; Persin, M.; Larbot, A.; Voorhout, W. F.; Kübel, C. K. U.; Kooyman, P.; Prouzet, E. *C.R. Chim.* **2005**, *8*, 627.
- (128) Yao, Y.; Czymmek, K. J.; Pazhianur, R.; Lenhoff, A. M. *Langmuir* **2006**, *22*, 11148.
- (129) Wang, H.; Zhou, X.; Yu, M.; Wang, Y.; Han, L.; Zhang, J.; Yuan, P.; Auchterlonie, G.; Zou, J.; Yu, C. *J. Am. Chem. Soc.* **2006**, *128*, 15992.
- (130) Han, Y.; Zhao, L.; Ying, J. Y. *Adv. Mater.* **2007**, *19*, 2454.
- (131) Yuan, P.; Liu, N.; Zhao, L. Z.; Zhou, X. F.; Zhou, L.; Auchterlonie, G. J.; Yao, X. D.; Drennan, J.; Lu, G. Q.; Zou, J.; Yu, C. *Z. Angew. Chem., Int. Ed.* **2008**, *47*, 6670.
- (132) Ersen, O.; Parmentier, J.; Solovyov, L. A.; Drillon, M.; Pham-Huu, C.; Werckmann, J.; Schultz, P. *J. Am. Chem. Soc.* **2008**, *130*, 16800.
- (133) Vercaemst, C.; Friedrich, H.; de Jongh, P. E.; Neimark, A. V.; Goderis, B.; Verpoort, F.; van der Voort, P. *J. Phys. Chem. C* **2009**, accepted.
- (134) Yates, T. J. V.; Thomas, J. M.; Fernandez, J. J.; Terasaki, O.; Ryoo, R.; Midgley, P. A. *Chem. Phys. Lett.* **2006**, *418*, 540.
- (135) Sakamoto, Y.; Kim, T. W.; Ryoo, R.; Terasaki, O. *Angew. Chem., Int. Ed.* **2004**, *43*, 5231.
- (136) Garcia-Bennett, A. E.; Che, S. N.; Miyasaka, K.; Sakamoto, Y.; Ohsuna, T.; Liu, Z.; Terasaki, O. *Stud. Surf. Sci. Catal.* **2005**, *156*, 11.
- (137) Gao, C. B.; Sakamoto, Y.; Sakamoto, K.; Terasaki, O.; Che, S. N. *Angew. Chem., Int. Ed.* **2006**, *45*, 4295.
- (138) Sietsma, J. R. A.; de Jongh, P. E.; van Dillen, A. J.; de Jong, K. P. *Stud. Surf. Sci. Catal.* **2006**, *162*, 95.

- (139) Ciesla, U.; Schüth, F. *Microporous Mesoporous Mater.* **1999**, *27*, 131.
- (140) Midgley, P. A.; Weyland, M.; Thomas, J. M.; Johnson, B. F. G. *Chem. Commun.* **2001**, 907.
- (141) Midgley, P. A.; Thomas, J. M.; Laffont, L.; Weyland, M.; Raja, R.; Johnson, B. F. G.; Khimyak, T. *J. Phys. Chem. B* **2004**, *108*, 4590.
- (142) Thomas, J. M.; Raja, R.; Johnson, B. F. G.; Hermans, S.; Jones, M. D.; Khimyak, T. *Ind. Eng. Chem. Res.* **2003**, *42*, 1563.
- (143) Janssen, A. H.; Yang, C. M.; Wang, Y.; Schuth, F.; Koster, A. J.; de Jong, K. P. *J. of Phys. Chem. B* **2003**, *107*, 10552.
- (144) Sietsma, J. R. A.; Friedrich, H.; Broersma, A. Versluijs-Helder, M.; van Dillen, A. J.; de Jongh, P. E.; de Jong, K. P. *J. Catal.* **2008**, *260*, 227.
- (145) Ersen, O.; Hirlimann, C.; Drillon, A.; Werckmann, J.; Tihay, F.; Pham-Huu, C.; Crucifix, C.; Schultz, P. *Solid State Sci.* **2007**, *9*, 1088.
- (146) Thiruvengadathan, R.; Levi-Kalishman, Y.; Regev, O. *Curr. Opin. Colloid Interface Sci.* **2005**, *10*, 280.
- (147) Li, Z.; Kübel, C.; Parvulescu, V. I.; Richards, R. *ACS Nano* **2008**, *2*, 1205.
- (148) Yamauchi, Y.; Takai, A.; Nagaura, T.; Inoue, S.; Kuroda, K. *J. Am. Chem. Soc.* **2008**, *130*, 5426.
- (149) Fujita, T.; Qian, L. H.; Inoke, K.; Erlebacher, J.; Chen, M. W. *Appl. Phys. Lett.* **2008**, *92*, 251902.
- (150) Verheijen, M. A.; Algra, R. E.; Borgström, M. T.; Immink, G.; Sourty, E.; van Enckevort, W. J. P.; Vlieg, E.; Bakkers, E. P. A. M. *Nano Lett.* **2007**, *7*, 3051.
- (151) Kim, H. S.; Hwang, S. O.; Myung, Y.; Park, J.; Bae, S. Y.; Ahn, J. P. *Nano Lett.* **2008**, *8*, 551.
- (152) Hungria, A. B.; Raja, R.; Adams, R. D.; Captain, B.; Thomas, J. M.; Midgley, P. A.; Golovko, V.; Johnson, B. F. G. *Angew. Chem., Int. Ed.* **2006**, *45*, 4782.
- (153) de Jong, K. P.; van den Oetelaar, L. C. A.; Vogt, E. T. C.; Eijsbouts, S.; Koster, A. J.; Friedrich, H.; de Jongh, P. E. *J. Phys. Chem. B* **2006**, *110*, 10209.
- (154) Raybaud, P. *Appl. Catal., A* **2007**, *322*, 76.
- (155) Bar Sadan, M.; Houben, L.; Wolf, S. G.; Enyashin, A.; Seifert, G.; Tenne, R.; Urban, K. *Nano Lett.* **2008**, *8*, 891.
- (156) Arslan, L.; Walmsley, J. C.; Rytter, E.; Bergene, E.; Midgley, P. A. *J. Am. Chem. Soc.* **2008**, *130*, 5716.
- (157) Midgley, P. A.; Weyland, M.; Thomas, J. M.; Gai, P. L.; Boyes, E. D. *Angew. Chem., Int. Ed.* **2002**, *41*, 3804.
- (158) Cervera Gontard, L.; Dunin-Borkowski, R. E.; Ozkaya, D.; Hyde, T.; Midgley, P. A.; Ash, P. *J. Phys. Conf. Ser.* **2006**, *26*, 367.
- (159) Wikander, K.; Hungria, A. B.; Midgley, P. A.; Palmqvist, A. E. C.; Holmberg, K.; Thomas, J. M. *J. Colloid Interface Sci.* **2007**, *305*, 204.
- (160) Gallezot, P.; Richard, D. *Cat. Rev. - Sci. Eng.* **1998**, *40*, 81.
- (161) Liu, Z. L.; Hong, L.; Tham, M. P.; Lim, T. H.; Jiang, H. X. *J. Power Sources* **2006**, *161*, 831.
- (162) Uchida, H.; Song, J. M.; Suzuki, S.; Nakazawa, E.; Baba, N.; Watanabe, M. *J. Phys. Chem. B* **2006**, *110*, 13319.
- (163) Drennan, J.; Webb, R.; Nogita, K.; Knibbe, R.; Auchterlonie, G.; Tatenuma, K.; Hunter, J. *Solid State Ionics* **2006**, *177*, 1649.
- (164) Yoshizawa, N.; Tanaike, O.; Hatori, H.; Yoshikawa, K.; Kondo, A.; Abe, T. *Carbon* **2006**, *44*, 2558.
- (165) Long, J. W.; Dunn, B.; Rolison, D. R.; White, H. S. *Chem. Rev.* **2004**, *104*, 4463.
- (166) Ebbesen, T. W. Properties: Experimental Results. In *Carbon Nanotubes, Preparation and Properties*; Ebbesen, T. W., Ed., CRC Press: New York, 1997. p 225.
- (167) Iijima, S. *Nature* **1991**, *354*, 56.
- (168) Kizuka, T.; Sumi, T.; Bansho, S.; Saito, T. *Jpn. J. Appl. Phys., Part 2* **2001**, *40*, L56.

- (169) Bals, S.; Batenburg, K. J.; Verbeeck, J.; Sijbers, J.; Van Tendeloo, G. *Nano Lett.* **2007**, *7*, 3669.
- (170) Cha, J. J.; Weyland, M.; Briere, J. F.; Daykov, I. P.; Arias, T. A.; Muller, D. A. *Nano Lett.* **2007**, *7*, 3770.
- (171) Pan, X. L.; Fan, Z. L.; Chen, W.; Ding, Y. J.; Luo, H. Y.; Bao, X. H. *Nat. Mater.* **2007**, *6*, 507.
- (172) Ersen, O.; Begin, S.; Houille, M.; Amadou, J.; Janowska, I.; Greneche, J.-M.; Crucifix, C.; Pham-Huu, C. *Nano Lett.* **2008**, *8*, 1033.
- (173) Jacoby, M. *Chem. Eng. News* **2008**, *86*, 31.
- (174) Numata, M.; Asai, M.; Kaneko, K.; Bae, A. H.; Hasegawa, T.; Sakurai, K.; Shinkai, S. *J. Am. Chem. Soc.* **2005**, *127*, 5875.
- (175) Yu, J. R.; Lu, K. B.; Sourty, E.; Grossiord, N.; Konine, C. E.; Loos, J. C. *Carbon* **2007**, *45*, 2897.
- (176) Bond, T. C.; Streets, D. G.; Yarber, K. F.; Nelson, S. M.; Woo, J. H.; Klimont, Z. *J. Geophys. Res.* **2004**, *109*, D14203.
- (177) Hansen, J.; Sato, M.; Ruedy, R.; Lacin, A.; Oinas, V. P. *Natl. Acad. Sci. USA* **2000**, *97*, 9875.
- (178) Jacobson, M. Z. *J. Geophys. Res.* **2001**, *106*, 1551.
- (179) van Poppel, L. H.; Friedrich, H.; Spinsby, J.; Chung, S. H.; Seinfeld, J. H.; Buseck, P. R. *Geophys. Res. Lett.* **2005**, *32*, L24811.
- (180) Adachi, K.; Chung, S. H.; Friedrich, H.; Buseck, P. R. *J. Geophys. Res.* **2007**, *112*, D14202.
- (181) Coronas, J.; Santamaria, J. *Catal. Today* **1999**, *51*, 377.
- (182) Keane, M. A. *J. Mater. Sci.* **2003**, *38*, 4661.
- (183) Yoshida, K.; Nanbara, T.; Yamasaki, J.; Tanaka, N. *J. Appl. Phys.* **2006**, *99*, 084908.
- (184) Kaneko, K.; Nagayama, R.; Inoke, K.; Noguchi, E.; Horita, Z. *Sci. Technol. Adv. Mater.* **2006**, *7*, 726.
- (185) Reddy, B. M.; Thrimurthulu, G.; Saikia, P.; Bharali, P. *J. Mol. Catal. A: Chem.* **2007**, *275*, 167.
- (186) Simonsen, S. B.; Dahl, S.; Johnson, E.; Helveg, S. *J. Catal.* **2008**, *255*, 1.
- (187) Kaspar, J.; Fornasiero, P.; Hickey, N. *Catal. Today* **2003**, *77*, 419.
- (188) Fornasiero, P.; Montini, T.; Graziani, M.; Kaspar, J.; Hungria, A. B.; Martinez-Arias, A.; Conesa, J. C. *Phys. Chem. Chem. Phys.* **2002**, *4*, 149.
- (189) Hernandez, J. C.; Hungria, A. B.; Perez-Omil, J. A.; Trasobares, S.; Bernal, S.; Midgley, P. A.; Alavi, A.; Calvino, J. J. *J. Phys. Chem. C* **2007**, *111*, 9001.
- (190) Kaneko, K.; Inoke, K.; Freitag, B.; Hungria, A. B.; Midgley, P. A.; Hansen, T. W.; Zhang, J.; Ohara, S.; Adschiri, T. *Nano Lett.* **2007**, *7*, 421.
- (191) Xu, X.; Saghi, Z.; Yang, G.; Hand, R. J.; Möbus, G. *Cryst. Growth Des.* **2008**, *8*, 1102.
- (192) Bergbreiter, D. E. *Curr. Opin. Drug Discov. Devel.* **2001**, *4*, 736.
- (193) van de Coevering, R.; Gebbink, R. J. M. K.; van Koten, G. *Prog. Polym. Sci.* **2005**, *30*, 474.
- (194) Spontak, R. J.; Williams, M. C.; Agard, D. A. *Polymer* **1988**, *29*, 387.
- (195) Radzilowski, L. H.; Carragher, B. O.; Stupp, S. I. *Macromolecules* **1997**, *30*, 2110.
- (196) Sugimori, H.; Nishi, T.; Jinnai, H. *Macromolecules* **2005**, *38*, 10226.
- (197) Spontak, R. J.; Fung, J. C.; Braunfeld, M. B.; Sedat, J. W.; Agard, D. A.; Ashraf, A.; Smith, S. D. *Macromolecules* **1996**, *29*, 2850.
- (198) Ikehara, T.; Jinnai, H.; Kaneko, T.; Nishioka, H.; Nishi, T. *J. Polym. Sci., Part B: Polym. Phys.* **2007**, *45*, 1122.
- (199) Kato, M.; Ito, T.; Aoyama, Y.; Sawa, K.; Kaneko, T.; Kawase, N.; Jinnai, H. *J. Polym. Sci., Part B: Polym. Phys.* **2007**, *45*, 677.
- (200) Yamauchi, K.; Takahashi, K.; Hasegawa, H.; Iatrou, H.; Hadjichristidis, N.; Kaneko, T.; Nishikawa, Y.; Jinnai, H.; Matsui, T.; Nishioka, H.; Shimizu, M.; Furukawa, H. *Macromolecules* **2003**, *36*, 6962.
- (201) Takano, A.; Wada, S.; Sato, S.; Araki, T.; Hirahara, K.; Kazama, T.; Kawahara, S.; Isono, Y.; Ohno, A.; Tanaka, N.; Matsushita, Y. *Macromolecules* **2004**, *37*, 9941.

- (202) Hashimoto, T.; Tsutsumi, K.; Funaki, Y. *Langmuir* **1997**, *13*, 6869.
- (203) Schneider, G. J.; Fink, S. A.; Rachel, R.; Goritz, D. *Kautsch. Gummi Kunstst.* **2005**, *58*, 461.
- (204) Jinnai, H.; Shinbori, Y.; Kitaoka, T.; Akutagawa, K.; Mashita, N.; Nishi, T. *Macromolecules* **2007**, *40*, 6758.
- (205) Nishioka, H.; Niihara, K. I.; Kaneko, T.; Yamanaka, J.; Inoue, T.; Nishi, T.; Jinnai, H. *Compos. Interface.* **2006**, *13*, 589.
- (206) Kawase, N.; Kato, M.; Nishioka, H.; Jinnai, H. *Ultramicroscopy* **2007**, *107*, 8.
- (207) Treacy, M. M. J.; Newsam, J. M. *Nature* **1988**, *332*, 249.
- (208) Lin, Y.; Boker, A.; He, J. B.; Sill, K.; Xiang, H. Q.; Abetz, C.; Li, X. F.; Wang, J.; Emrick, T.; Long, S.; Wang, Q.; Balazs, A.; Russell, T. P. *Nature* **2005**, *434*, 55.
- (209) Arslan, I.; Yates, T. J. V.; Browning, N. D.; Midgley, P. A. *Science* **2005**, *309*, 2195.
- (210) Haider, M.; Uhlemann, S.; Schwan, E.; Rose, H.; Kabius, B.; Urban, K. *Nature* **1998**, *392*, 768.
- (211) Krivanek, O. L.; Dellby, N.; Lupini, A. R. *Ultramicroscopy* **1999**, *78*, 1.
- (212) Smith, D. J. *Microsc. Microanal.* **2008**, *14*, 2.
- (213) Jinschek, J. R.; Batenburg, K. J.; Calderon, H. A.; Kilaas, R.; Radmilovic, V.; Kisielowski, C. *Ultramicroscopy* **2008**, *108*, 589.

Chapter 3

An Electron Tomography Study of NiO supported on SBA-15 obtained by thermal Decomposition of Nickel Nitrate in different Gas Atmospheres

Abstract

The 3D morphology of NiO/SBA-15 catalysts, prepared by thermally decomposing nickel nitrate supported on SBA-15 in different gas atmospheres, was studied. Electron tomography (ET) clearly showed that rod-like NiO particles, which were confined by the corrugated silica walls, had formed in air and He atmospheres. In He a large number of small and more spherical NiO particles were present too. Blocking of pores by NiO rods explained the two-step desorption in the N₂-physisorption isotherms. After thermal decomposition in an atmosphere of 1 vol % NO in He, no rod-like NiO or pore blocking was observed. The presence of oxygen and in particular high concentrations of decomposition products was connected to a severe redistribution and sintering of the nickel phase. Transport to the support exterior resulted in NiO particles that were in most instances porous and connected by bridges through the micropores of the silica wall to NiO in adjacent SBA-15 mesopores.

3.1 Introduction

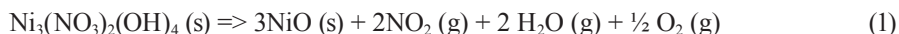
Supported metal (oxide) catalysts are essential to modern life and have a significant impact on the industrial production of chemicals, transportation fuels, drugs, and food.¹⁻³ Nickel based catalysts belong to the most widely used as a result of their activity in many important (de)hydrogenation reactions.⁴⁻⁶ One central objective in catalyst preparation is to achieve a high dispersion of the active phase at high loadings, which is equivalent to maximizing the active surface area per unit weight of catalyst. Relevant approaches are mainly based on liquid phase processes, such as ion adsorption⁷⁻⁹, deposition-precipitation⁹⁻¹² and impregnation and drying.¹³⁻¹⁵

In particular impregnation and drying permits high loadings in a technically simple manner, and has been widely implemented on an industrial scale. Preparation is carried out by impregnation of pre-shaped catalyst support bodies with a precursor-containing solution followed by drying.¹⁶ Dried impregnates are subsequently heat treated in air (calcination) to convert the precursor into the desired metal oxide, or into the metal when followed by a high temperature reduction. Although a large number of precursors can be employed, metal nitrates are very attractive since they are cost-effective and highly soluble so that high loadings can be achieved via a single step impregnation.¹⁷ In addition, the nitrate is completely removed during thermal decomposition leading to pure metal oxides. Unfortunately, a poorly dispersed active phase is often obtained.¹⁸⁻²¹

The reasons for poor catalyst dispersion are not well understood since the underlying processes, e.g. of impregnation and drying, are very complex.²² Fundamental studies, separating the effects of each preparation step, are complicated by the heterogeneity of conventional support materials and therefore are best carried out on well-defined model systems.^{23,24} In this respect ordered mesoporous silica (OMS), like MCM-41²⁵ or SBA-15²⁶, have attracted much attention as model supports.^{15,27,28} Resulting from their tunable and well-defined pore geometry, characterization by N₂ physisorption yields detailed information on the presence and morphology of guest phases.^{29,30} Commonly these results are complemented by X-ray diffraction (XRD) to measure the average crystallite size and transmission electron microscopy (TEM) to study the active phase distribution.^{24,31}

Similarly to conventional silica supports, many studies reported an inhomogeneous distribution of the metal (oxide) phase within the pores of the OMS support.³²⁻³⁴ Non-uniform filling of OMS pores could be related to non-uniform wetting during impregnation since OMS have a relatively low surface hydroxyl density (1-3 OH nm⁻²)^{35,36} as compared to conventional silica (4-6 OH nm⁻²).³⁷ Furthermore, poor nickel oxide dispersion has also been associated either with redistribution during drying^{23,38} or sintering and redistribution during heat treatment in air.³⁹

The conversion from aqueous nickel nitrate solution to NiO proceeds in two steps: (i) formation of a basic nickel nitrate upon drying, and (ii) formation of NiO upon thermal decomposition (Equation 1).³⁸



Inhomogeneous wetting and drying phenomena caused the basic nickel nitrate to be deposited in only a fraction of the available SBA-15 pores.³⁹ Nevertheless, no basic nickel nitrate was present on the outer surface of the support. Subsequent thermal decomposition of the dried precursor into nickel oxide showed that the final dispersion and distribution was strongly linked to the gas atmosphere during heat treatment.⁴⁰ While nanoscale characterization of the nickel oxide dispersion and distribution is commonly carried out by TEM, interpretation of electron micrographs is hampered by the fact that they are in first approximation 2D projections of a 3D structure. In contrast, electron tomography (ET), which utilizes multiple TEM images from different viewing directions, can resolve the actual 3D structure and is thus particularly suitable for local nanoscale investigations.

In the following study ET is applied to NiO/SBA-15 catalysts to reveal the final 3D distribution and morphology of the NiO particles after thermal decomposition of the nickel nitrate as a function of the gas atmosphere (air, He, 1 vol% NO in He). Nanoscale findings on the level of individual SBA-15 pores are complemented and discussed in context of bulk characterization by XRD and N₂-physisorption.

3.2 Experimental

3.2.1 Sample preparation

SBA-15 (total pore volume 0.78 cm³ g⁻¹ and average pore diameter 9 nm) was synthesized according to the procedure described by Zhao et al.²⁶ In short, 8 g of poly(ethylene oxide)₂₀poly(propylene oxide)₇₀poly(ethylene oxide)₂₀ tri-block copolymer (Aldrich) was dissolved in 250 ml demineralized water at 40 °C.

After a clear solution was obtained, first 48 g of concentrated HCl (Merck), and second 21.5 ml of tetraethyl orthosilicate (Acros) were added. Following stirring for 20 hours at 40 °C, the suspension was placed in an oven at 80 °C for 48 hours. The solid product was filtered from the suspension, washed, dried in air for 12 hours at 80 °C, and calcined for 6 hours at 550 °C.

Impregnation was carried out from a 4.2 M precursor solution containing $\text{Ni}(\text{NO}_3)_2 \cdot 6\text{H}_2\text{O}$ (Acros) dissolved in de-mineralized water. Dried supports (2 h at 80 °C in dynamic vacuum) were impregnated in static vacuum using 1.00 ml g^{-1} to provide 24 wt% or 0.75 ml g^{-1} to provide 19 wt% NiO/SBA-15. Drying of the fresh impregnates proceeded in static air while increasing the temperature at a rate of 1 °C min^{-1} to 120 °C where it was kept for an additional 12 hours.

Small portions (40 mg) of the dried impregnates were decomposed in an atmosphere of air, He, or 1 vol % NO in He using a plug flow reactor (17 cm length and 1 cm diameter). Samples were heated in a gas flow of 90 ml/min at a rate of 1 °C min^{-1} to 450 °C where they were kept for an additional 4 hours before cooling down. Thermal decomposition in stagnant air was carried out by heating 250 mg of the dried impregnate in an oven dish (62 cm^3) with a loose lid on top to minimize removal of the decomposition products. Heating proceeded at a rate of 1 °C min^{-1} to 450 °C where the sample was kept for an additional 4 hours before cooling down.

Samples were labeled S24NiO_{air}, S24NiO_{He}, S24NiO_{NO/He}, and S19NiO_{stagnant}, where S24NiO denotes SBA-15 support and 24 wt% NiO loading supplemented by the gas atmosphere during thermal decomposition in subscript. Sample code S24_{dried} refers to the dried impregnate.

3.2.2 Characterization

Powder X-ray diffraction measurements were performed at room temperature with a Bruker-AXS D8 Advance diffractometer using $\text{Co-K}_{\alpha 1,2}$ radiation with a wavelength of 0.179 nm. Powder XRD patterns were collected over an angular range of 5° to 90° 2 θ and baseline-corrected for the amorphous silica background. The average NiO crystallite sizes were calculated from the broadening of the three diffraction lines ((111) at 2 θ =43.6°; (200) at 2 θ =50.8°; (220) at 2 θ =74.6°) using the Scherrer Equation with $k=1$.

N_2 -physisorption isotherms were recorded at -196 °C using a Micromeritics TriStar 3000). Samples were dried preceding measurements in a flow of He at 120 °C for 14 hours. The pore size distribution was calculated from the adsorption branch of the isotherms by non-local density functional theory (NL-DFT) using a model for ordered mesoporous silica supports with cylindrical pore geometry developed by Jaroniec *et al.*⁴² The SBA-15 mesopore diameter was defined by the value at the point of maximum differential pore volume. For determination of the blocked mesopore volume we used the desorption branch of the isotherm in combination with BJH theory⁴³, the Harkins-Jura thickness equation⁴⁴, and the Kruk-Jaroniec-Sayari correction for OMS supports⁴⁵ to calculate the cumulative pore volume as a function of the pore size. The volume contained in pores with an apparent pore diameter between 2-5 nm in the BJH plot was considered as blocked mesopore volume. ET samples were prepared by first applying 10 nm colloidal gold particles from suspension to a Quantifoil R2/1 lacey carbon support film on a 200 mesh Cu parallel bar TEM grid.

Following drying of the grid in air, a small amount of the catalyst powder was directly deposited onto the carbon film. After shaking-off excess material, the grid was inserted into a Fischione advanced tomography holder (model 2020).

ET was performed in bright-field TEM and in high-angle annular dark-field (HAADF) STEM mode on Tecnai 20 electron microscopes, operated at 200kV. The microscopes were equipped with TWIN objective lenses and a LaB₆ or a field emission (FEG) electron source. Series of images (tilt-series) were acquired by rotating the specimen in the electron beam over an angular range of at least $\pm 70^\circ$ at 1° or 2° increments. Images were recorded either on a 2048 x 2048 pixel TVIPS CCD camera or on a Fischione HAADF STEM detector using Xplore3D (FEI) software. Changes in object position and defocus were corrected at each step of the series. The defocus was set in TEM mode between -90 nm and -200 nm depending on the size of the SBA-15 particle to keep the entire object in underfocus. HAADF STEM was performed with the sample in focus and using a camera length of 120 mm or 150 mm. Images of the tilt-series were aligned with respect to a common origin and rotation axis using the 10 nm gold particles as fiducial markers. Alignment, reconstruction by filtered backprojection, and denoising were performed in IMOD.⁴⁶ Denoising was done by nonlinear anisotropic diffusion⁴⁷ and visualization was carried out in Amira 3.1 (TGS-Visual Concepts/Mercury Computer Systems, Inc). Quantitative analysis of the tomograms of sample S19NiO_{stagnant} was performed in Matlab (The MathWorks, Inc.) using in part functions of the TOM toolbox⁴⁸ and the DIPimage library (www.diplib.org). A detailed description of the image analysis procedure is presented in chapter 5, section 5.3 on page 82.

Experiments by environmental TEM were performed at the John M. Cowley Center for High Resolution Electron Microscopy, Arizona State University, on a Tecnai 20 electron microscope. The microscope was equipped with an environmental cell allowing gases to be present during thermal decomposition of the sample. The dried impregnate was directly deposited on a carbon support film on a 200 mesh Ti grid or on the bars of a Pt mesh, and subsequently heated in-situ at a rate of 1 and 5 °C min⁻¹ to 300-400 °C in 5 or 50 mbar of O₂. TEM images of multiple SBA-15 particles were taken at 20 °C or 150 °C and at 300-400 °C, while a single particle was followed during the entire heating process.

3.3 Results and Discussion

In the first section (3.3.1) the impact of the gas atmosphere during heat treatment on the resulting NiO distribution will be discussed based on TEM, XRD and N_2 physisorption results. The remaining sections (3.3.2–3.3.4) give an in depth analysis of the observed NiO and SBA-15 morphologies as a function of gas atmosphere in context of ET findings.

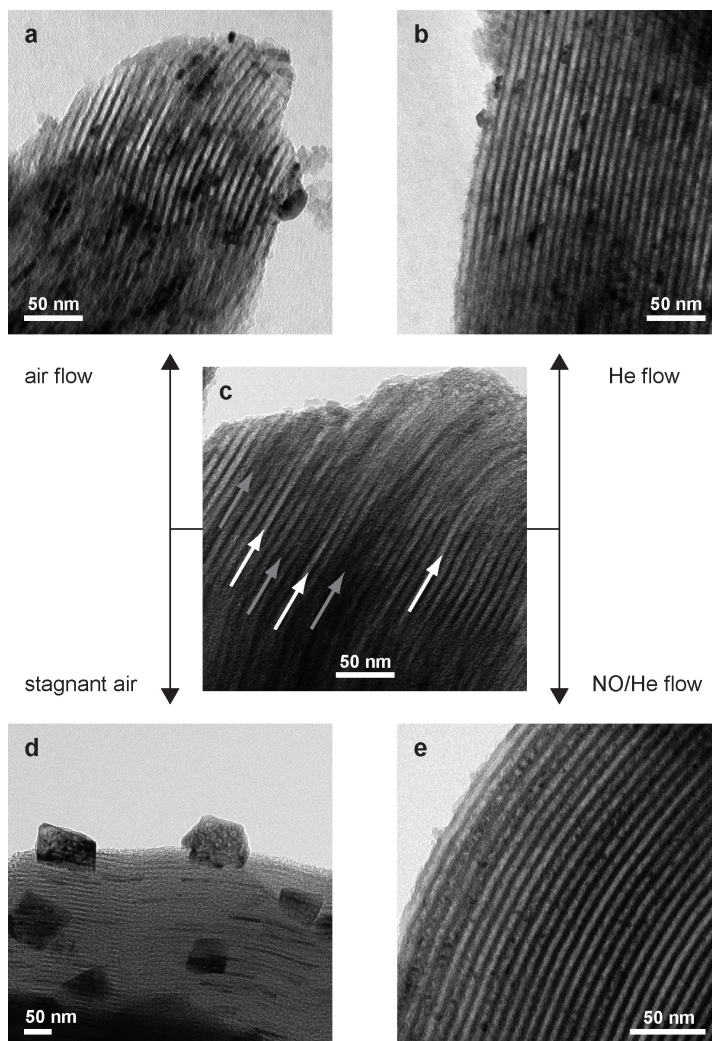


Figure 1 Bright-field TEM image of the dried impregnate ($S24_{\text{dried}}$) with gray arrows indicating nickel nitrate filled mesopores and white arrows empty ones (c). TEM images of heat treated impregnate using different gas atmospheres $S24NiO_{\text{Air}}$ (a), $S24NiO_{\text{He}}$ (b), $S19NiO_{\text{stagnant}}$ (d), and $S24NiO_{\text{NO/He}}$ (e).

3.3.1 Bulk Characterization and TEM

Figure 1 displays representative electron micrographs of the examined samples. As seen in Figure 1c, the basic nickel nitrate was non-uniformly distributed in the mesopores of SBA-15 at the same time preserving the ordered pore structure upon impregnation and drying. After thermal decomposition in air (Figure 1a,d), rod-like NiO particles and NiO on the external surface of the support were observed. While decomposition in stagnant air led to very large external NiO particles (Figure 1d), flow conditions (Figure 1a) limited transport of the nickel phase to the outer surface of the support. Decomposition in He flow (Figure 1b) produced rod-like NiO particles inside the pores of SBA-15. In contrast, a flow of 1 vol% NO in He (Figure 1e) prevented formation of NiO rods and redistribution to the exterior.

The results of bulk characterization by XRD and N₂-physisorption are shown in Figure 2. Broadening of the (111), (200), and (220) NiO diffraction peaks (Figure 2a) correlates well with the TEM findings. Decomposition in stagnant air formed the largest NiO particles (25 nm Scherrer diameter) with the most narrow diffraction peaks, followed by air flow (10 nm), and He flow (8 nm). The broadest peaks were observed for a 1 vol% NO in He flow corresponding to ~4 nm NiO particles. The N₂ physisorption isotherms (Figure 2b) displayed for all samples, except the NO/He treated one, a desorption step at $p/p_0=0.48$. This feature has been associated with the blocking of mesopores^{33,49}, in this case presumably caused by the rod-like NiO particles. Closed-off pore sections (cavities) remain filled upon lowering the pressure until spontaneous cavitation of the condensed N₂ through the micropores in the silica wall occurs.⁵⁰ While after decomposition in air and He flow most mesopores were blocked, enhanced transport of the nickel phase to the exterior support surface in stagnant air reduced the likelihood of forming cavities. In the case of a NO/He flow no blocking was observed, suggesting that only NiO particles much smaller than the pore diameter were present.

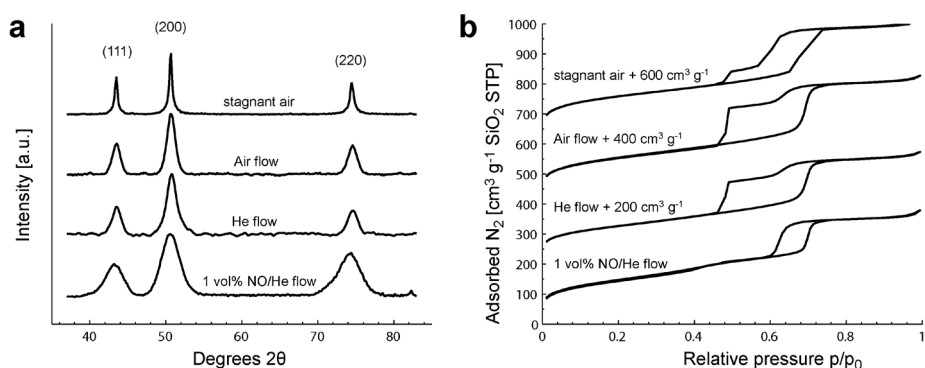


Figure 2 XRD patterns (a) and N₂ physisorption isotherms (b) of NiO/SBA-15 catalysts synthesized via thermal decomposition of nickel nitrate in different gas atmospheres.³⁹

TEM and bulk characterization results, presented above, describe some of the structural features of the examined samples but are limited. For instance, TEM images are in first approximation two dimensional projections of an originally three-dimensional structure hence the location of objects is ambiguous. In contrast, ET allows a detailed analysis of the NiO particle morphology and distribution down to the level of individual SBA-15 pores as is illustrated in the following sections.

3.3.2 Thermal decomposition in Air flow

In Figure 3 numerical cross-sections (ET slices) through two different SBA-15 particles of sample S24NiO_{Air} are displayed. The ordered mesopores of SBA-15 were well resolved and NiO was present inside the pores and on the exterior surface of the SBA-15 particle. The NiO particles inside the mesopores were confined by the pore walls and therefore rod-like. The rod diameter was approximately 9 nm matching the pore diameter of the SBA-15 support obtained from N₂ physisorption. The length of the NiO rods varied between 10 and 70 nm. This value exceeds the Scherrer diameter of 10 nm due to the elongated geometry and the particles most likely polycrystalline nature. NiO particles on the support exterior had a diameter of approximately 10-40 nm.

Figure 4 displays the ET results from an analysis of the tomograms on the scale of individual SBA-15 pores. Blocking of SBA-15 mesopores by pairs of rod-like NiO particles, confined within the same pore thus forming a cavity, was observed in many instances. These cavities, blocked only as far as the mesopores are concerned, are accessible to nitrogen through the micropores in the silica wall as observed in the N₂ physisorption isotherm in Figure 2. Physisorption revealed that 74% of mesopore volume was blocked, i.e. volume in cavities. In addition to the NiO nanorods, collapsed pore walls might also contribute to the creation

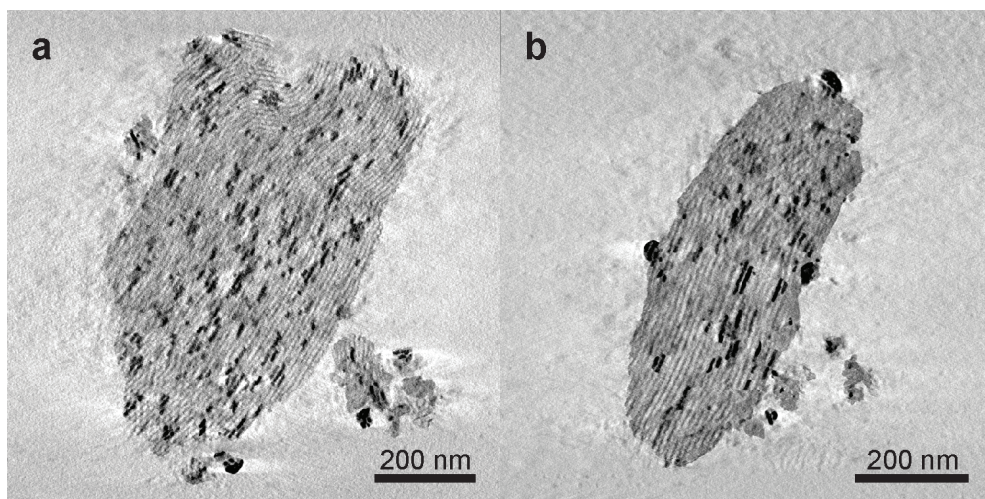


Figure 3 ET slices through two different SBA-15 particles of sample S24NiO_{Air}.

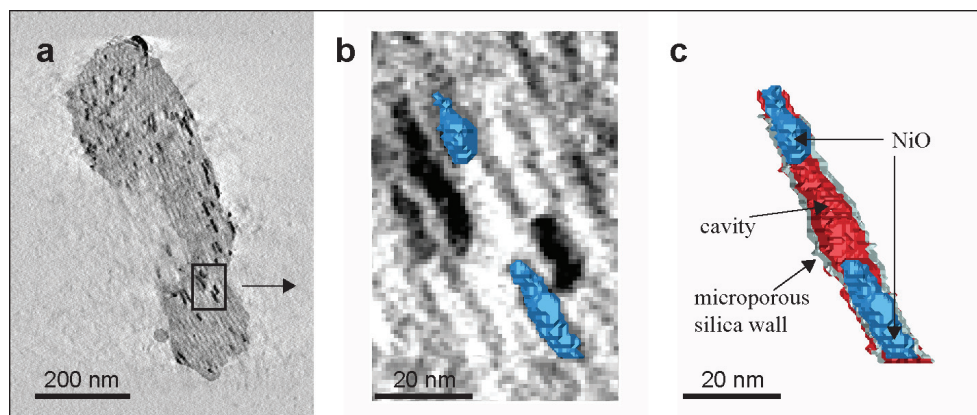


Figure 4 ET slice of sample S24NiO_{air} (a), magnified region with two segmented NiO particles (blue) located in the same pore (b), segmented cavity formed between two NiO rods (c).

of cavities. Thermal decomposition in air flow led to fragmented SBA-15 particles (Figure 3), exposing partially collapsed pores (Figure 5a). Differential scanning calorimetry (DSC) results, published elsewhere³⁹, showed a very sharp peak upon heating, indicating a rapid decomposition of the basic nickel nitrate. Fast formation of gaseous decomposition products in combination with transport and sintering of the nickel phase might explain the partial collapse of the pore walls.

Contrary to pore collapse, corrugation of the silica walls is a characteristic feature of the SBA-15 mesopore channels.⁵¹ As seen in Figure 5b, pore wall corrugation led, as a result of confinement, to corrugated NiO particles. These findings are supported by earlier reports on Pt⁵² and Co₃O₄⁵³ replicas of SBA-15 in which TEM showed the curved outline of the obtained nanorods. Notably, the NiO particles on the support exterior and some NiO nanorods appeared to be porous (Figure 5a,b) which was also found for Co₃O₄.⁵³

Figure 5c-e display a surface representation of manually segmented NiO particles revealing their complex morphology. The NiO particles confined within the pores were only in first approximation rod-like, showing protrusions and pockets. NiO particles in neighboring pores were connected by bridges through the micropores in the silica walls of SBA-15. Similar connections have been inferred from TEM for Pt⁵² and metal oxide⁵⁴ replicas after silica removal. In addition, the NiO particle on the SBA-15 exterior (shown in red in Figure 5c-e) was also connected to the NiO in adjacent pores.

The arrangement of NiO-filled SBA-15 mesopores, connecting bridges, and NiO on the support exterior was observed in most instances. This suggests that transport of the nickel phase to the exterior of the SBA-15 particle might have commenced through the micropores of the silica walls. A detailed discussion of this hypothesis will be given in context of thermal decomposition in stagnant air which displays the most significant transport of the nickel phase.

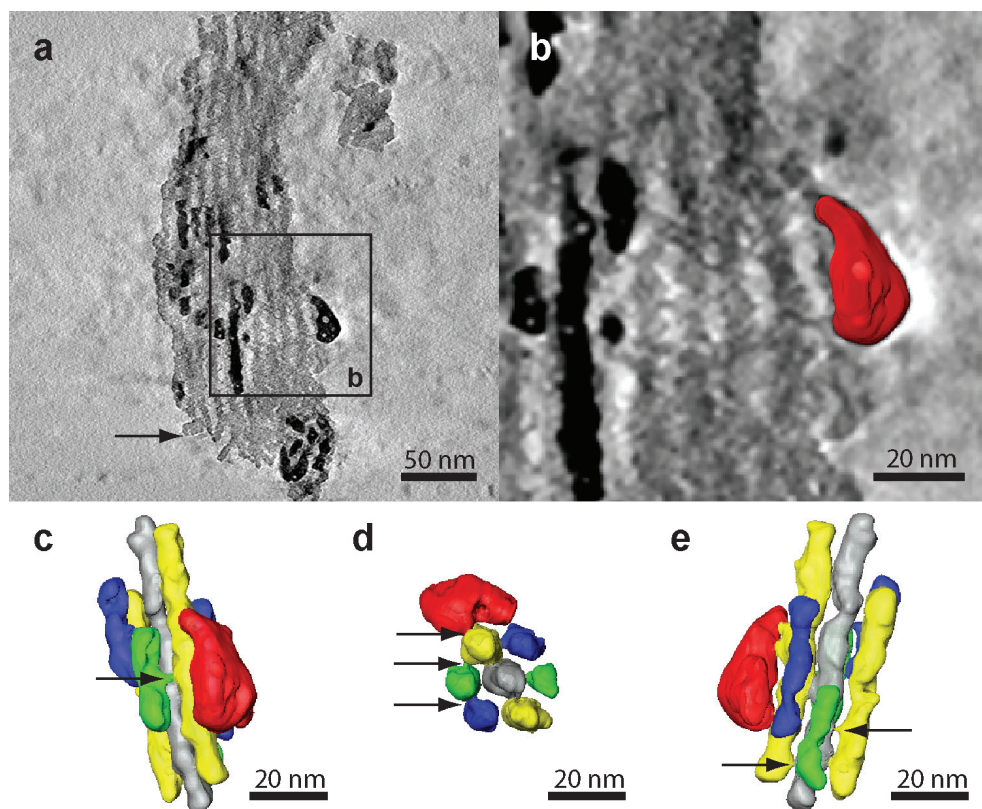


Figure 5 ET slice of S24NiO_{air} showing partially collapsed mesopores indicated by arrow (a), and magnified region with corrugated NiO nanorods and segmented NiO particle (red) on support exterior (b). Surface representation of segmented NiO particles viewed in direction of the electron beam (c), along the SBA-15 pore direction (d), and perpendicular to the SBA-15 pore direction (e). Some bridges connecting the NiO particles through the silica walls are indicated by arrows.

3.3.3 Thermal decomposition in He flow

In Figure 6a,b ET slices through two different SBA-15 particles of sample S24NiO_{He} are displayed. Although to a lesser extent than in the air calcined sample, sintering to rod-like NiO and transport to the support exterior had occurred. The rod diameter (9 nm) was limited by the pore diameter, while the rod length varied from 10-40 nm. For NiO particles on the exterior surface of SBA-15 a diameter of approximately 10-30 nm was found. In addition, thermal decomposition in He flow led to a large number of small, more spherical NiO particles which were retained in the pores of the support. These findings are in line with

the average particle diameter of 8 nm obtained by XRD. Similarly to calcination in air flow, thermal decomposition in a He flow led to cavities and an example is presented in Figure 6c (white arrow). Nitrogen physisorption revealed that only 57% of the mesopores volume was blocked. This fact can be explained by the presence of many small particles which reduces the likelihood of forming cavities. As mentioned above, fragmentation of SBA-15 resulting in partially collapsed SBA-15 mesopores, indicated in Figure 6c,d by black arrows, might also contribute to the blocked mesopore volume.

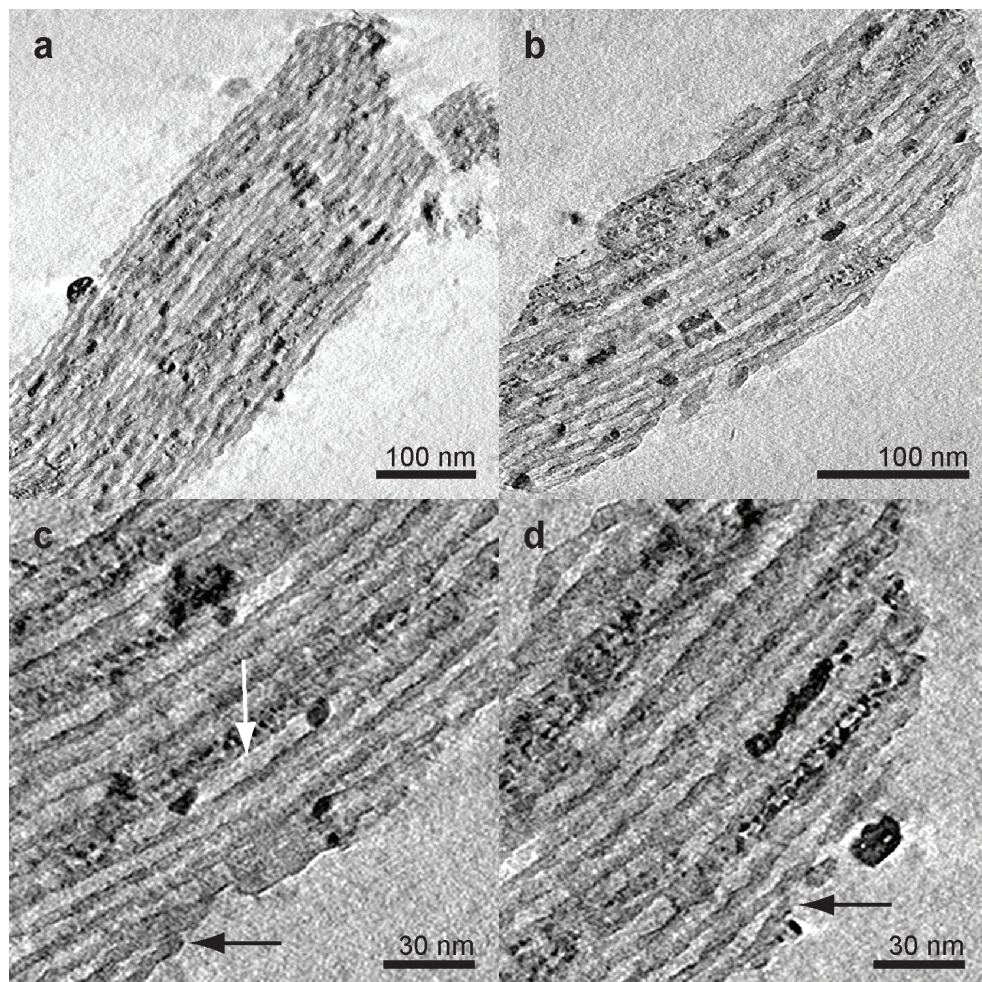


Figure 6 ET slices of sample S24NiO_{He} showing overviews (a,b), a cavity formed between two NiO nanorods indicated by a white arrow (c), and partially collapsed SBA-15 mesopores indicate by black arrows (c,d).

Concluding from the NiO morphology in the two samples presented above, exclusion of O_2 limited the transport of Ni species during thermal decomposition, thereby significantly reducing sintering to rod-like NiO particles and redistribution to the support exterior.

3.3.4 Thermal decomposition in 1 vol% NO in He flow

In Figure 7 two ET slices of sample S24NiO_{NO/He} are displayed. In contrast to thermal decomposition in air or He, no sintering of the nickel phase or transport to the support exterior was observed. NO moderates the thermal decomposition of the basic nickel nitrate and prevents formation of O_2 .³⁹ Limited local concentrations of gaseous decomposition products and suppressed transport of the nickel phase might therefore be responsible for the absence of SBA-15 fragmentation and mesopore collapse. Overall, a non-uniform distribution of NiO within the support material was observed, related to the inhomogeneous distribution of the nitrate precursor after drying (Figure 1). While some SBA-15 mesopores contained a large number of NiO particles, others did not contain any. ET revealed that exclusively small (2-6 nm) NiO particles were formed and retained in the pores of the support. This is in excellent agreement with the average crystallite diameter of 4 nm found by XRD. Since the NiO particles are significantly smaller than the pore diameter of SBA-15 (9 nm) no cavities were formed. The absence of cavities on the scale of individual pores is representative for the bulk material as seen in the N_2 physisorption isotherm in Figure 2. An in depth discussion of the NiO particle size, distribution and resulting NiO loading in individual SBA-15 pores is given in the chapter 4, page 63.⁵⁵

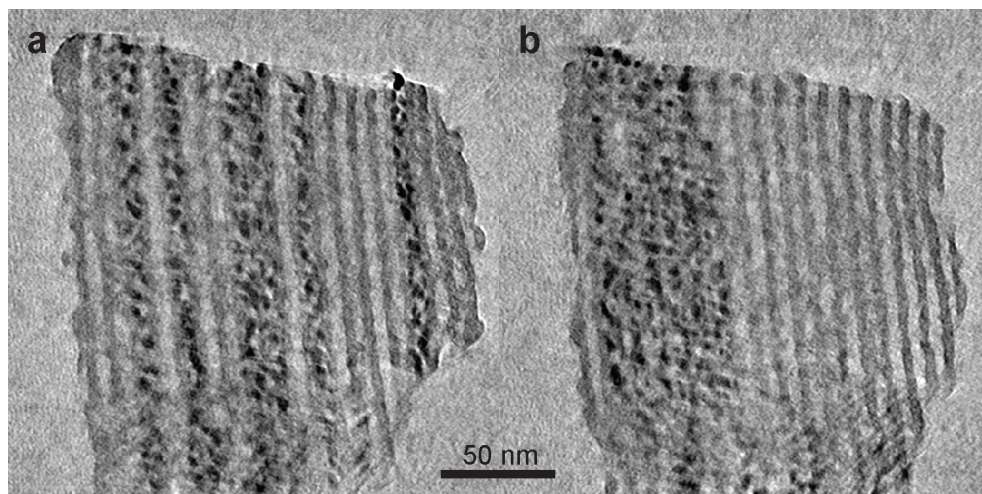


Figure 7 ET slices through reconstruction of sample S24NiO_{NO/He} showing small NiO particles (black) present in only a fraction of the SBA-15 mesopores (dark gray).

3.3.5 Thermal decomposition in stagnant air

As mentioned in section 3.3.1, conversion of the dried precursor in air and under stagnant conditions led to severe sintering and redistribution of the nickel phase (Figure 1). ET results (Figure 8) revealed that the NiO particles on the support exterior were highly porous. Most of these NiO particles exposed a faceted morphology, close to that of an octahedron or part thereof, with sizes of up to several hundreds of nanometers. NiO retained in the SBA-15 mesopores was confined by the pore walls and thus rod-like with a length varying from 20 – 200 nm. The measured Scherrer diameter of more than 25 nm only roughly estimates the NiO particle size on account of their complex morphology, polycrystalline nature, and limitations imposed by the instrumental line broadening. Transport of the nickel phase to the support exterior partially emptied the SBA-15 mesopores which was in line with the N_2 -physisorption results (Figure 2) that revealed only 27 % of blocked mesopore volume despite the severe sintering.

Notably, SBA-15 mesopores adjacent to the exterior NiO particle were preferentially filled by rod-like NiO. Figure 8b illustrates this clearly, in particular the structure to the right, showing the 2D hexagonal ordering of rod-like NiO particles in cross-section (white spots). Deviations from ideal 2D hexagonal symmetry result from sectioning not fully perpendicular to the pore direction. Similarly to decomposition in air flow, NiO particles were interconnected by bridges. The combination of filled pores, connecting bridges and NiO at the support exterior indicated that the transport of the nickel phase most likely had proceeded through the micropores of the silica walls.

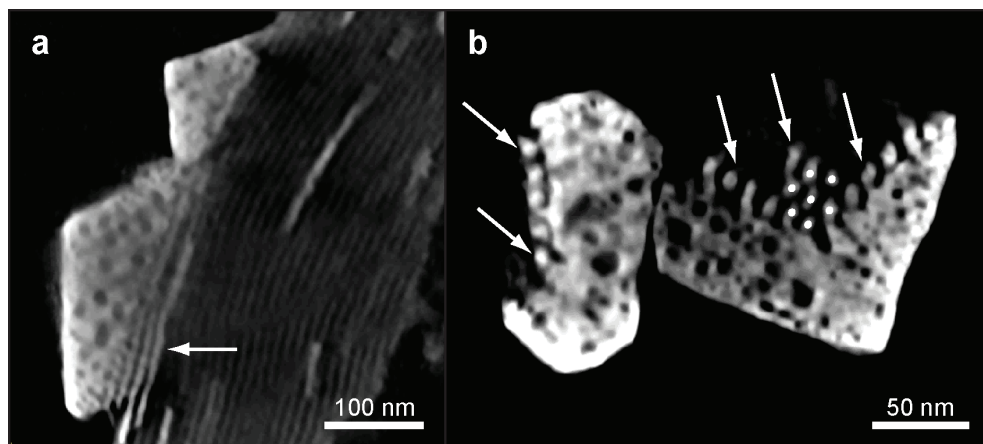


Figure 8 ET slices through HAADF STEM reconstructions of sample S24NiO_{stagnant} showing NiO in bright gray and silica support in dark gray (a), and two different NiO particles in bright gray which were separated from the silica support during TEM sample preparation (b). Some rod-like NiO particles, filling SBA-15 mesopores adjacent to the NiO on the support exterior, are indicated by white arrows and white spots.

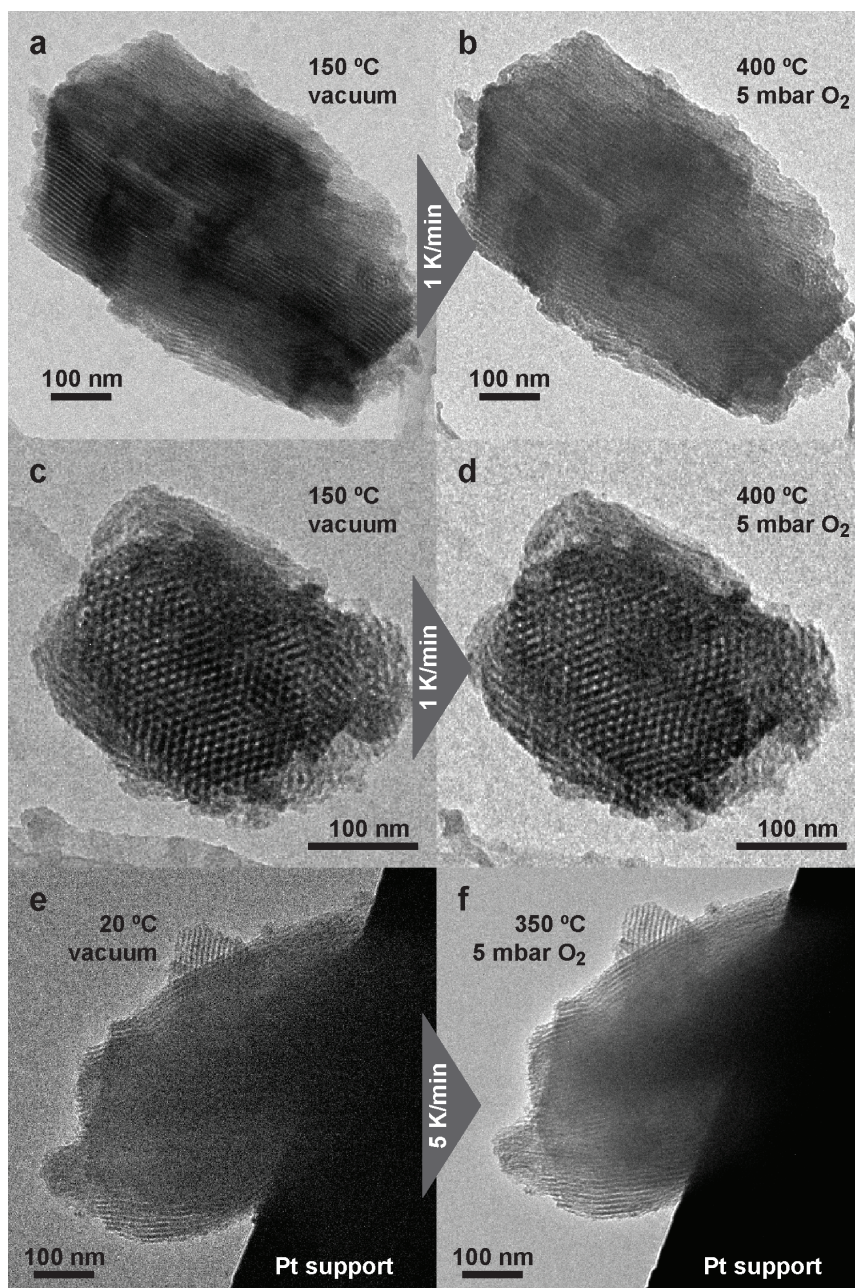


Figure 9 TEM images of basic nickel nitrate/SBA-15 below (a,c,e) and above (b,d,e) the decomposition temperature of the basic nickel nitrate (~ 250 °C). SBA-15 particles were applied either to a carbon support film on a Ti grid (a-d) or a Pt wire mesh without carbon support (e,f).

To study the transport of Ni species in real time, experiments by environmental TEM were carried out and the results are displayed in Figure 9. Although a number of TEM supports (C film and Pt mesh), heating rates (1 and 5 K.min⁻¹), end temperatures (300 to 400 °C), and oxygen partial pressures (5 and 50 mbar) were used, no transport was observed. The morphology of the imaged material containing the nickel phase was remarkably similar below and above the decomposition temperature of the basic nickel nitrate. Therefore, limitations in applicable oxygen pressure (50 mbar) of the environmental setup or insufficient concentrations of decomposition products seemed to prevent in-situ observations. An alternative explanation involves electron beam induced decomposition of the nickel nitrate prior to thermal decomposition.

The formation of crystalline and porous NiO particles on the SBA-15 exterior (Figure 8) is a particularly interesting feature of sample S19NiO_{stagnant}. An illustration of the complex NiO particle morphology is presented in Figure 10a. As mentioned before, most of these NiO structures exposed a faceted morphology close to that of an octahedron or part thereof. The large number of pores suggested that a high surface to volume ratio was reached. We refer to NiO pore in the sense that no NiO is present while pores might be filled with silica. Quantitative analysis of three NiO particles on the SBA-15 exterior estimated the specific NiO surface area of such structures to 25 – 40 m².g⁻¹. More details on the quantification method are presented in chapter 5. Only a small fraction of the NiO pores were cavities, i.e. fully enclosed within the NiO particles. The surface area of these cavities accounted for less than 10 % of the total surface area of the NiO particles. Figure 10b displays the cavity size distribution that could be approximated by a lognormal distribution, also found for the void (bubble) size distributions in liquids⁵⁶ and metals.⁵⁷ Such information, not accessible to other techniques such as N₂-physisorption, might contribute to an understanding of the nature and attendant phases of mass transport.

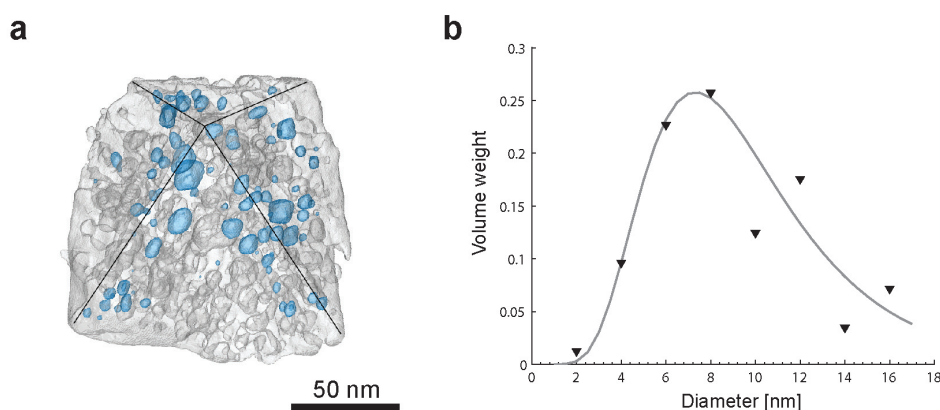


Figure 10 Surface representation of a porous NiO particle with edges of facets indicated by lines and showing cavities in blue through the semi-transparent exterior surface (a). Size distribution of 296 cavities found in three NiO particles with lognormal fit (b).

3.4 Conclusions

The 3D morphology of SBA-15 supported NiO obtained by thermal decomposition of nickel nitrate in air, He, and NO/He was studied. The combination of ET, N₂-physisorption and XRD permitted detailed insight into the NiO particle size and distribution down to the level of individual SBA-15 mesopores as a function of the gas atmosphere. While thermal decomposition in air led exclusively to rod-like NiO particles inside the mesopores, in He a large number of smaller more spherical particles was present too. Rod-like NiO particles, confined by the corrugated silica walls, led to cavities between particles within the same pore. This finding provided a microscopic explanation for the forced closure of the hysteresis loop in the N₂-physisorption isotherms. Thermal treatment in NO/He moderated the decomposition rate, forming exclusively small particles inside the mesopores of the support. Besides intra-porous rod-like particles, NiO was present on the exterior surface of SBA-15 after decomposition in air and He. Redistribution phenomena were most severe for stagnant air, much less pronounced in air flow, and almost absent in He flow. Synonymously, exclusion of O₂ limited precursor mobility, while retarded removal of decomposition products significantly enhanced redistribution. NiO particles on the support exterior were in most instances porous and connected by bridges through the micropores of the silica wall to NiO filling adjacent mesopores. A quantitative analysis estimated the specific NiO surface area to 25 – 40 m².g⁻¹ for external particles obtained by decomposition in stagnant air. The application of ET in combination with bulk characterization techniques gives detailed insight into the processes that govern the assembly of heterogeneous catalysts.

Acknowledgements

Jelle R. A. Sietsma is kindly thanked for introducing me to the field of model catalysts and for preparation of the supported NiO/SBA-15 samples, N₂ physisorption and XRD characterization. I also would like to acknowledge Mariska Wolters and Tamara Eggenhuisen for an engaging collaboration on catalyst preparation. A special thanks to Peter Crozier for the environmental TEM experiments at Arizona State University. Microscopy was performed at the Electron Microscopy group Utrecht (EMU) acknowledging W. J. C. Geerts, J. D. Meeldijk, T. P. van der Krift, M. N. Lebbink, N. Jimenez-Gil, A. Yakushevska, and M. Barcena for their support.

References

- (1) Bell, A. T. *Science* **2003**, *299*, 1688.
- (2) de Jong, K. P. *Curr. Opin. Solid State Mater. Sci.* **1999**, *4*, 55.
- (3) Schlögl, R.; Abd Hamid, S. B. *Angew. Chem. Int. Ed.* **2004**, *43*, 1628.
- (4) Allen, R. R. *J. Am. Oil Chem. Soc.* **1986**, *63*, 1328.
- (5) Balakos, M. W.; Hernandez, E. E. *Catal. Today* **1997**, *35*, 415.

- (6) Fouillaux, P. *Appl. Catal.* **1983**, *8*, 1.
- (7) Carrier, X.; Lambert, J. F.; Che, M. *J. Am. Chem. Soc.* **1997**, *119*, 10137.
- (8) Schreier, M.; Regalbutto, J. R. *J. Catal.* **2004**, *225*, 190.
- (9) Toebes, M. L.; van der Lee, M. K.; Tang, L. M.; in 't Veld, M. H. H.; Bitter, J. H.; van Dillen, A. J.; de Jong, K. P. *J. Phys. Chem. B* **2004**, *108*, 11611.
- (10) Boellaard, E.; van der Kraan, A. M.; Geus, J. W. *Stud. Surf. Sci. Catal.* **1995**, *91*, 931.
- (11) van der Grift, C. J. G.; Elberse, P. A.; Mulder, A.; Geus, J. W. *Appl. Catal.* **1990**, *59*, 275.
- (12) van der Lee, M. K.; van Dillen, J.; Bitter, J. H.; de Jong, K. P. *J. Am. Chem. Soc.* **2005**, *127*, 13573.
- (13) Bourikas, K.; Kordulis, C.; Lycourghiotis, A. *Catal. Rev. Sci. Eng.* **2006**, *48*, 363.
- (14) Haddad, G. J.; Goodwin, J. G. *J. Catal.* **1995**, *157*, 25.
- (15) Thomas, J. M.; Raja, R.; Johnson, B. F. G.; Hermans, S.; Jones, M. D.; Khimyak, T. *Ind. Eng. Chem. Res.* **2003**, *42*, 1563.
- (16) Ertl, G.; Knözinger, H.; Weikamp, J.; (Ed.) *Preparation of Solid Catalysts*; WILEY-VCH Verlag GmbH: Weinheim, 1999.
- (17) Wang, X. Y.; Zhao, B. Y.; Jiang, D. E.; Xie, Y. C. *Appl. Catal., A* **1999**, *188*, 201.
- (18) Infantes-Molina, A.; Merida-Robles, J.; Braos-Garcia, P.; Rodriguez-Castellon, E.; Finocchio, E.; Busca, G.; Maireles-Torres, P.; Jimenez-Lopez, A. *J. Catal.* **2004**, *225*, 479.
- (19) Okamoto, Y.; Nagata, K.; Adachi, T.; Imanaka, T.; Inamura, K.; Takyu, T. *J. Phys. Chem.* **1991**, *95*, 310.
- (20) van de Loosdrecht, J.; Barradas, S.; Caricato, E. A.; Ngwenya, N. G.; Nkwanyana, P. S.; Rawat, M. A. S.; Sigwebela, B. H.; van Berge, P. J.; Visagie, J. L. *Topics Catal.* **2003**, *26*, 121.
- (21) Vos, B.; Poels, E.; Blik, A. *J. Catal.* **2001**, *198*, 77.
- (22) van Dillen, A. J.; Terorde, R. J. A. M.; Lensveld, D. J.; Geus, J. W.; de Jong, K. P. *J. Catal.* **2003**, *216*, 257.
- (23) Lensveld, D. J.; Mesu, J. G.; van Dillen, A. J.; de Jong, K. P. *Microporous Mesoporous Mater.* **2001**, *44*, 401.
- (24) Sietsma, J. R. A.; Van Dillen, A. J.; de Jongh, P. E.; de Jong, K. P. *Stud. Surf. Sci. Catal.* **2006**, *162*, 95.
- (25) Kresge, C. T.; Leonowicz, M. E.; Roth, W. J.; Vartuli, J. C.; Beck, J. S. *Nature* **1992**, *359*, 710.
- (26) Zhao, D. Y.; Feng, J. L.; Huo, Q. S.; Melosh, N.; Fredrickson, G. H.; Chmelka, B. F.; Stucky, G. D. *Science* **1998**, *279*, 548.
- (27) de Jong, K. P. *Oil & Gas Sci. Technol.* **2006**, *61*, 527.
- (28) Sietsma, J. R. A. PhD thesis, Department of Chemistry, Utrecht University, 2007.
- (29) Khodakov, A. Y.; Zholobenko, V. L.; Bechara, R.; Durand, D. *Microporous Mesoporous Mater.* **2005**, *79*, 29.
- (30) Vradman, L.; Landau, M. V.; Kantorovich, D.; Kolytyn, Y.; Gedanken, A. *Microporous Mesoporous Mater.* **2005**, *79*, 307.
- (31) Li, X. K.; Ji, W. J.; Zhao, J.; Wang, S. J.; Au, C. T. *J. Catal.* **2005**, *236*, 181.
- (32) Imperor-Clerc, M.; Bazin, D.; Appay, M. D.; Beaudier, P.; Davidson, A. *Chem. Mater.* **2004**, *16*, 1813.
- (33) Janssen, A. H.; Yang, C. M.; Wang, Y.; Schüth, F.; Koster, A. J.; de Jong, K. P. *J. Phys. Chem. B* **2003**, *107*, 10552.
- (34) Moreno, M. S.; Weyland, M.; Midgley, P. A.; Bengoa, J. F.; Cagnoli, M. V.; Gallegos, N. G.; Alvarez, A. M.; Marchetti, S. G. *Micron* **2006**, *37*, 52.
- (35) Jentys, A.; Kleestorfer, K.; Vinek, H. *Microporous Mesoporous Mater.* **1999**, *27*, 321.
- (36) Llewellyn, P. L.; Schüth, F.; Grillet, Y.; Rouquerol, F.; Rouquerol, J.; Unger, K. K. *Langmuir* **1995**, *11*, 574.

- (37) Zhuravlev, L. T. *Langmuir* **1987**, *3*, 316.
- (38) Sietsma, J. R. A.; Meeldijk, J. D.; Versluijs-Helder, M.; Broersma, A.; van Dillen, A. J.; de Jongh, P. E.; de Jong, K. P. *Chem. Mater.* **2008**, *20*, 2921.
- (39) Sietsma, J. R. A.; Friedrich, H.; Broersma, A.; Versluijs-Helder, M.; Van Dillen, A. J.; De Jongh, P. E.; De Jong, K. P. *J. Catal* **2008**, *260*, 227.
- (40) Sietsma, J. R. A.; Meeldijk, J. D.; den Breejen, J. P.; Versluijs-Helder, M.; van Dillen, A. J.; de Jongh, P. E.; de Jong, K. P. *Angew. Chem.-Int. Ed.* **2007**, *46*, 4547.
- (41) Chytil, S.; Haugland, L.; Blekkan, E. A. *Microporous Mesoporous Mater.* **2008**, *111*, 134.
- (42) Jaroniec, M.; Kruk, M.; Olivier, J. P.; Koch, S. *Stud. Surf. Sci. Catal.* **2000**, *128*, 71.
- (43) Barrett, E. P.; Joyner, L. G.; Halenda, P. P. *J. Am. Chem. Soc.* **1951**, *73*, 373.
- (44) Harkins, W. D.; Jura, G. *J. Am. Chem. Soc.* **1944**, *66*, 1366.
- (45) Kruk, M.; Jaroniec, M.; Sayari, A. *Langmuir* **1997**, *13*, 6267.
- (46) Kremer, J. R.; Mastronarde, D. N.; McIntosh, J. R. *J. Struct. Biol.* **1996**, *116*, 71.
- (47) Frangakis, A. S.; Hegerl, R. *J. Struct. Biol.* **2001**, *135*, 239.
- (48) Nickell, S.; Forster, F.; Linaroudis, A.; Net, W. D.; Beck, F.; Hegerl, R.; Baumeister, W.; Plitzko, J. M. *J. Struct. Biol.* **2005**, *149*, 227.
- (49) van der Voort, P.; Ravikovitch, P. I.; de Jong, K. P.; Neimark, A. V.; Janssen, A. H.; Benjelloun, M.; van Bavel, E.; Cool, P.; Weckhuysen, B. M.; Vansant, E. F. *Chem. Commun.* **2002**, 1010.
- (50) Ravikovitch, P. I.; Neimark, A. V. *Langmuir* **2002**, *18*, 9830.
- (51) Gommès, C.; Friedrich, H.; Wolters, M.; de Jongh, P. E.; de Jong, K. P. *Chem. Mater.* **2009**, *21*, 1311.
- (52) Liu, Z.; Terasaki, O.; Ohsuna, T.; Hiraga, K.; Shin, H. J.; Ryoo, R. *Chemphyschem* **2001**, *2*, 229.
- (53) Salabas, E. L.; Rumpelcker, A.; Kleitz, F.; Radu, F.; Schüth, F. *Nano Lett.* **2006**, *6*, 2977.
- (54) Tian, B. Z.; Liu, X. Y.; Yang, H. F.; Xie, S. H.; Yu, C. Z.; Tu, B.; Zhao, D. Y. *Adv. Mater.* **2003**, *15*, 1370.
- (55) Friedrich, H.; Sietsma, J. R. A.; de Jongh, P. E.; Verkleij, A. J.; de Jong, K. P. *J. Am. Chem. Soc.* **2007**, *129*, 10249.
- (56) Du, L. P.; Prokop, A.; Tanner, R. D. *J. Colloid Interface Sci.* **2003**, *259*, 180.
- (57) Suzudo, T.; Kaburaki, H.; Itakura, M.; Wakai, E. *Modell. Simul. Mater. Sci. Eng.* **2008**, *16*, 055003.

Chapter 4

Measuring Location, Size, Distribution, and Loading of NiO Crystallites in individual SBA-15 Pores by Electron Tomography

Abstract

By combining electron tomography with image segmentation the properties of 299 NiO crystallites contained in six SBA-15 pores were studied. A statistical analysis of the particle size showed that crystallites between 2 and 6 nm were present with a distribution maximum at 3 nm and 4 nm, for the number-weighted and volume-weighted curves, respectively. Inter-particle distances between nearest neighbors were 1 to 3 nm with very few isolated crystallites. In the examined pores a local loading twice the applied average of 24 wt% NiO was found. This suggests that a very high local loading combined with a high dispersion is achievable.

Adapted with permission from H. Friedrich, J. R. A. Sietsma, P.E. de Jongh, A. J. Verkleij, and K. P. de Jong, *Measuring Location, Size, Distribution, and Loading of NiO Crystallites in individual SBA-15 Pores by Electron Tomography*. J. Am. Chem. Soc. **2007**, *129*, 10249-10254. Copyright 2007 American Chemical Society.

4.1 Introduction

The intermediate size regime of nanostructured materials, where the collective behavior of bulk materials emerges from the discrete nature of molecular properties, provides the opportunity to observe unusual optical¹, magnetic², and catalytic³ behavior. One important factor for the design and production of such novel materials, in general, and more efficient catalysts, in particular, is the development of new characterization procedures. In heterogeneous catalysis, size, structure, location, distribution, and accessibility of the active particles within the support determine the selectivity and activity of the catalyst. Since commercial catalysts are highly complex, fundamental studies are advantageously carried out on well-defined model systems. In this respect ordered mesoporous materials (OMM) have attracted much attention as model supports since 1992.^{4,5} This special interest can be attributed to their tunable and well-defined pore geometry, bridging the gap between ordered microporous zeolites and disordered meso- and macroporous oxides. One of the most widely studied ordered mesoporous silica is SBA-15, exposing a two-dimensional hexagonal symmetry of cylindrical pores.⁶ Its thermostability and the extensive prior research⁷⁻¹⁹ make catalysts prepared from SBA-15 ideal model systems. For the present case study a highly dispersed NiO/SBA-15 intermediate was chosen, since nickel is used as active component in many industrially relevant processes.²⁰⁻²³

Structural characterization of OMM-based catalysts to study the influence of various preparation treatments is mostly carried out by bulk techniques, such as N₂-physisorption¹⁰⁻¹⁹ or X-ray diffraction¹²⁻¹⁹ (XRD). From these measurements structural parameters, like pore diameter, pore wall thickness, particle size, and accessibility of the active phase are derived. One major drawback of bulk techniques is that no direct information on the actual location and distribution of the active particles within the support is obtained. If additional, spatially resolved information is required, transmission electron microscopy (TEM)^{14-19,24-27} and scanning electron microscopy (SEM)²⁵⁻²⁹ are applied. Although TEM is a very powerful technique, the resulting images are in first approximation a two-dimensional (2D) projection of a three-dimensional (3D) structure.³⁰ This implies that for complex 3D objects, like the examined NiO/SBA-15, the 3D location and distribution of the NiO phase cannot be unambiguously determined from a TEM image.

Complex 3D structures can be imaged using electron tomography (ET), sometimes referred to as 3D-TEM, which combines multiple TEM images from different directions.^{7-9,24-27,31-35} First applications of ET to heterogeneous catalysts focused on the qualitative description of the observed nanoscale structures.⁷⁻⁹ More recent applications involve a posteriori image segmentation to quantify catalyst properties, like, porosity,³³ localization of the active phase,³⁴ and loading of active components.³⁵ As for any data derived from electron microscopy, care has to be taken that the imaged structures are representative for the bulk, thus bulk characterization is mandatory to provide a basis to evaluate the relevance of nanoscale

observations. In the present study ET in combination with a posteriori image segmentation is applied to measure the 3D location and size of single NiO crystallites in individual SBA-15 pores. Based on the segmentation results the NiO particle size distribution, 3D nearest neighbor distances, and a loading model of individual SBA-15 pores are derived. Obtained results are verified and discussed in context of the bulk characterization. To our knowledge, this is the first application of ET to quantify the particle size distribution, 3D nearest neighbor distances, and the local loading in individual pores of the support material.

4.2 Materials and Methods

Preparation of NiO/SBA-15. SBA-15 (pore volume $0.73 \text{ cm}^3 \cdot \text{g}^{-1}$) was synthesized according to a procedure described by Zhao.⁶ Deposition of the NiO precursor was carried out by incipient wetness impregnation of SBA-15 using a 4.2 M aqueous $\text{Ni}(\text{NO}_3)_2$ solution ($\text{Ni}(\text{NO}_3)_2 \cdot 6\text{H}_2\text{O}$ (Acros) in demineralized water) followed by drying at $120 \text{ }^\circ\text{C}$ for 12 hours. Conversion of the dried precursor was done by heating the sample at $1 \text{ }^\circ\text{C} \cdot \text{min}^{-1}$ to $450 \text{ }^\circ\text{C}$ in a flow of 1 vol% NO in He. The sample was kept at $450 \text{ }^\circ\text{C}$ for 4 hours. Following this procedure highly dispersed NiO/SBA-15 at a loading of 24 wt% NiO was obtained.³⁶

XRD and N_2 -physisorption. Powder XRD measurements were performed with a Bruker AXS D8 Advance diffractometer using $\text{Co K}\alpha_{1,2}$ radiation with a wavelength of 0.179 nm. Small-angle XRD patterns of the SBA-15 material were recorded from 0.5 to 5 degrees (2θ) at an angular increment of 0.0086 degrees. The diffraction pattern was corrected for the $\text{K}\alpha_2$ component prior to further processing. To provide reproducible results and minimize effects of XRD sample preparation, the average over eight individual small angle XRD patterns was taken. XRD measurements of the NiO/SBA-15 were obtained from 40 to 100 degrees (2θ) at an angular increment of 0.0086 degrees. The NiO crystallite size was calculated from the FWHM of the broadened diffraction peaks using the Scherrer equation.

N_2 -physisorption measurements were performed at $-196 \text{ }^\circ\text{C}$ (Micromeritics, TriStar 3000 V6.01 A) on the SBA-15 and the NiO/SBA-15 intermediate. From the adsorption isotherms the pore volume and pore size distribution were deduced using NL-DFT theory³⁷⁻³⁹ implemented in the DataMaster 4.01 software (Micromeritics).

Electron tomography (ET). TEM tomography grids were prepared by applying 10 nm sized colloidal gold particles (Aurion, PAG conjugated) from aqueous suspension to a Quantifoil R2/1 carbon film supported on a parallel bar Cu TEM grid. After drying in air, a small amount of the NiO/SBA-15 powder was deposited directly onto the grid. Excess catalyst was shook-off before inserting the TEM grid into a Fischione, Model 2020, advanced tomography holder. ET was performed in bright-field TEM mode using a Tecnai 20 electron microscope (FEI) operating at 200kV acceleration voltage, equipped with a LaB_6 electron source and a TWIN objective lens. A series of TEM images (tilt-series) were acquired by rotating the specimen inside the microscope over a tilt range of at least $+70$ to -70 degrees

at increments of 1 degree. Images were recorded at each tilt step on a 2048 pixel \times 2048 pixel TVIPS CCD camera using Xplore3D software (FEI). Diffraction effects caused by a combination of the microscope aberrations and strongly excited high-order beams, resulting in non-symmetric white halos around crystalline material, were excluded by using an objective aperture. The defocus was set between -130 nm and -200 nm depending on the thickness of the examined SBA-15 particle to keep the entire object in underfocus. The nominal magnification was 29000 \times which corresponds to a pixel size of 0.27 nm. Images of the tilt-series were aligned with respect to a common origin and rotation axis using the 10 nm gold particles as fiducial markers. Finally the aligned tilt-series was binned to 0.54 nm pixel size prior to reconstruction of the three-dimensional volume. Alignment and reconstruction by filtered backprojection was performed in IMOD.⁴⁰ Preliminary results using the sequential iterative reconstruction technique (SIRT) showed good contrast in the reconstruction, but did not improve the segmentation described in the next paragraph.

Image analysis. Assessment of the NiO phase within the SBA-15 mesopores, a process called segmentation, was carried out in Amira 3.1 (TGS - Visual Concepts / Mercury Computer Systems, Inc.). Segmentation involved in a first step the manual tracing of the NiO crystallite contours throughout the volume of the examined mesopores. Since the NiO crystallites are three-dimensional, three perpendicular cutting planes were used to identify connected regions with dark contrast. As practical limit for the smallest detectable particle a connected region of at least $3 \times 3 \times 2$ pixels ($\sim 3 \text{ nm}^3$) had to be present. This practical limit exceeds the rule-of-thumb for the theoretically predicted resolution which equals three times the thickness of the sample divided by the number of images. However, the practical achievable resolution has been reported to be considerably better than the calculated value.^{9,31} In the last segmentation step the volume and the center-of-mass of each NiO crystallite was calculated.

4.3 Results and Discussion

4.3.1 Bulk characterization

A schematic model of the SBA-15 support is shown in Figure 1a. The straight cylindrical pores are viewed along the pore direction and the 2D hexagonal symmetry (p6mm) of the pore ordering is apparent. The small-angle XRD pattern of the SBA-15 (Figure 1b) shows distinct peaks that are associated with the hexagonal symmetry.⁶ From the position of the first three peaks the unit cell size (a_0) was calculated to $10.5 \pm 0.2 \text{ nm}$.

The corresponding SBA-15 adsorption and desorption isotherms with their typical hysteresis loop are displayed in Figure 2a. Analysis by NL-DFT calculations³⁷⁻³⁹ gave a porosity of $0.73 \text{ cm}^3 \cdot \text{g}^{-1}$ and a very narrow pore size distribution with a maximum at 9 nm (Figure 2b). These results confirm a uniform SBA-15 support with 1 to 2 nm thick pore walls.

Upon addition of the NiO phase to the SBA-15 support by impregnation, drying, and calcination, the accessible pore volume decreased (Figure 2a). The desorption branch of the isotherm did not indicate a significant mesopore blocking.^{8,11} NL-DFT analysis yielded a porosity of $0.54 \text{ cm}^3 \cdot \text{g}^{-1}$ and a pore size distribution similar to the one observed for the blank SBA-15 with the maximum again at 9 nm (Figure 2b). The XRD pattern of NiO/SBA-15 (Figure 3) displays three distinct peaks associated with the NiO crystal structure. The width of the diffraction peaks confirmed that only nanometer-sized NiO crystallites were created upon calcination of the precursor. All three peaks had a FWHM that led via the Scherrer equation to a NiO crystallite size of 4 nm. The formation of small NiO crystallites in combination with the observed loss in pore volume suggests that the NiO phase was located inside the SBA-15 pores.

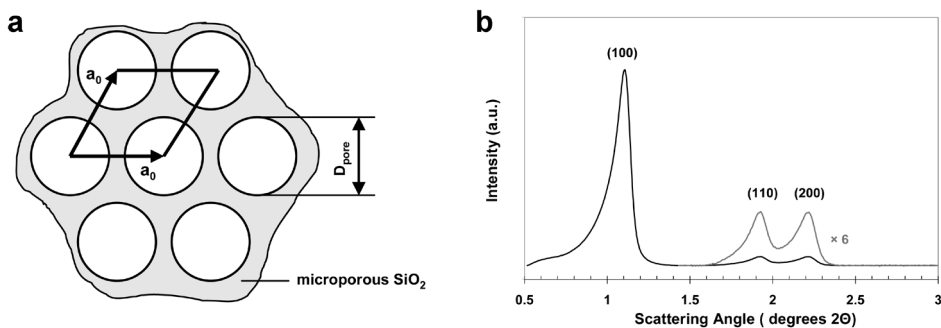


Figure 1. Geometrical model of the hexagonal mesopore ordering in SBA-15 (a), and low angle XRD pattern (b).

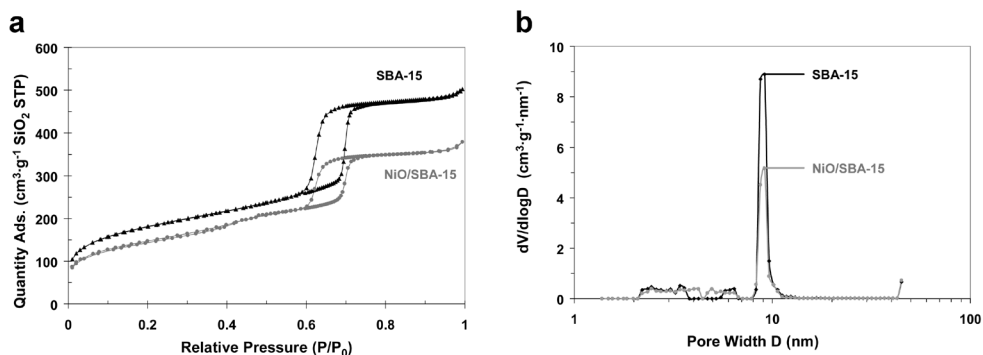


Figure 2. N₂ adsorption and desorption isotherms of SBA-15 and NiO/SBA-15 (a), and pore size distributions derived by NL-DFT (b).

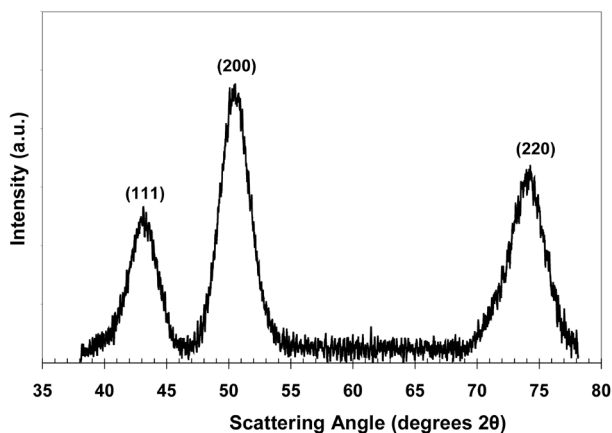


Figure 3. XRD pattern of the NiO crystallites within SBA-15 after impregnation and calcination.

4.3.2 Characterization by ET

TEM observations, as in Figure 4a, confirm that the NiO phase was assembled inside the SBA-15 pores. Using ET the actual 3D structure is resolved. Figure 4b shows a 0.54 nm thick numerical cross-section through the reconstruction of the support particle A. It is immediately apparent that not all pores of the support contained NiO crystallites. In this particular structure approximately 45% of the pores were filled. This phenomenon, of filling only a fraction of the pores, has previously been reported for $\text{ZrO}_2/\text{SBA-15}$ ⁸ and $\text{MnO}_x/\text{SBA-15}$ ⁴¹, and might be related to an inhomogeneous concentration of surface hydroxyl groups.^{42,43} The extent of pore filling by NiO throughout the whole SBA-15 structure can be best observed by consulting the supporting movie slices.mpg.

For a quantitative characterization image segmentation was applied. In Figure 4c a part of the numerical cross-section has been magnified. The manually traced contours of the NiO are marked in different colors. Crystallites belonging to different pores have been color coded green, blue, yellow, pink, and red. A 3D surface model of the NiO is displayed in Figure 4d. This example shows how ET in combination with a posteriori image processing provides the volume and the 3D location of the NiO crystallites in individual SBA-15 pores. For further analysis a total of 299 NiO crystallites, contained in six filled pores (3 in support particles A and B), were segmented. The six filled pores were chosen from different regions of the two SBA-15 structures to ensure proper statistical sampling. The relative location of the three pores in support particle A is indicated in the supporting movie slices.mpg.

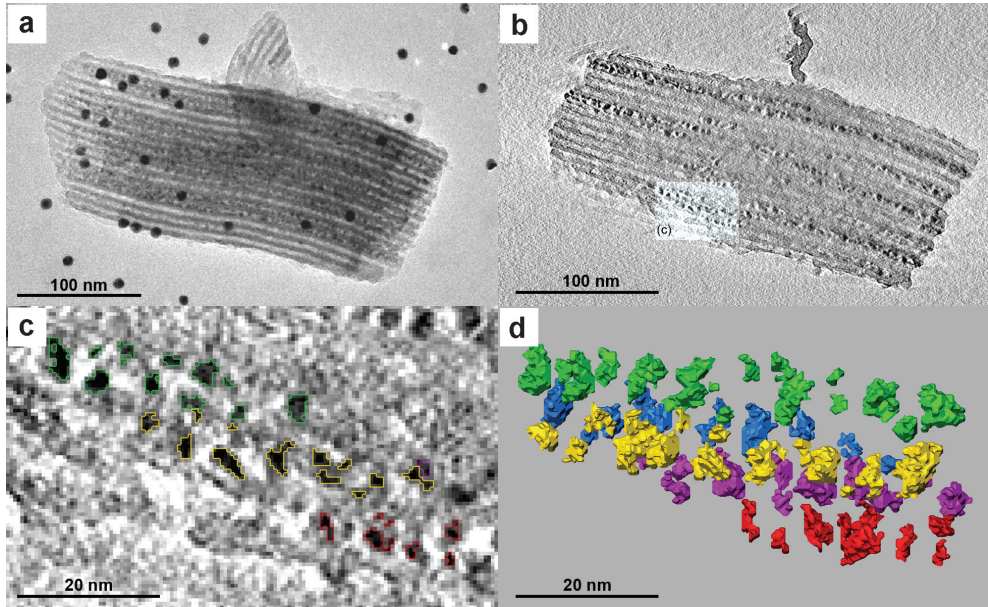


Figure 4. TEM image of NiO/SBA-15 structure (particle A). The dark spots are 10 nm gold particles used for alignment of the tilt series (a). 0.54 nm thick numerical cross-section through same object (b), magnified part of cross-section with colored outline of segmented NiO crystals. Different colors have been assigned to crystals in different pores (c). surface view of segmented NiO particles (d).

For accurate volume measurements reconstruction artifacts have to be considered. Dense objects will appear elongated in the tomographic reconstruction, an effect which is known as the missing wedge problem.⁴⁴⁻⁴⁶ The missing wedge of information in Fourier space is caused by the inherent limit to the range of tilt angles, e.g. the finite thickness of the specimen holder and restrictions of the microscope stage.⁴⁴⁻⁴⁶ The elongation factor, e , which occurs in the direction of the electron beam, can be calculated from the maximum tilt angle (α):⁴⁷

$$e = \sqrt{\frac{\alpha + \sin \alpha \cos \alpha}{\alpha - \sin \alpha \cos \alpha}} \quad (1)$$

Measured volumes of the NiO crystals have to be corrected for elongation by dividing by the elongation factor. Simple division can be applied, since elongation only occurs along one axis of the three-dimensional structure.

A statistical analysis of the 299 NiO crystallite volumes (Figure 5a) showed that a large number of small NiO crystallites ($< 30 \text{ nm}^3$) were present. The measured volumes are, in contrast to those resulting from techniques like TEM or XRD, not based on a sphere model. The volume statistics could be fitted well to a log-normal distribution as predicted by Granqvist to be observed independently of the prevalent growth mechanism.^{48,49}

For comparison with XRD, the size of each NiO crystallite can be estimated by its equivalent diameter, i.e. the diameter of a sphere having the same volume. The resulting size distribution and log-normal fit are given in Figure 5b. Despite the fact that the crystallites did not appear to be spherical, a close match is observed. When volume weighting was applied to the log-normal fit, the curve maximum shifted from 3 nm to 4 nm, which corresponds very well with the NiO crystallite diameter obtained by XRD. The deviation at a diameter value of 5 nm was caused by poor statistical sampling as seen in the region between 60 and 80 nm^3 in Figure 5a. The observation that particles of 6 nm and above were rare was also supported by the N_2 - physisorption measurements and the inferred absence of mesopore blocking.

In addition to the volume, the locations of all 299 NiO crystallites were determined from their centers-of-mass. The results of a statistical analysis of the nearest and second-nearest neighbor distances between NiO crystallites can be seen in Figure 6. Distances were measured in 3D between the centers-of-mass of adjacent NiO crystallites belonging to the same pore. Both curves are narrow indicating a homogeneous distribution and very few isolated crystallites. In conjunction with the measured particle size distribution, neighbors were separated by only 1-3 nm. To our knowledge, no other technique can provide this local nanoscale information.

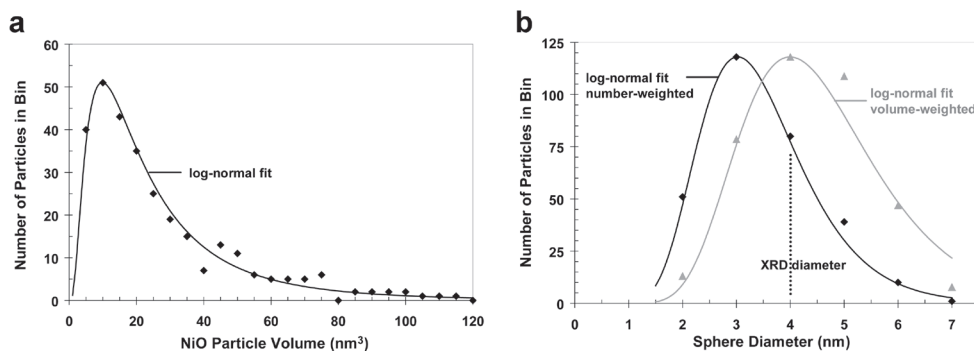


Figure 5. Volume statistics over 299 NiO particles (a), and size distributions of NiO particles expressed in diameter of sphere having the same volume (b).

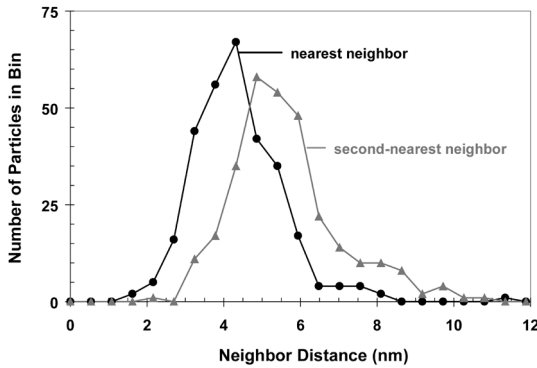


Figure 6. Statistical analysis of the 3D nearest and 3D second-nearest neighbor distances from 299 NiO crystallites.

4.3.3 A nanoscale loading model

The loading of an individual SBA-15 pore can be calculated if the NiO and the SiO₂ volumes associated with that particular pore are known. The NiO volume per filled pore equals the sum over the individual crystallite volumes, while the SiO₂ volume can be calculated from a geometrical model:

$$V_{SiO_2} = \frac{\frac{\sqrt{3}}{2} a_0^2}{1 + \rho_{SiO_2} (V_{pores} + V_{NiO})} \cdot L_{pore} \quad (2)$$

with ($a_0 = 10.5 \text{ nm}$) the unit cell size, ($\rho_{SiO_2} = 2.2 \text{ g}\cdot\text{cm}^{-3}$) the density of bulk silica, ($V_{pores} = 0.54 \text{ cm}^3\cdot\text{g}^{-1}$) the pore volume measured by N₂-physisorption, ($V_{NiO} = 0.047 \text{ cm}^3\cdot\text{g}^{-1}$) the volume of impregnated NiO per gram of silica, and (L_{pore} in nm) the pore length. The pore length is approximated by the center-of-mass-distance between the first and the last segmented particle in the pore.

Detailed values for occupied pore length, segmented NiO volume, calculated SiO₂ volume and the resulting loading in individual pores are given in Table 1. To our surprise a local loading much higher than the applied 24 wt% was found. The loading average of 41 wt% corresponds to a NiO content in the examined pores that is more than twice the expected value. This observation is in line with the large percentage of unfilled pores that arguably compensate for the high local loading.

Table 1. Properties of NiO filled SBA-15 pores from reconstruction A and B.

pore	length [nm]	NiO volume [nm ³]	SiO ₂ volume [nm ³]	NiO loading [wt%]
A1	134	1650	5588	47
A2	211	1998	8799	41
A3	198	1711	8257	39
B1	94	939	3920	42
B2	111	1081	4629	42
B3	139	916	5797	32
all	887	8295	36991	41

Variations along the pores were studied by calculating the loading in 10 consecutive pore segments as displayed for pore A3 in Figure 7. Information on crystallite volume vs. position and a surface view complement the results. In general a homogeneous distribution of the number of NiO particles is seen, leading to few isolated crystallites as derived from the nearest neighbor distances. A preference towards higher loading at the pore mouth was not found. Although small and large particles were mostly distributed at random, the local loading decreased in regions with mainly small particles.

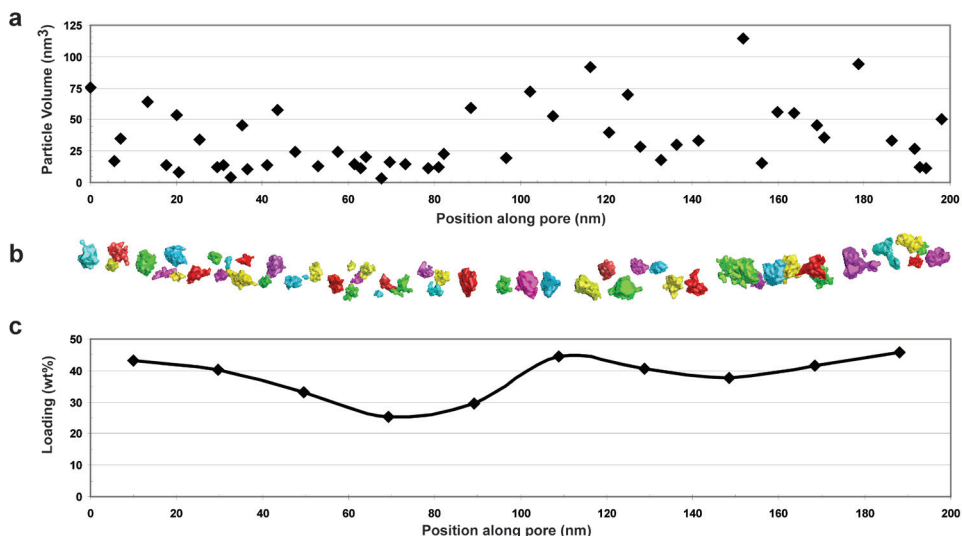


Figure 7. Properties of pore A3 of NiO/SBA-15: position and corresponding volume of individual NiO crystallites (a), surface view of NiO crystallites (b), and local NiO loading calculated for 10 successive segments of the SBA-15 pore (c).

Any conclusions to be drawn from this nanoscale pore loading model have to be seen with regard to its limitations. Limiting factors are the pore length approximation, the segmentation accuracy, and the fact that NiO particles below 3 nm^3 ($\sim 1.8 \text{ nm}$ sphere diameter) have not been detected. A 10 % error in both NiO and SiO₂ volumes translated into 5 wt% difference in local loading. Effects of the reconstruction point-spread function beyond the elongation factor were not considered and might further decrease the segmentation accuracy, and consequently the size determination.

Electron tomograms contain large amounts of potentially quantitative information, but the problem remains of how to extract it. Manual segmentation, although subjective and its error undetermined, is one rather straightforward solution to the problem. Based on a total of 299 examined NiO crystallites a sufficient statistical sampling was given. Volume and particle size distributions corresponded well with numerical fits of a commonly assumed log-normal distribution.⁴⁹ The close match of the ET derived particle size to XRD results strongly suggests that the studied crystallites were representative for the bulk.

4.4 Conclusions

ET in combination with a posteriori image processing was successfully applied to study the size distribution and 3D location of single NiO crystallites in individual SBA-15 pores. Statistical analysis confirms a commonly assumed log-normal size distribution with a volume-weighted maximum at 4 nm, which was in excellent agreement with the crystallite size determined by XRD. Inter-particle distances between nearest-neighboring crystallites were 1 to 3 nm with very few isolated crystallites. The local loading in filled pores was almost twice the applied overall loading of the support and significant variations existed between and along the pores. The high local loading was compensated by a large percentage of unfilled pores. This suggests that a very high local loading combined with a high dispersion is achievable, if the filling of the pores during impregnation and drying is improved. ET has provided new quantitative information on the 3D structure of NiO/SBA-15 and is expected to play a major role in the characterization of nanostructured materials, in general, and heterogeneous catalysts, in particular

Acknowledgments

I would like to thank A. J. Koster, W. J. C. Geerts, J. D. Meeldijk, T. P. van der Krift, M. N. Lebbink, A. Yakushevskaya, and M. Barcena for their support.

Supporting Information Available

Slices.mpg - a movie of consecutive numerical cross-sections through reconstruction A of NiO/SBA-15 structure, with the relative location of the three segmented SBA-15 pores indicated. This material is available free of charge via the Internet at <http://pubs.acs.org>.

References

- (1) Murray, C. B.; Norris, D. J.; Bawendi, M. G. *J. Am. Chem. Soc.* **1993**, *115*, 8706.
- (2) Bala, T.; Sankar, C. R.; Baidakova, M.; Osipov, V.; Enoki, T.; Joy, P. A.; Prasad, P. L. V.; Sastry, M. *Langmuir* **2005**, *21*, 10638.
- (3) Bezemer, G. L.; Bitter, J. H.; Kuipers, H. P. C. E.; Oosterbeek, H.; Holeywijn, J. H.; Xu, X.; Kaptein, F.; van Dillen, A. J.; de Jong, K. P. *J. Am. Chem. Soc.* **2006**, *128*, 3956.
- (4) Kresge, C. T.; Leonowicz, M. E.; Roth, W. J.; Vartuli, J. C.; Beck, J. S. *Nature* **1992**, *359*, 710.
- (5) Beck, J. S.; Vartuli, J. C.; Roth, W. J.; Leonowicz, M. E.; Kresge, C. T.; Schmitt, K. D.; Chu, C. T.-W.; Olson, D. H.; Sheppard, E. W.; McCullen, S. B.; Higgins, J. B.; Schlenkert, J. L. *J. Am. Chem. Soc.* **1992**, *114*, 10834.
- (6) Zhao, D.; Feng, J.; Huo, Q.; Melosh, N.; Fredrickson, G. H.; Chmelka, B. F.; Stucky, G. D. *Science* **1998**, *279*, 548.
- (7) Janssen, A. H.; Van Der Voort, P.; Koster, A. J.; de Jong, K. P. *Chem. Commun.* **2002**, 1632.
- (8) Janssen, A. H.; Yang, C.-M.; Wang, Y.; Schüth, F.; Koster, A. J.; de Jong K. P. *J. Phys. Chem. B* **2003**, *107*, 10552.
- (9) Ziese, U.; de Jong, K. P.; Koster A. J. *Appl. Catal., A* **2004**, *260*, 71.
- (10) Ravikovitch, P. I.; Neimark A. V. *J. Phys. Chem. B* **2001**, *105*, 6817.
- (11) Van Der Voort, P.; Ravikovitch, P. I.; de Jong, K. P.; Neimark, A. V.; Janssen, A. H.; Benjelloun, M.; Van Bavel, E.; Cool, P.; Weckhuysen, B. M.; Vasant, E. F. *Chem. Commun.* **2002**, 1010.
- (12) Khodakov, A. Y.; Zholobenko, V. L.; Bechara, R.; Durand, D. *Microporous Mesoporous Mater.* **2005**, *79*, 29.
- (13) Esparza, J. M.; Ojeda, M. L.; Campero, A.; Domínguez, A.; Kornhauser, I.; Rojas, F.; Vidales, A. M.; López, R. H.; Zgrablich, G. *Colloids Surf., A* **2004**, *241*, 35.
- (14) Sietsma, J. R. A.; Van Dillen, A. J.; de Jongh, P. E.; de Jong, K. P. *Stud. Surf. Sci. Catal.* **2006**, *162*, 95.
- (15) Kantorovich, D.; Haviv, L.; Vradman, L.; Landau, M. V. *Stud. Surf. Sci. Catal.* **2005**, *156*, 147.
- (16) Vradman, L.; Landau, M. V.; Kantorovich, D.; Koltypin, Y.; Gedanken, A. *Microporous Mesoporous Mater.* **2005**, *79*, 307.
- (17) Cho, Y. S.; Park, J. C.; Lee, B.; Kim, Y.; Yi, J. *Catal. Lett.* **2002**, *81*, 89.
- (18) Li, X.-K.; Ji, W.-J.; Zhao, J.; Wang, S.-J.; Au, C.-T. *J. Catal.* **2005**, *236*, 181.
- (19) Park, Y.; Kang, T.; Kim, P.; Yi J. *J. Colloid Interface Sci.* **2006**, *295*, 464.
- (20) Satterfield, C. N. *Heterogeneous Catalysis in Practice*; McGraw-Hill: New York, 1980.
- (21) Bond, G. C. *Heterogeneous Catalysis*; Oxford University Press: Oxford, 1988.
- (22) Augustine, R. L. *Heterogeneous Catalysis for the Synthetic Chemist*; Marcel Dekker, Inc: New York, 1996.
- (23) van der Lee, M. K.; van Dillen, A. J.; Bitter, J. H.; de Jong, K. P. *J. Am. Chem. Soc.* **2005**, *127*, 13573.
- (24) Meurig Thomas, J.; Midgley, P. A. *Chem. Commun.* **2004**, 1253.

- (25) Datye, A. K. *J. Catal.* **2003**, *216*, 144.
- (26) Gai, P. L.; Boyes E. D. *Electron microscopy in heterogeneous catalysis*; Institute of Physics Publishing: Bristol, 2003.
- (27) Anderson, M. W.; Ohsuna, T.; Sakamoto, Y.; Liu, Z.; Carlsson, A.; Terasaki, O. *Chem. Commun.* **2004**, 907.
- (28) Smith, D. J.; Yao, M. H.; Allard, L. F.; Datye, A. K. *Catal. Lett.* **1995**, *31*, 57.
- (29) Bore, M. T.; Pham, H. N.; Switzer, E. E.; Ward, T. L.; Fukuoka, A.; Datye, A. K. *J. Phys. Chem. B* **2005**, *109*, 2873.
- (30) Hawkes, P. W. *The Electron Microscope as a Structure Projector*. in Frank, J. ed. *Electron Tomography : Three-Dimensional Imaging with the Transmission Electron Microscope*; Plenum Press: New York, 1992.
- (31) Weyland, M.; Midgley, P. A.; Meurig Thomas, J. *J. Phys. Chem. B* **2001**, *105*, 7882.
- (32) de Jong, K. P.; Koster, A. J. *ChemPhysChem* **2002**, *3*, 776.
- (33) Ziese, U.; Gommès, C. J.; Blacher, S.; Janssen, A. J.; Koster, A. J.; de Jong, K. P. *Stud. Surf. Sci. Catal.* **2005**, *158*, 633.
- (34) Gommès, C. J.; de Jong, K. P.; Pirard, J. P.; Blacher S. *Langmuir* **2005**, *21*, 12378.
- (35) Midgley, P. A.; Meurig Thomas, J.; Laffont, L.; Weyland, M.; Raja, R.; Johnson, B. F. G.; Khimyak, T. *J. Phys. Chem. B.* **2004**, *108*, 4590.
- (36) Sietsma, J. R. A.; van Dillen, A. J.; de Jongh, P. E.; de Jong K. P. *Angew. Chem. Int. Ed.* **2007**, *46*,4547.
- (37) Tarazona, P. *Phys. Rev. A* **1985**, *31*, 2672.
- (38) Tarazona, P. *Phys. Rev. A* **1985**, *32*,3148.
- (39) Tarazona, P.; Marini Bettolo Marconi, U.; Evans, R. *Mol. Phys.* **1987**, *60*, 573.
- (40) Kremer, J. R.; Mastronarde, D. N.; McIntosh, J. R. *J. Struct. Biol.* **1996**, *116*, 71.
- (41) Imperor-Clerc, M.; Bazin, D.; Appay, M.-D.; Beaunier, P.; Davidson, A. *Chem. Mater.* **2004**, *16*, 1813.
- (42) Moreno, M. S.; Weyland, M.; Midgley, P. A.; Bengoa, J. F.; Cagnoli, M. V.; Gallegos, N. G.; Alvarez, A. M.; Marchetti, S. G. *Micron* **2006**, *37*, 52.
- (43) Jentys, A.; Kleestorfer, K.; Vinek H. *Microporous and Mesoporous Mater.* **1999**, *27*, 321.
- (44) Penczek, P.; Marko, M.; Buttle, K.; Frank J. *Ultramicroscopy* **1995**, *60*, 393.
- (45) Mastronarde D. N. *J. Struct. Biol.* **1997**, *120*, 343.
- (46) Midgley, P. A.; Weyland, M. *Ultramicroscopy* **2003**, *96*, 413.
- (47) Radermacher, M.; Hoppe, W. Proceedings of the Seventh European Congress on Electron Microscopy, Den Haag, **1980**, 132.
- (48) Granqvist, C. G.; Buhrman R. A. *J. Catal.* **1976**, *42*, 477.
- (49) Datye, A. K.; Xu, Q.; Kharas, K. C.; McCarty, J. M. *Catal. Today* **2006**, *111*, 59.



Chapter 5

Quantifying the 3D Structure of Nanomaterials by Threshold-based Segmentation of Electron Tomograms

Abstract

A method for automated segmentation of electron tomograms by combining edge detection with single value thresholding is proposed. Its suitability and accuracy are validated in simulation and experiments on a colloidal gold model system, a Ru/carbon nanotube catalyst, and an Au@zirconia system. ET revealed a difference in the Ru particle size distribution depending on the location, i.e., inside (1–4 nm) or outside (1–3 nm) the nanotube. Approximately 80 wt% of the ruthenium was deposited inside the tube at a local loading of 3.2 wt%. The Au@zirconia system consisted of 18 nm Au particles stabilized against sintering in close to spherical zirconia shells of varying thickness. The shells were highly porous, sometimes connected, and composed of on average 5 nm sized zirconia crystallites. ET gives detailed quantitative insight into the 3D morphology of nanostructured catalysts and will in the future contribute to a more rational design of this important class of materials.

5.1 Introduction

In the last decade the range of materials studied by electron tomography (ET) has extended dramatically.¹⁻⁸ While ET has been applied in biology for more than three decades,^{9,10} it now spans also the physical and chemical sciences.¹¹⁻¹³ The recent interest in ET is strongly connected to advances in shaping and patterning materials on the nanoscale. One of the most important classes of nanostructured materials are heterogeneous catalysts as they are essential for the industrial production of transportation fuels, chemicals, and drugs.¹⁴⁻¹⁶

The ability of ET to give detailed insight into the three-dimensional (3D) morphology of complex nanostructured materials has considerably contributed to the understanding of their physico-chemical properties. While sometimes a qualitative description of structural characteristics, e.g. pore connectivity in zeolites or distribution of active components in supported catalysts, is sufficient,^{1,2,17-20} more and more often a detailed quantification on the nanoscale, e.g. pore size distributions,^{21,22} and particle size distributions,^{4,7,8} and particle-particle distances^{4,7} is required.

Quantification can be achieved by segmenting the tomogram and subsequently analyzing the structure of individual components/objects. Methods can include information on the object shape²²⁻²⁴ or consider the information in the gray level histogram.^{4,25,26} At present, segmentation by thresholding the recorded gray levels (binarization) to distinguish objects from the background is most frequently applied in materials science electron tomography.^{4,6,21,26-29} The segmentation threshold (t) has to be determined by the user or by automatic procedures and results are commonly validated just visually.^{30,31} An illustration of the problems involving visual validation is presented in Figure 1. While the binarized datasets (Figure 1b,c and Figure 1e,f) closely approximate what can be seen in the reconstruction (Figure 1a and 1d, respectively) there is a significant difference in the corresponding particle size distributions (Figure 1h). Moreover, the difference in segmented volume was in this case approximately 40%. In particular for heterogeneous catalysts, where small differences in particle size might have a significant impact on the catalytic activity,³² above uncertainties are hard to tolerate.

In general, manual adjustment of the threshold based on visual inspection, which is likely to give different results at different times and/or by different operators, should be avoided, if possible.³⁰ Also for automated procedures that utilize the information in the gray level histogram the resulting thresholds may differ significantly depending on which method is employed.³³ For example, using the dataset shown in Figure 1, the isodata algorithm³⁴ computes -1110, Otsu's method³⁵ -350, and the triangle procedure³⁶ 512 as corresponding thresholds.

A more physical criterion for demarking interfaces is the detection of edges based on the steepest intensity gradient.³⁷ Edge definitions based on zero crossings of the second order derivative are common, but sensitive to noise.^{38,39} In addition, the edge of an object might

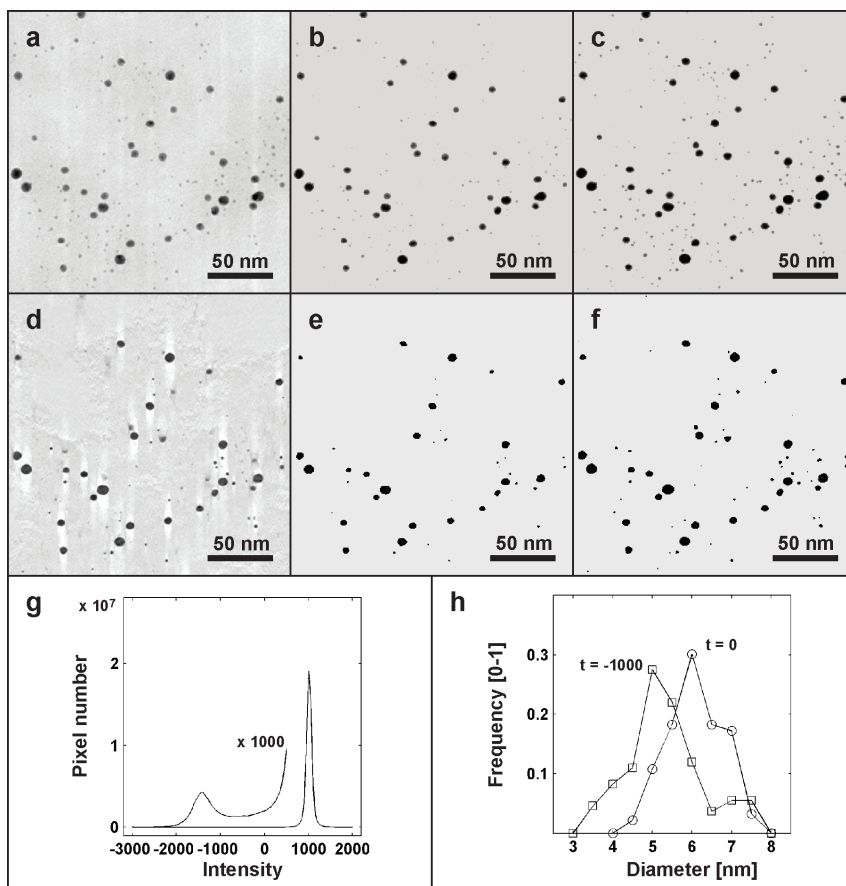


Figure 1 Colloidal Au particles on carbon support film (0.54 nm pixel size) with projection (not thresholded) of reconstruction (a), projection of thresholded reconstruction at $t=-1000$ (b), projection of thresholded reconstruction at $t=0$ (c), numerical cross-section (not thresholded) displayed for intensity levels between -2500 and 1500 (d), thresholded cross-section at $t=-1000$ (e), thresholded cross-section at $t=0$ (f), gray level histogram (g), particle size distributions for $t=-1000$ and $t=0$ (h).

correspond to different gray levels in different positions which challenges the common assumption that reconstructed intensities scale with the scattering strength of the material. Here we propose a criterion that combines edge detection with single value thresholding for automated, reproducible and operator-independent quantification of electron tomograms. The suitability and accuracy of our method is validated by numerical simulations and in three experimental case studies: i) a model system of nanosized colloidal gold particles, ii) ruthenium nanoparticles supported on carbon nanotubes (CNT), and iii) a gold catalyst stabilized against sintering in size and shape persistent zirconia nanocontainers.

5.2 Experimental

5.2.1 Catalyst preparation

Synthesis of the Au@ZrO₂ catalysts proceeded in four steps following an earlier published procedure.⁴⁰ First, to 212.5 ml of demi water under reflux an HAuCl₄ solution (25 ml, 2.54·10⁻³ M) was added, heated and stirred until the boiling point was reached again. Then, a sodium citrate solution (12.5 ml, 10 mg.ml⁻¹) was added, the system refluxed for an additional 30 min, and finally cooled to room temperature. Second, an aqueous solution of polyvinylpyrrolidone (0.325 ml, 12.8 mg.ml⁻¹) was added to 240 ml of the colloidal gold solution, stirred for 24 h to allow complete adsorption of the polymer on the gold surface. After centrifugation and removal of the supernatant, the concentrated colloid was diluted to 6 mL with demi water under rapid stirring. Subsequently, 18.9 ml of ethanol premixed with 0.84 ml concentrated ammonia solution (28–30% NH₃ in H₂O) was added, followed by 1.19 ml of tetraethylorthosilicate in 12.8 ml ethanol. The reaction mixture was then stirred for an additional 12 h at room temperature, and finally centrifuged and washed twice with water and twice with absolute ethanol. Third, the solid was redispersed by ultrasonication in 25 g of pure ethanol, sealed in a 100 ml flask, and heated under stirring at 30 °C. Then 0.125 ml of an aqueous solution of Lutensol AO5 (from BASF; 0.43 g dissolved in 11 g MilliQ water) was added to the stirred solution. After 1 h, 0.45 ml zirconium butoxide in butanol (80 % wt.wt⁻¹) was added and the reaction proceeded overnight. The colloid was then four times washed and redispersed in 25 ml of water. After aging at 20 °C for 3 days, the organics were removed and the zirconia crystallized by heating from room temperature to 900 °C in air at a heating rate 2 K.min⁻¹. Fourth, the silica was removed in an NaOH solution (1 N) under stirring for 16 h, after which the solution was exchanged and the process continued for an additional 12 h at 50 °C. Finally, the core–shell particles were washed five times with water and once with ethyl tert-butyl ether.

Synthesis of the Ru/carbon nanotube (CNT) catalyst proceeded via wet impregnation following earlier published procedures.⁴¹⁻⁴³ First, CNT (Chengdu Organic Chemicals, 4-8 nm inner diameter, 10-20 nm outer diameter), were refluxed in HNO₃ (68 wt %) at 140 °C for 14 h. Then the mixture was filtered, the CNT washed in de-ionized water and dried at 60 °C for 12 h. Second, a 0.32 ml RuCl₃ / acetone solution (15 mg.ml⁻¹) was further diluted to 18 ml and then 120 mg CNTs were added under ambient conditions. Ultrasonication for 4 h aided in filling of the CNT channel by capillary forces. The mixture was then further stirred at ambient conditions to allow slow evaporation of the acetone. Third, the mixture was gradually heated and kept in air at 110 °C for 11 h and subsequently reduced in H₂ for 5 h at 450 °C.

5.2.2 TEM sample preparation

ET samples of the catalyst materials were prepared in two steps. First, 6 nm colloidal gold particles⁴⁴ were applied from aqueous suspension to a carbon support film on a 200 mesh Cu parallel bar TEM grid, followed by drying in air. The support film consisted of a Quantifoil R2/1 holey carbon film with an additional 2-3 nm thick continuous carbon layer on top. Second, approximately 5 mg of the catalyst powder was suspended in 1-5 ml of ethanol by ultrasonication. Subsequently, one to three droplets of the suspension were applied to the gold labeled TEM grid, followed by drying at 60 °C for at least 30 min. Another sample containing only colloidal gold particles of nominally 1-2 nm, 6 nm, 10 nm, 15 nm and 25 nm in size were prepared by depositing a drop of a mixed colloidal suspension (Aurion 800.266, 406.011, 410.011, 415.011, 425.011) to a TEM sample grid, as described above, followed by drying in air.

5.2.3 Characterization

Powder X-ray diffraction measurements were performed at room temperature with a Bruker-AXS D8 Advance diffractometer using Co-K_{α12} radiation with a wavelength of 0.179 nm. Powder XRD patterns were collected over an angular range of 20° to 80° 2θ. Crystallite sizes were determined from the width of the diffraction peaks using EVA software (version 14.0 Bruker AXS).

ET was performed in bright-field TEM mode on a Tecnai 20 electron microscope, operated at 200kV. The microscope was equipped with a TWIN objective lense and a LaB₆ electron source. Series of images (tilt-series) were acquired by rotating the specimen in the electron beam over an angular range of at least ±72° at 1° or 2° increments. For data acquisition a 40 μm objective aperture was inserted in the beam path. To reduce background effects of the carbon support at high tilt angles, structures supported only on the 2–3 nm continuous carbon film were imaged. Images were recorded on a 2048 x 2048 pixel TVIPS CCD camera using Xplore3D (FEI) software. Changes in object position and defocus were corrected at each step of the series. The defocus was set to -100 nm and -400 nm (nominal) depending on the magnification and size of the studied structures to keep the entire object in underfocus. Images of the tilt-series were aligned with respect to a common origin and rotation axis using the colloidal gold particles or other high contrast objects as fiducial markers. Alignment and reconstruction by filtered backprojection were performed in IMOD.⁴⁵ Image analysis of the tomograms was performed in Matlab (The MathWorks, Inc.) using in part functions of the TOM toolbox⁴⁶ and the Delft Image Processing library (www.diplib.org).

5.3 Image analysis

In general, electron tomograms will contain intensity variations that can be interpreted in terms of imaged object property. For medium resolution bright-field TEM ET (BF ET) of catalyst materials contrast arises in first approximation (disregarding diffraction effects and phase contrast contributions) from differences in scattering strength of the material, i.e. mass-density. In BF ET objects of high mass-density, e.g., metals will appear dark. To distinguish objects from the background directly (binarization or thresholding) an intensity threshold t can be chosen such that all pixels with a lower intensity value belong to the objects of interest and all pixel with an intensity value higher than t are background. In contrast to approaches that use the information in the gray level histogram, our method focuses on finding the threshold that corresponds to the globally highest intensity gradient. In Figure 2, a simple schematics of the two dimensional equivalent is displayed. An object (Figure 2a), will be blurred by the point-spread-functions (PSF) of the imaging and reconstruction processes (Figure 2b). This results in edges that gradually evolve from the background intensity to the intensity within the original object (Figure 2c). Assuming that edges are not linear, intensity contours at constant increments (Figure 2d) will not be equally spaced. In the following the differences in spacing between intensity contours at constant increments are utilized to determine the highest intensity gradient.

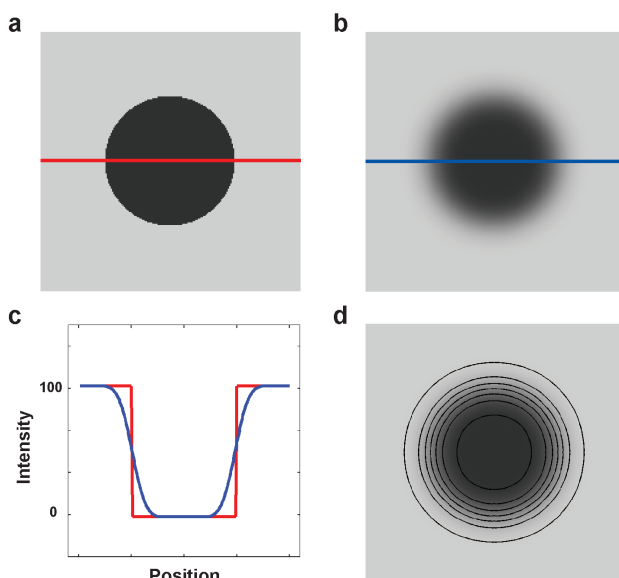


Figure 2 Schematics of edge and threshold determination. Disk model (a), Gaussian blurred disk (b), intensity profiles (c), and blurred disk with intensity contours at constant increments overlaid (d).

The distance d between neighboring contours will depend on the threshold (t) and the increment (Δt). If the image is thresholded at t and $t+\Delta t$ an approximation of $d(t,\Delta t)$ can be obtained using the measured area and perimeter values of the two binarized objects.

$$d(t, \Delta t) = \text{shapefactor} \cdot \frac{\text{Area}(t + \Delta t) - \text{Area}(t)}{\text{Perimeter}(t + \Delta t) + \text{Perimeter}(t)} \quad (1)$$

Figure 3 illustrates the process of edge detection using equation 1. In Figure 3a the area differences calculated for the model in Figure 2d, corresponding to $t=20,50,80$ ($\Delta t=5$), are displayed. Figure 3b shows the results for the model in Figure 2d evaluated over a range of thresholds ($\Delta t=5$, shapefactor=1) and third order polynomial fit. Figures 3c,d and 3e,f display the equivalent information for two other shapes. The minima in the three curves correspond to the gray level halfway between the background (100) and the object (0). Differences in shape change the absolute values of $d(t,\Delta t)$ but not the threshold at which the minimum in the curve, i.e. the highest intensity gradient, is found.

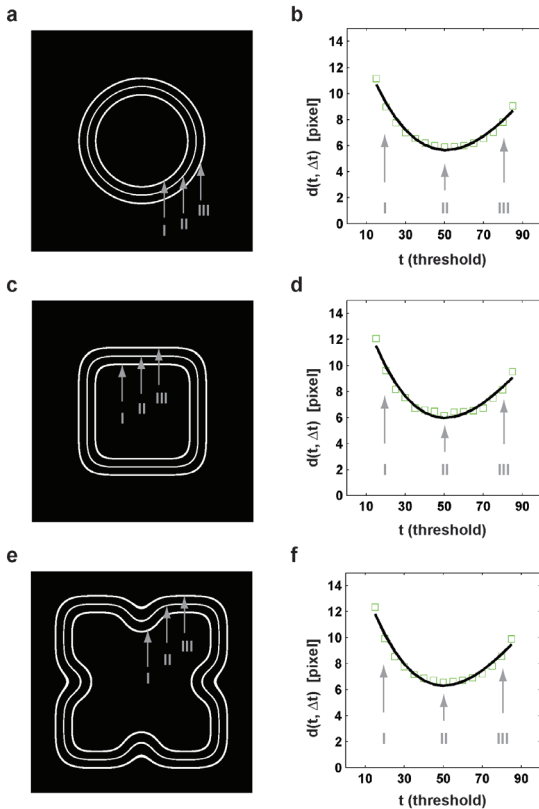


Figure 3 Edge detection using equation 1 for Gaussian blurred disk (a,b), Gaussian blurred square (c,d), Gaussian blurred ‘clover leaf’ (e,f). Area differences calculated for $t=20,50,80$ and $\Delta t=5$ (a,c,e), threshold criterion (shapefactor =1) with third order polynomial fit (b,d,f).

Equation 1 for edge detection in two dimensions can be extended into three dimensions using the volume and surface area of segmented objects. In 3D it reads:

$$d(t, \Delta t) \sim \frac{Volume(t + \Delta t) - Volume(t)}{SurfaceArea(t + \Delta t) + SurfaceArea(t)} \quad (2)$$

In the following only the proportionality is exploited (shapefactor=1) to find the minimum distance between isosurfaces (isolines in 2D) corresponding to the globally (averaged over all directions and all objects) highest intensity gradient.

The influence of sampling, imaging and reconstruction on the detection of small objects was simulated. A schematic of the simulation is displayed in Figure 4. We start from a 3D model containing 20 spheres with diameters ranging from 1 to 20 pixels. In the first step the model was projected to obtain a tilt series. Second, images of the tilt-series were filtered, as explained in the next paragraph, to approximate the experimental imaging conditions. Subsequently, Poisson distributed noise was added (as measured in the TEM images of the colloidal gold model system) resulting in a signal-to-noise-ratio of 3, 6, and 9 for spheres with a diameter of 5, 10, and 15 pixels, respectively. Third, the tilt-series was reconstructed in IMOD introducing a reconstruction PSF. In the fourth step the segmentation threshold was determined using the criterion in equation 2, the reconstruction binarized, and the volume and surface area measured for the 20 spheres. Measurements of volumes and surface areas were carried out using the measure function of the DIPimage library. A direct comparison of gray levels, as in the case of the Gaussian blurred 2D model, is not possible on account of rescaling by the weighted backprojection algorithm.

An approximation of the imaging filter, i.e. the imaging point-spread-function (PSF), was obtained by taking the objective aperture size and the spherical aberration coefficient of the objective lens into account. For an ideal lens, the Rayleigh criterion yields a minimum spatial resolution of:

$$\delta_{OA} = 1.22 \cdot \frac{f\lambda}{D} \quad (3)$$

with f the focal length (3 mm for a TWIN objective lens), λ the wavelength (2.54 pm for 200 kV electrons), and D the diameter of the objective aperture (40 μ m). The spherical aberration coefficient ($C_s = 2$ mm) of the objective lens will introduce an additional blurring which can be estimated by ⁴⁷:

$$\delta_{C_s} = 0.5 \cdot C_s \cdot \alpha_0^3 \quad (4)$$

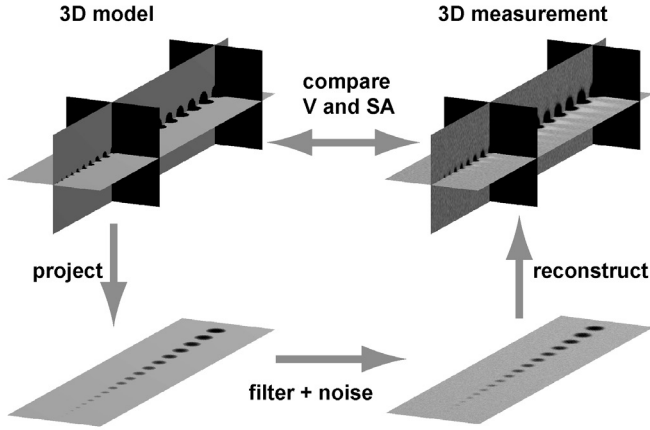


Figure 4 Schematics of simulation.

with α_0 the convergence semi angle which is equivalent to $D/2f$. The resulting blurring can be treated approximately as a quadratic superposition of the error-disk diameters and assuming a Gaussian error-disk shape.

$$\delta_{total} = \sqrt{\delta_{OA}^2 + \delta_{Cs}^2} \approx 0.38 \text{ nm} \quad (5)$$

In a conservative estimate the imaging PSF can for the smallest experimental pixel size of 0.16 nm be described by a Gaussian with a standard deviation (STD) of 1.2 pixel. The imaging PSF reduces to a Gaussian with a STD of 0.6 pixel for a two times binned tilt-series (0.32 nm pixel at the highest experimental magnification, 50 k \times).

In the following we studied the effects of the reconstruction, imaging, noise, and tilt increment on the threshold criterion and measured volumes and surface areas on the model of 20 spheres (Figure 4). The results of such a study assuming single axis tilting over an angular range of $\pm 70^\circ$ at 1° increments are presented in Figure 5. The threshold criterion in Figure 5a shows two minima which is an artifact that is caused by the reconstruction algorithm. Addition of noise and blurring by the imaging PSF (Figure 5c,e) greatly reduces this artifact resulting in flat valleys in the curves. The apparent flatness introduces an uncertainty in finding the curve minimum, which was approximated to ± 100 intensity levels in this case.

In Figure 5b,d,f the correspondence between model and measured object diameters is displayed. Error bars were calculated by thresholding at ± 100 intensity levels from the minimum of the polynomial fit and their magnitude was comparable between objects of different sizes, e.g. approximately ± 0.6 pixel in Figure 5d and ± 1 pixel in Figure 5f. In general, a sampling dependence of measured volume and surface area was observed. For objects below 10 pixels in diameter, blurring dampens the contrast, thus causing an underestimation of their size. Nevertheless, detection seems feasible for ~ 1 nm objects (Figure 5d, 3 pixel diameter, 0.32 nm/pixel or Figure 5f, 5 pixel diameter, 0.16 nm/pixel) to within 25 % of their actual size. The simulation also predicts that objects of 2 nm in diameter and larger are detected to within 10 % of their respective size, including the uncertainty in segmentation threshold.

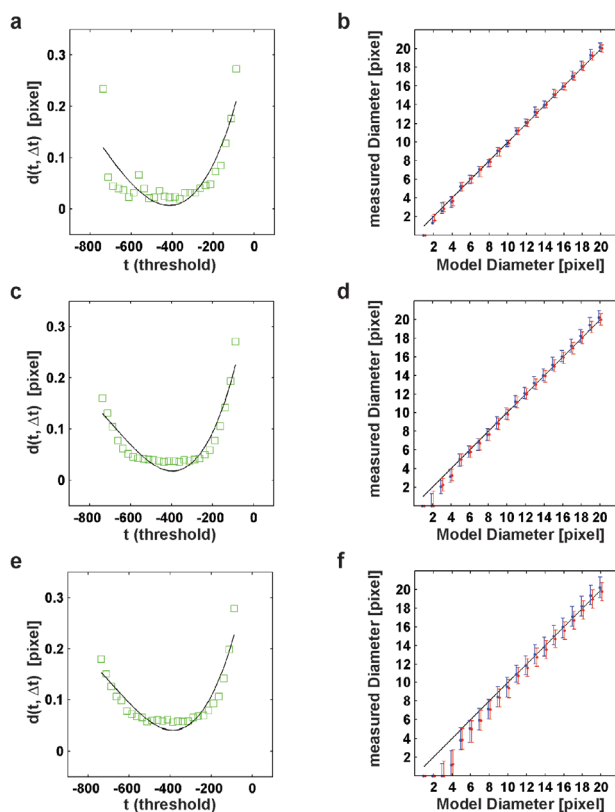


Figure 5 Simulation results for single-axis tilting series over $\pm 70^\circ$ at 1° increments showing threshold criterion (green) with third order polynomial fit (black) on the left and the measured diameters using the volume (red), surface area (blue) and one-to-one correlation (black) on the right. Reconstruction without blurring or noise (a,b), reconstruction from blurred (STD=0.6) and noisy data (c,d), reconstruction from blurred (STD=1.2) and noisy data (e,f). The error bars in (b,d,f) were calculated by thresholding at ± 100 intensity levels from the minimum of the polynomial fit.

In Figure 6 the results of a simulation assuming single axis tilting over an angular range of $\pm 70^\circ$ at 2° increments are presented. Increasing the tilt increment from 1° to 2° , thus effectively halving the number of images in the tilt series, has no significant effect. Thus, experimental data acquired at 1° and 2° increments will be treated equivalently.

In summary, the uncertainty in threshold has the most significant effect on measured volumes and surface areas, followed by the imaging PSF in combination with sampling that lead to an underestimation of the size of small objects. This permits analysis of experimental datasets down to approximately 1 nm sized objects within the boundaries of the presented model and experimental parameters.

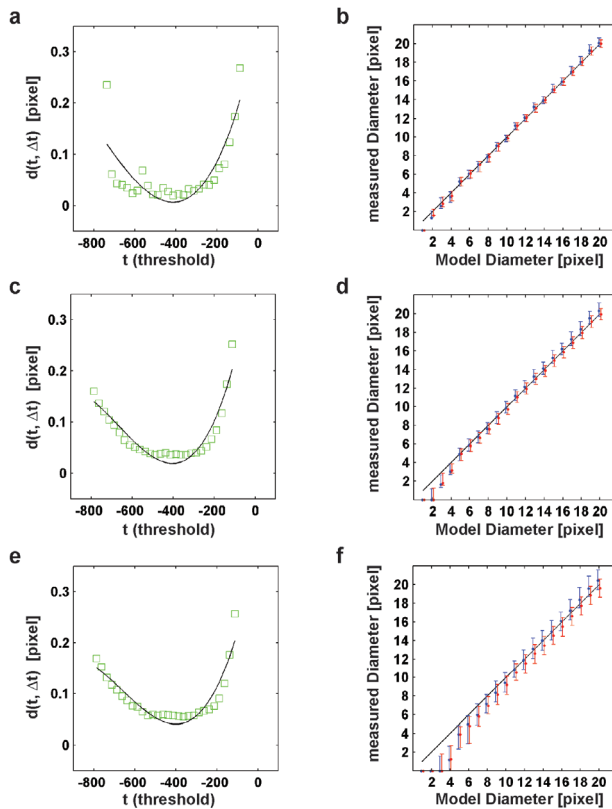


Figure 6 Simulation results for single-axis tilting series over $\pm 70^\circ$ at 2° increments showing threshold criterion (green) with third order polynomial fit (black) on the left and the measured diameters using the volume (red), surface area (blue) and one-to-one correlation (black) on the right. Reconstruction without blurring or noise (a,b), reconstruction from blurred (STD=0.6) and noisy data (c,d), reconstruction from blurred (STD=1.2) and noisy data (e,f). The error bars in (b,d,f) were calculated by thresholding at ± 100 intensity levels from the minimum of the polynomial fit.

5.4 Results and Discussion

5.4.1 Colloidal Au

The first example is a model system (Figure 1) consisting of nominally 1-2, 6, 10, 15, and 25 nanometer-sized colloidal gold particles. Figure 7a displays the threshold criterion calculated from three tomograms denoted A to C. All curves expose a clear minimum. The summed particle size distribution (PSD), displayed in Figure 7b, shows distinct peaks close to the nominal particle sizes. Throughout the remaining sections particle sizes are, independently of their actual shape, expressed in diameter of a sphere having the same volume. Since the number of larger particles was very small the statistical significance of the PSD above 7 nm is very low. Figure 7c displays the PSD for the two smallest particle classes and Figure 7d only for the smallest. Both curves show a narrow size distribution and agree well with the nominal values. Differences in frequency between panels b,c,d in Figure 7 arise from the different histogram bin sizes and normalization to a sum of one for each curve.

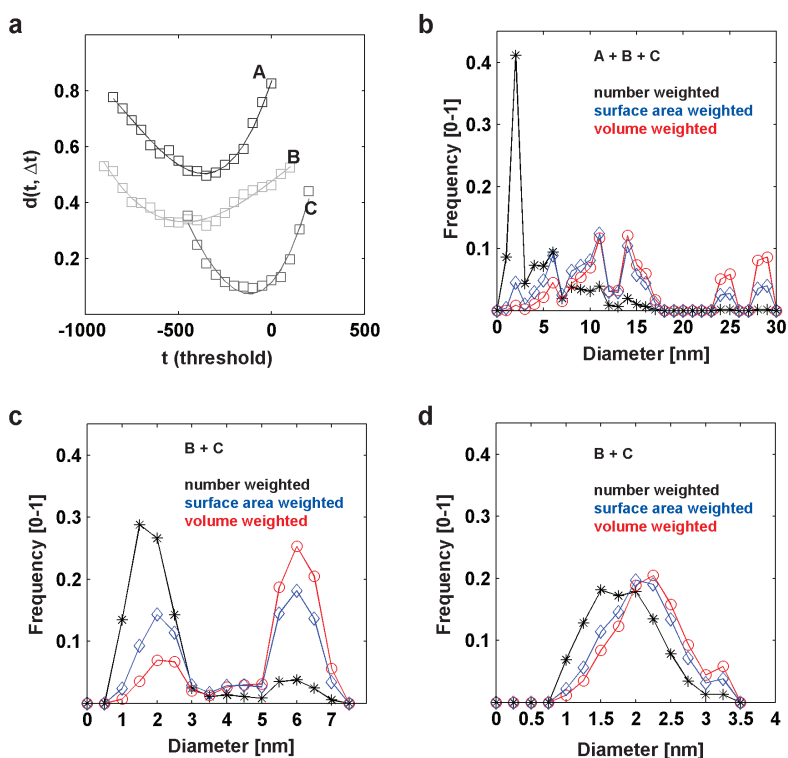


Figure 7 Quantitative analysis of colloidal gold model system showing threshold criterion with third order polynomial fit (a), PSD with a bin size of 1 nm from 617 particles (b), PSD with a bin size of 0.5 nm from 389 particles (c), and PSD with a bin size of 0.25 nm from 320 particles (d).

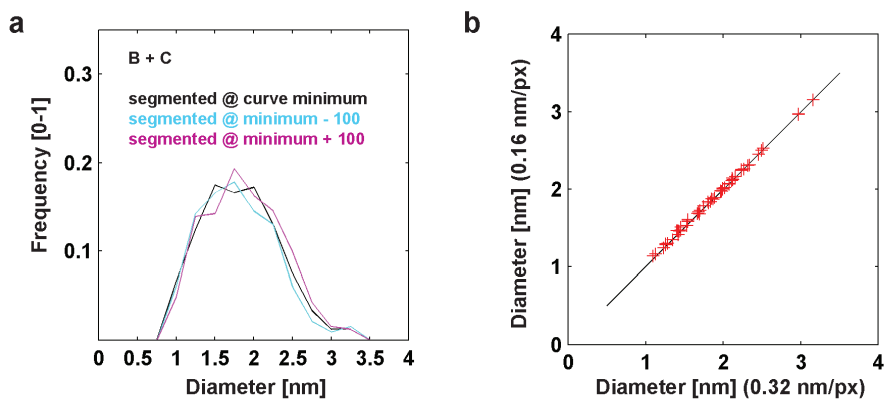


Figure 8 Particle size distributions of colloidal gold particles at different thresholds (a), and correlation between particles sizes using different sampling rates (b).

Although the threshold criterion curves (Figure 7a) show pronounced valleys, there is an uncertainty of approximately ± 100 gray levels in finding the minima. The effect of this error on the resulting particle size distribution is displayed in Figure 8a. Thresholding at 100 gray levels below and above the fitted minimum causes only a minor change in the corresponding particle size distributions. Also the effect of sampling on the measured particle sizes was investigated. To this end, dataset C was reconstructed at a sampling of 0.16 nm/px and of 0.32 nm/px, particles were identified based on their positions, and their respective sizes compared. The result of this analysis is displayed in Figure 8b. Although there is an eight fold difference in the number of pixel describing an object (e.g. a 2 nm particle contains 115 pixels @ 0.32nm/px or 900 pixels @ 0.16 nm/px) their respective sizes expressed in nanometers match.

In Figure 9 the results of the segmentation of dataset B are presented. The TEM image (Figure 9a) and an overlay with the segmented particles (Figure 9b) show a close match. Numerical cross-sections through the particle centers and binarized sections, displayed in Figure 9 c-f, illustrate the sampling for smallest Au colloids at a pixel size of 0.27 nm. In contrast to manual adjustments of the segmentation threshold or manually outlining the particles by hand, which might give different results depending on the operator, the presented methodology invokes a hard criterion, is automated, and thus reproducible and operator-independent. In addition, the threshold criterion provides an estimation of the measurement error based on the uncertainty in finding the minimum of the curve, i.e. the highest intensity gradient.

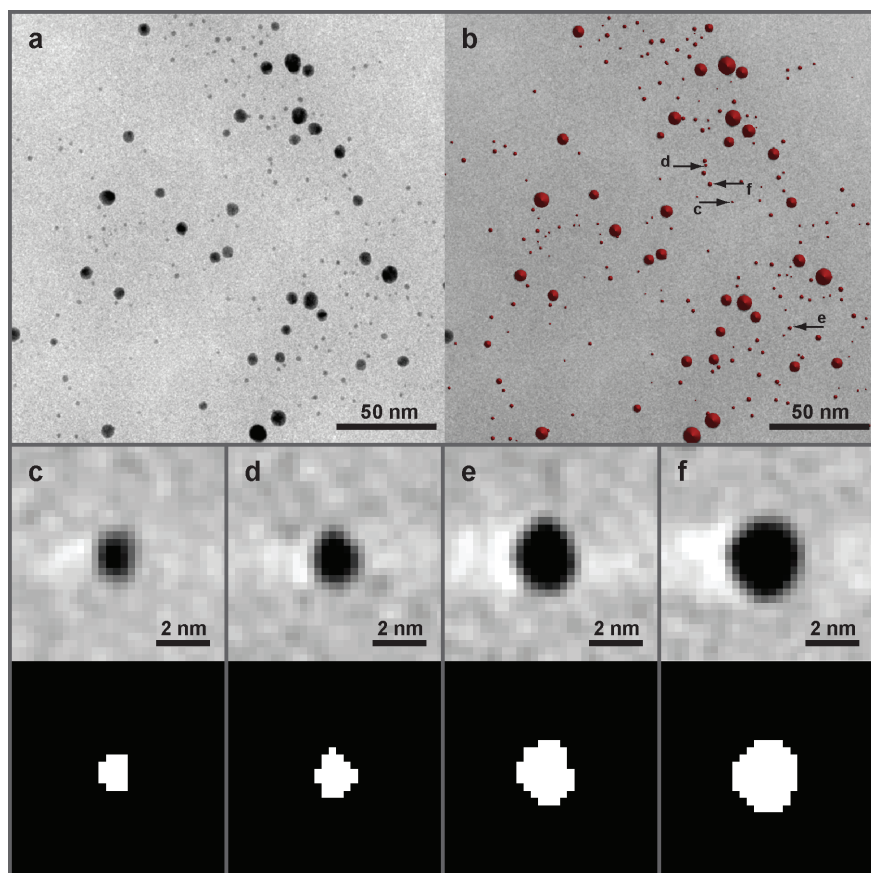


Figure 9 Examples for segmentation of colloidal gold model system showing TEM image of series at zero tilt (a), TEM image overlaid with segmented particles (b), and numerical cross-sections (0.27 nm/px) through Au particles and binarized sections (c-f).

5.4.2 Ru/carbon nanotube catalyst

The second example deals with ruthenium particles supported on carbon nanotubes (CNT). In Figure 10 the results of the quantitative analysis are displayed. The threshold criteria in Figure 10b show clear, but in some cases flat valleys, which will be discussed below. The particle size distribution (Figure 10c) exposes two distinct peaks which can be associated with the Ru particles (2 to 4 nm) and the colloidal gold markers (6 nm). The colloidal gold particles were deposited on the carbon support film prior to the catalyst materials and aid in alignment of the tilt-series with respect to a common origin and rotation axis. Please refer to section 5.2.2 and 5.2.3 on page 81 for more details.

While the flatness of some valleys could be a reconstruction artifact, in this case it could also be related to the presence of two materials (Ru and Au) of similar but not identical contrast. Sampling limitations for the Ru particles below 2 nm required ET to be performed at higher magnification corresponding to a pixel size of 0.32 nm for the two times binned tilt series. In this case, no colloidal gold was deposited on the carbon support, as it was found that the Ru particles themselves could be used.

In Figure 11 the results of the analysis at 0.32 nm pixel size are displayed. As in above examples evaluation of the threshold criterion was successful (Figure 11b). The distribution curves in Figure 11c confirmed the results at lower magnification and were in agreement with previous studies.⁴³ The apparent roughness in the volume and surface area weighted curves was caused by the low particle number. The error in finding the minimum of the criterion curve was approximately ± 100 gray levels and the effect on the resulting particle size distribution is displayed in Figure 11d. Thresholding at 100 gray levels below and above the fitted minimum insignificantly changed the corresponding particle size distributions.

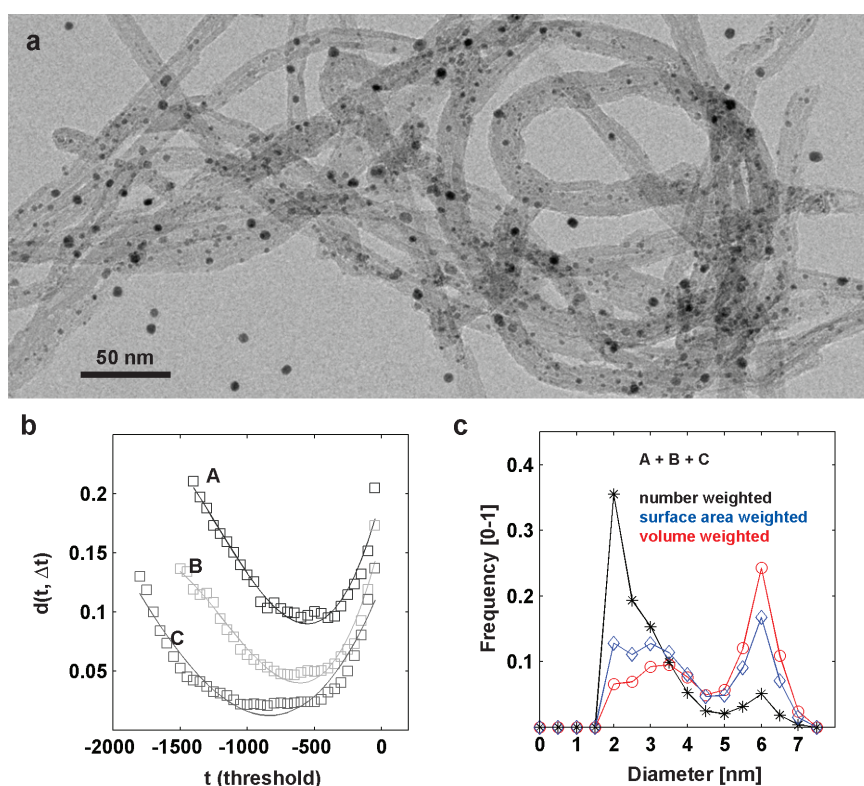


Figure 10 Quantitative analysis of Ru/CNT catalyst showing TEM image (a), threshold criterion (b), PSD of Ru particles and 6 nm Au markers, 1817 particles in total (c).

For CNTs the curvature of the tube wall can have a significant impact on the catalytic performance of metal particles depending on their position inside or outside of the tube.^{41,42} Thus, we extended our PSD analysis to include the location of the Ru particles. The corresponding PSDs displayed in Figure 11e,f illustrate that particles on the outside of the CNT are smaller than the particles inside the tube. While for this part of the sample only

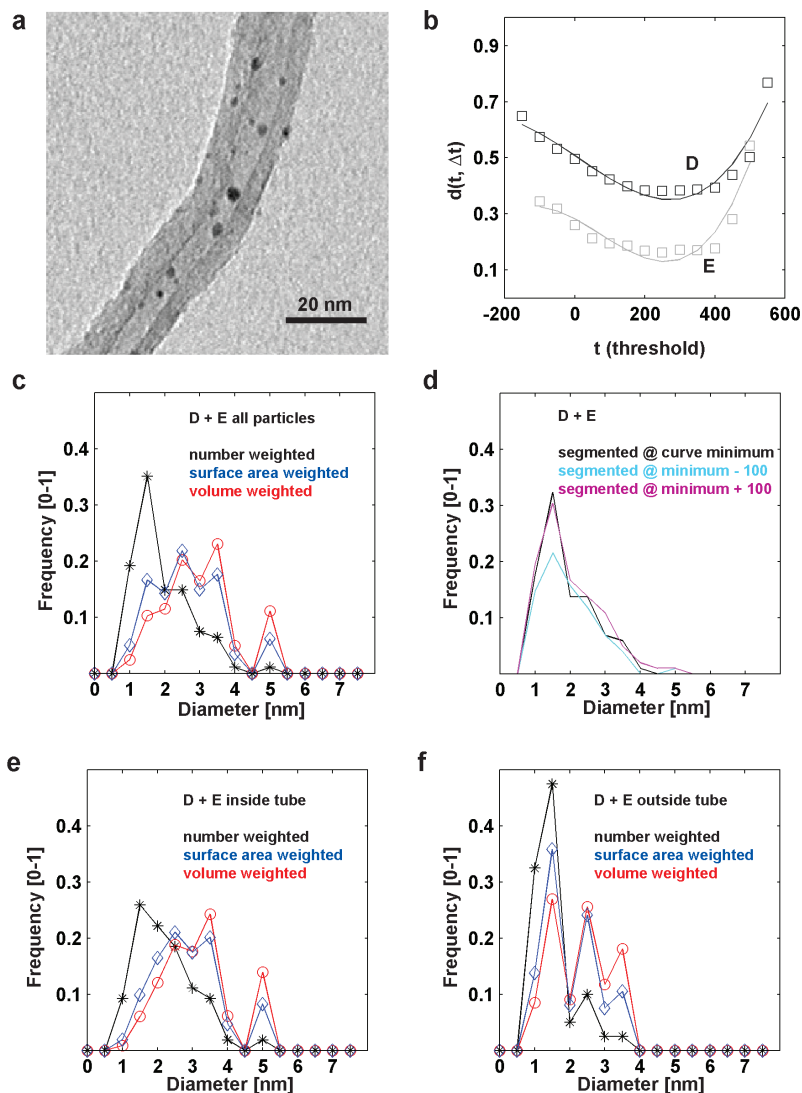


Figure 11 Quantitative analysis of Ru/CNT catalyst showing TEM image (a), threshold criterion (b), PSD of 94 Ru particles on CNT (c), effect of error in threshold (d), PSD of the 54 Ru particles located inside the CNT (e), and PSD of 40 Ru particles located outside the CNT (f).

60% of all particles were located inside, the differences in size resulted on a weight basis to approximately 80% of ruthenium inside the tube. This clearly shows that differences in the PSD depending on location have to be considered to accurately describe the filling of the CNT. To calculate the Ru loading, CNTs were approximated by hollow cylinders whose inner and outer diameter and length can be estimated from the reconstruction. The Ru loading was thus estimated to 3.2 wt% close to the intended value of 4 wt% from preparation.

An illustration of the 3D morphology the Ru/CNT system is presented in Figure 12. While the TEM image (Figure 12a) suggests that the particle indicated by arrow b is inside the tube, ET revealed its position on the outside (Figure 12b). Furthermore, a small Ru particle (Figure 12d) which was almost invisible in the TEM image was located inside the CNT wall, indicating the presence of cracks and/or encapsulation of Ru by carbon. The numerical cross-sections in Figure 12b-e also illustrate that the structure of the nanotube is more complex than the commonly assumed cylinder model. The round cross-section of the tube seems in some instances deformed at the location of the metal particles (Figure 12c,e). This could point, one the one hand, towards favorable deposition in locations of a higher local curvature arising from capillary forces on the impregnation solution.²⁸ On the other hand, a local deformation of the CNT as a result of the presence of the metal particle is also possible.⁴⁸

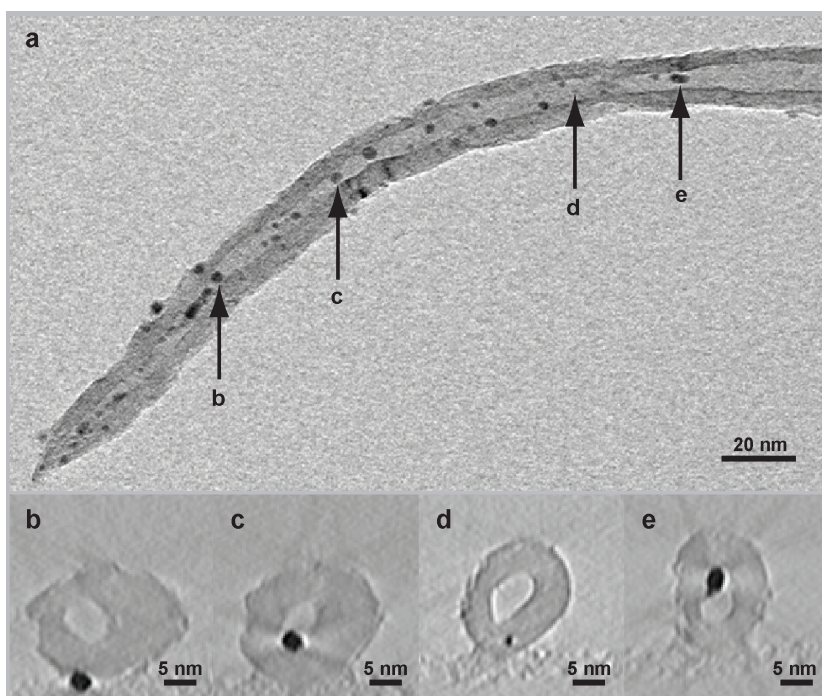


Figure 12 ET analysis of Ru/CNT catalyst showing TEM image (a), and numerical cross-sections through reconstruction perpendicular to TEM viewing direction (and in direction of arrows) to show the particle location (b-e).

5.4.3 Au@zirconia catalyst

The third example deals with a gold catalyst stabilized against sintering in size and shape persistent zirconia nanocontainers.⁴⁰ To obtain the particle size distribution of the colloidal gold particles, encapsulated by spherical zirconia shells, above methodology was employed. The results of this analysis are displayed in Figure 13. The threshold criterion (Figure 13b) displayed pronounced minima while differences in position are caused by the scaling of intensities by the reconstruction algorithm. Two distinct peaks in the size distribution are observed. The peak at ~ 18 nm corresponds to the gold colloid inside the zirconia and the peak at 6 nm reflects the fiducial marker size used in the alignment process. As in above examples the uncertainty in finding the minimum of the threshold curves (Figure 13b) has no significant effect on the resulting Au PSD.

Besides automated PSD determination for the Au colloids, the structure and particle size of ZrO_2 crystallites forming the porous zirconia shell was examined. Image analysis of the zirconia shells was carried out on a total of four sub-volumes (B1, B2, C1, C2) of the reconstructions B and C. Each sub-volume, 128^3 pixels in size and containing only zirconia, was first denoised using nonlinear anisotropic diffusion ($k=0.5$, 50 iterations).⁴⁹ Second, the threshold criterion was evaluated and the reconstructions subsequently binarized.

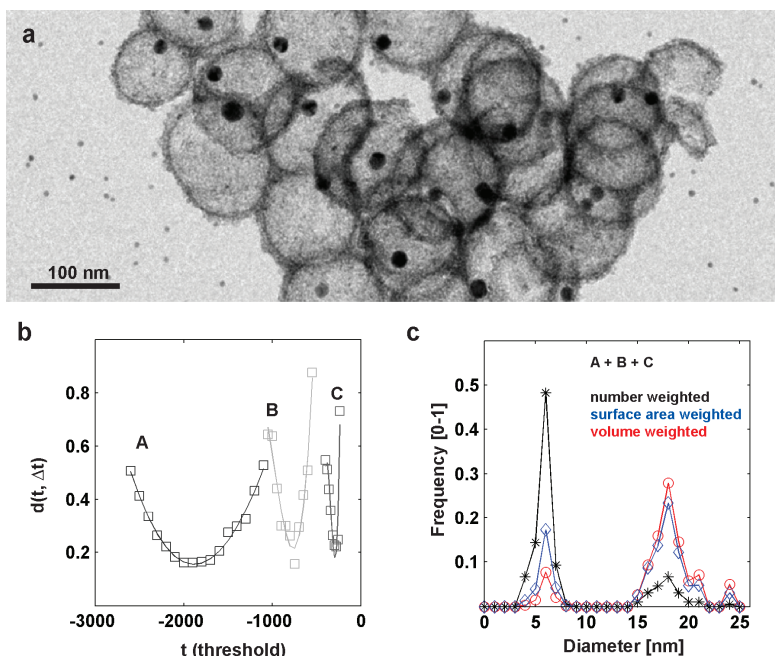


Figure 13 Quantitative analysis of the Au particles in the Au@ ZrO_2 catalyst showing TEM image (a), threshold criterion (b), and PSD of 189 Au particles including the 6 nm fiducial markers (c).

Third, the porous zirconia was split into convex segments using a combination of the Euclidean distance transform and the watershed algorithm.⁵⁰⁻⁵² Fourth, the PSDs of the individual segments were calculated. The results of this analysis are displayed in Figure 14. For all four investigated sub-volumes the threshold criterion (Figure 14c,e) showed minima. The size distribution of convex segments (Figure 14d,f) calculated from the two different reconstructions (B, C) matched remarkably well.

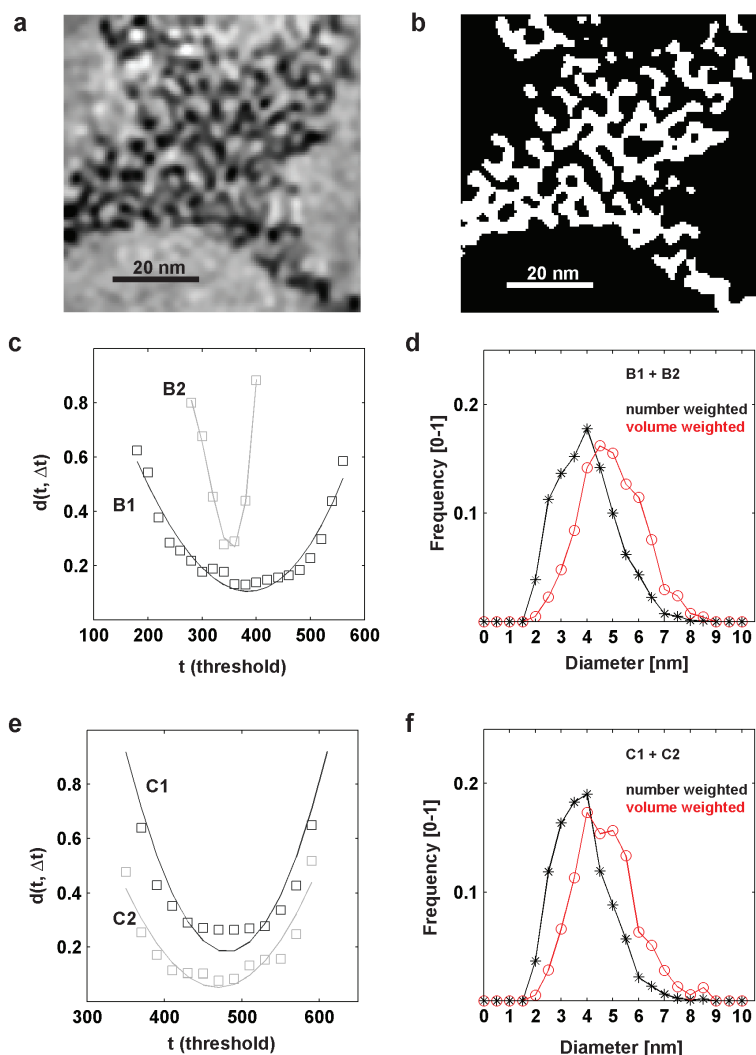


Figure 14 Quantitative analysis of zirconia shell showing numerical cross-section through reconstruction B sub-volume 1 (a), binarized cross-section (b), threshold criterion (c,e), PSD of 1698 ZrO_2 particles in contained in reconstruction B sub-volumes 1 and 2 (d), and PSD of 1363 ZrO_2 particles contained in reconstruction C sub-volumes 1 and 2 (f).

For the zirconia, the uncertainty in finding the curve minimum (± 75 gray levels) caused a modest broadening of the distribution curve. However, the separation step into convex segments restricts a direct interpretation in terms of accuracy as in the case of the metal particles. Our ET derived results are in good agreement with earlier TEM studies that estimated the size of zirconia segments to less than 10 nm.⁴⁰ An independent measurement of the zirconia crystal domain size was obtained by X-ray diffraction (Figure 15). From the width of the (011) ZrO_2 diffraction peak a crystal domain size of 4.5 nm was found which accurately matches the volume-weighted distribution maximum from ET. For the gold the width of the (111) peak indicated a domain size of 10.5 nm. This result significantly underestimates the ET derived particle size due to the presence of multiple crystalline domains within one gold particle as is frequently observed by TEM.⁵³

This study concludes with Figure 16 which illustrates additional characteristics of the zirconias 3D morphology. The TEM image (Figure 16a) shows an overview and is complemented by ET results (Figure 16b) that depict the porous nature of the zirconia shell composed of many crystallites. The zirconia shells had an approximate thickness of 10 nm with the thinnest regions observed at the contact points between neighboring spheres. Two examples of the interfaces between neighboring zirconia spheres are displayed in Figure 16c,d. While in some instances a hole at the contact point was observed (Figure 16c), in most cases the zirconia shells were complete (Figure 16d). The presence of holes suggests that the silica coated Au colloid partially agglomerated during sample preparation, thus preventing formation of the zirconia shell in these contact points. This is also supported by the Au PSD showing some particles larger than 18 nm, which may have formed by coalescence of the gold colloids from two neighboring zirconia spheres.

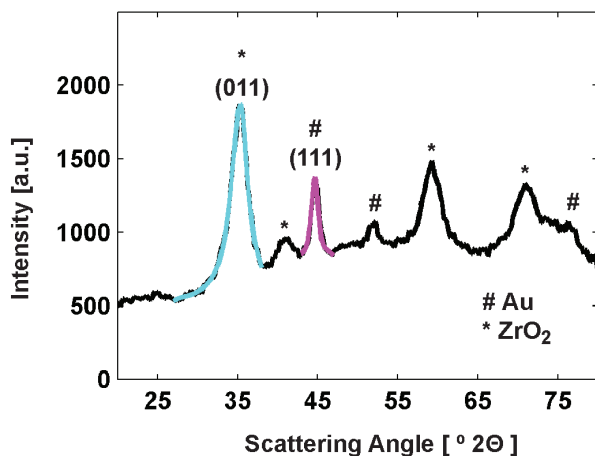


Figure 15 X-ray diffraction pattern of the Au@ZrO_2 system with fitted (011) ZrO_2 peak (blue) and (111) Au peak (magenta) to determine the crystal domain size.

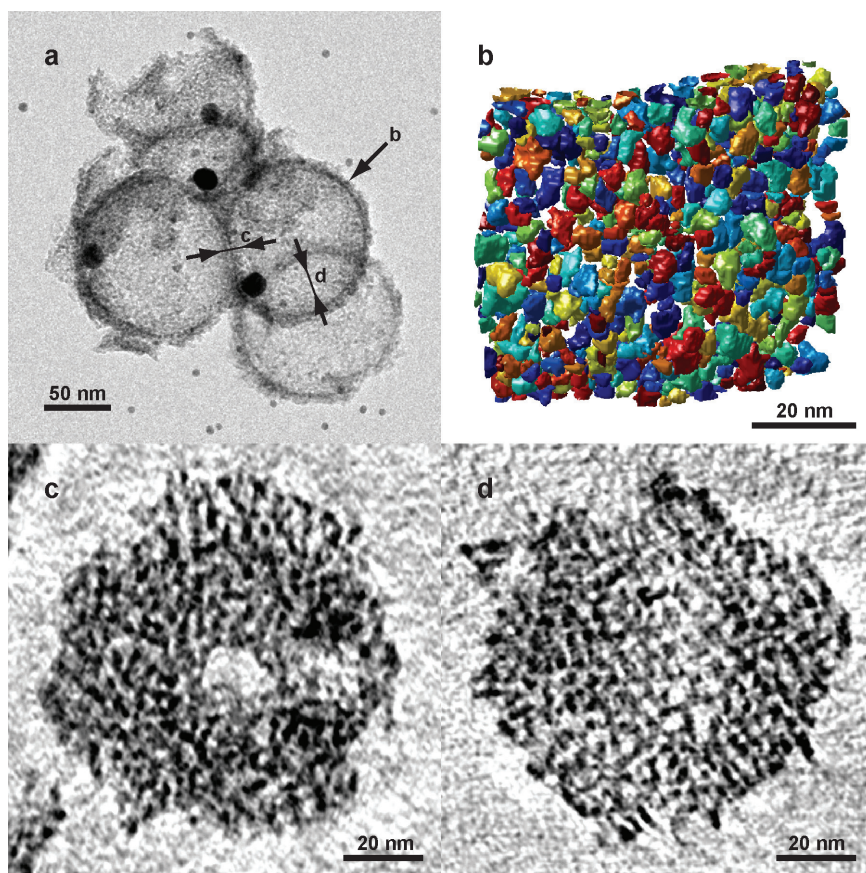


Figure 16 TEM image of the Au@ZrO₂ catalyst (a), surface representation of zirconia shell with individual crystallites displayed in different colors (b), numerical cross-section parallel to interface between two neighboring zirconia spheres with hole at the contact point (c), and complete shell (d).

5.5 Conclusions

ET has become an indispensable tool for the local 3D characterization of nanostructured catalysts. Particularly the potential to extract quantitative 3D information, e.g. by threshold-based segmentation of electron tomograms, can aid in understanding of the materials physico-chemical properties. Manual adjustment of the threshold based on visual inspection, which is likely to give different results at different times or by different operators (Figure 1), can be misleading and therefore automated, operator-independent procedures should be used instead. We propose a threshold criterion that is based on a combination of edge detection and single value thresholding. Its suitability to detect objects as small as 1 nm and measure their volume and surface area was validated in experiments on a colloidal gold model system and in simulations. Uncertainties in finding the minima of the criterion curve, i.e. the appropriate segmentation threshold, had no significant effect on the resulting particle size distributions. For the Ru/CNT catalyst a small difference in the PSD depending on the location of the particle with respect to the nanotube, i.e. inside (1-4 nm) or outside (1-3 nm), was observed. ET showed that 80 wt% of the ruthenium was deposited inside the tube at a local loading of 3.2 wt%. For the Au@ZrO₂ system mainly 18 nm Au particles were present within close to spherical zirconia shells. The shell was composed of on average 5 nm sized zirconia segments in line with the crystal domain size obtained from XRD line broadening. Moreover, the shell thickness (~ 10 nm) decreased in contact points between neighboring spheres, sometimes forming holes. In summary, we have shown a method for automated and operator-independent quantification of nanostructured catalysts which will in the future contribute to a more rational design of this important class of materials.

Acknowledgements

I would like to thank my collaborators Michael Paul and Ferdi Schüth (MPI Mühlheim, Germany) for the fascinating Au@zirconia catalyst, and Shujing Guo, Xiulian Pan and Xinhe Bao (DICP Dalian, P. R. China) for the very intriguing Ru/CNT system. Microscopy was performed at the Electron Microscopy group Utrecht (EMU) acknowledging W. J. C. Geerts, J. D. Meeldijk, T. P. van der Krift, M. N. Lebbink, N. Jimenez-Gil, E. van Donselaar, and C. Schneijdenberg for their support. I also would like to thank Bernd Rieger (Delft University of Technology) for reading of the manuscript and critical comments.

References

- (1) Janssen, A. H.; Koster, A. J.; de Jong, K. P. *Angew. Chem. Int. Ed.* **2001**, *40*, 1102.
- (2) Weyland, M.; Midgley, P. A.; Thomas, J. M. *J. Phys. Chem. B* **2001**, *105*, 7882.
- (3) Arslan, I.; Yates, T. J. V.; Browning, N. D.; Midgley, P. A. *Science* **2005**, *309*, 2195.
- (4) Gommès, C. J.; de Jong, K.; Pirard, J. P.; Blacher, S. *Langmuir* **2005**, *21*, 12378.

- (5) de Jong, K. P.; van den Oetelaar, L. C. A.; Vogt, E. T. C.; Eijsbouts, S.; Koster, A. J.; Friedrich, H.; de Jongh, P. E. *J. Phys. Chem. B* **2006**, *110*, 10209.
- (6) Adachi, K.; Chung, S. H.; Friedrich, H.; Buseck, P. R. *J. Geophys. Res. D: Atmos.* **2007**, *112*, D14202.
- (7) Friedrich, H.; Sietsma, J. R. A.; de Jongh, P. E.; Verkleij, A. J.; de Jong, K. P. *J. Am. Chem. Soc.* **2007**, *129*, 10249.
- (8) Ersen, O.; Werckmann, J.; Houille, M.; Ledoux, M. J.; Pham-Huu, C. *Nano Lett.* **2007**, *7*, 1898.
- (9) Koster, A. J.; Grimm, R.; Typke, D.; Hegerl, R.; Stoschek, A.; Walz, J.; Baumeister, W. *J. Struct. Biol.* **1997**, *120*, 276.
- (10) McIntosh, R.; Nicastro, D.; Mastronarde, D. *Trends Cell Biol.* **2005**, *15*, 43.
- (11) Midgley, P. A.; Weyland, M.; Thomas, J. M.; Johnson, B. F. G. *Chem. Commun.* **2001**, 907.
- (12) Möbus, G.; Inkson, B. J. *Mater. Today* **2007**, *10*, 18.
- (13) Friedrich, H.; de Jongh, P. E.; Verkleij, A. J.; de Jong, K. P. *Chem. Rev.* **2009**, DOI: 10.1021/cr800434t.
- (14) Bell, A. T. *Science* **2003**, *299*, 1688.
- (15) de Jong, K. P. *Curr. Opin. Solid State Mater. Sci.* **1999**, *4*, 55.
- (16) Schlögl, R.; Abd Hamid, S. B. *Angew. Chem. Int. Ed.* **2004**, *43*, 1628.
- (17) Weyland, M. *Top. Catal.* **2002**, *21*, 175.
- (18) Janssen, A. H.; Schmidt, I.; Jacobsen, C. J. H.; Koster, A. J.; de Jong, K. P. *Microporous Mesoporous Mater.* **2003**, *65*, 59.
- (19) Martinez, M. U.; Yeong, E.; Persin, M.; Larbot, A.; Voorhout, W. F.; Kubel, C. K. U.; Kooyman, P.; Prouzet, E. C. R. *Chim.* **2005**, *8*, 627.
- (20) Sietsma, J. R. A.; Friedrich, H.; Broersma, A.; Versluijs-Helder, M.; van Dillen, A. J.; de Jongh, P. E.; de Jong, K. P. *J. Catal.* **2008**, *260*, 227.
- (21) Ziese, U.; Gommès, C. J.; Blacher, S.; Janssen, A. H.; Koster, A. J.; de Jong, K. P. *Stud. Surf. Sci. Catal.* **2005**, *158*, 633.
- (22) Gommès, C. J.; Friedrich, H.; Wolters, M.; de Jongh, P. E.; de Jong, K. P. *Chem. Mater.* **2009**, *21*, 1311.
- (23) Bohm, J.; Frangakis, A. S.; Hegerl, R.; Nickell, S.; Typke, D.; Baumeister, W. *Proc. Nat. Acad. Sci. U.S.A.* **2000**, *97*, 14245.
- (24) Frangakis, A. S.; Bohm, J.; Forster, F.; Nickell, S.; Nicastro, D.; Typke, D.; Hegerl, R.; Baumeister, W. *Proc. Nat. Acad. Sci. U.S.A.* **2002**, *99*, 14153.
- (25) Pal, N. R.; Pal, S. K. *Pattern Recognit.* **1993**, *26*, 1277.
- (26) Ersen, O.; Hirlimann, C.; Drillon, A.; Werckmann, J.; Tihay, F.; Pham-Huu, C.; Crucifix, C.; Schultz, P. *Solid State Sci.* **2007**, *9*, 1088.
- (27) Midgley, P. A.; Thomas, J. M.; Laffont, L.; Weyland, M.; Raja, R.; Johnson, B. F. G.; Khimyak, T. J. *Phys. Chem. B* **2004**, *108*, 4590.
- (28) Ward, E. P. W.; Yates, T. J. V.; Fernandez, J. J.; Vaughan, D. E. W.; Midgley, P. A. *J. Phys. Chem. C* **2007**, *111*, 11501.
- (29) Arslan, L.; Walmsley, J. C.; Rytter, E.; Bergene, E.; Midgley, P. A. *J. Am. Chem. Soc.* **2008**, *130*, 5716.
- (30) Russ, J. C. *The image processing handbook*; 5th ed.; CRC Press, Taylor and Francis Group: Boca Raton, Florida, 2007.
- (31) Ohser, J.; Schladitz, K. Visualization, Processing and Analysis of Tomographic Data. In *Advanced Tomographic Methods in Materials Research and Engineering* Banhard, J., Ed.; Oxford University Press: Oxford, 2008; p37.
- (32) Bezemer, G. L.; Bitter, J. H.; Kuipers, H. P. C. E.; Oosterbeek, H.; Holeywijn, J. E.; Xu, X. D.; Kapteijn, F.; van Dillen, A. J.; de Jong, K. P. *J. Am. Chem. Soc.* **2006**, *128*, 3956.

- (33) Sahoo, P. K.; Soltani, S.; Wong, A. K. C.; Chen, Y. C. *Comput. Vision Graphics & Image Process.* **1988**, *41*, 233.
- (34) Ridler, T.; Calvard, S. *IEEE Trans. Syst. Man Cybern.* **1978**, *8*, 629.
- (35) Otsu, N. *IEEE Trans. Syst. Man Cybern.* **1979**, *9*, 62.
- (36) Zack, G. W.; Rogers, W. E.; Latt, S. A. *J. Histochem. Cytochem.* **1977**, *25*, 741.
- (37) Verschoor, A.; Frank, J.; Radermacher, M.; Wagenknecht, T. *J. Mol. Biol.* **1984**, *178*, 677.
- (38) Verbeek, P. W.; Vanvliet, L. J. *IEEE Trans. Pattern Anal. Mach. Intell.* **1994**, *16*, 726.
- (39) Castaldo, V.; Hagen, C. W.; Rieger, B.; Kruit, P. *J. Vac. Sci. Technol., B* **2008**, *26*, 2107.
- (40) Arnal, P. M.; Comotti, M.; Schüth, F. *Angew. Chem. Int. Ed.* **2006**, *45*, 8224.
- (41) Pan, X. L.; Fan, Z. L.; Chen, W.; Ding, Y. J.; Luo, H. Y.; Bao, X. H. *Nat. Mater.* **2007**, *6*, 507.
- (42) Chen, W.; Fan, Z. L.; Pan, X. L.; Bao, X. H. *J. Am. Chem. Soc.* **2008**, *130*, 9414.
- (43) Wang, C. F.; Guo, S. J.; Pan, X. L.; Chen, W.; Bao, X. H. *J. Mater. Chem.* **2008**, *18*, 5782.
- (44) Slot, J. W.; Geuze, H. J. *Nat. Protoc.* **2007**, *2*, 2480.
- (45) Kremer, J. R.; Mastronarde, D. N.; McIntosh, J. R. *J. Struct. Biol.* **1996**, *116*, 71.
- (46) Nickell, S.; Forster, F.; Linaroudis, A.; Net, W. D.; Beck, F.; Hegerl, R.; Baumeister, W.; Plitzko, J. M. *J. Struct. Biol.* **2005**, *149*, 227.
- (47) Reimer, L. *Transmission Electron Microscopy*; 4th ed.; Springer-Verlag: Berlin, 1997.
- (48) Cha, J. J.; Weyland, M.; Briere, J. F.; Daykov, I. P.; Arias, T. A.; Muller, D. A. *Nano Lett.* **2007**, *7*, 3770.
- (49) Frangakis, A. S.; Hegerl, R. *J. Struct. Biol.* **2001**, *135*, 239.
- (50) Friedman, J. H.; Bentley, J. L.; Finkel, R. A. *ACM Trans. Math. Software* **1997**, *3*, 209.
- (51) Russ, J. C.; Russ, J. C. *Acta Stereol.* **1988**, *7*, 33.
- (52) Vincent, L.; Soille, P. *IEEE Trans. Pattern Anal. Mach. Intell.* **1991**, *13*, 583.
- (53) Johnson, C. L.; Snoeck, E.; Ezcurdia, M.; Rodriguez-Gonzalez, B.; Pastoriza-Santos, I.; Liz-Marzan, L. M.; Hytch, M. J. *Nat. Mater.* **2008**, *7*, 120.

Chapter 6

Quantitative Structural Analysis of Binary Nanocrystal Superlattices by Electron Tomography

Abstract

Binary nanocrystal superlattices, i.e. ordered structures of two sorts of nanocolloids, hold promise for a series of functional materials with novel collective properties. Here we show that based on electron tomography a comprehensive, quantitative, 3D characterization of these systems down to the single nanocrystal level can be achieved, key in understanding the emerging materials properties. On four binary lattices composed of PbSe, CdSe, and Au nanocrystals we illustrate that ambiguous interpretations based on 2D TEM can be prevented, nanocrystal sizes and superlattice parameters accurately determined, individual crystallographic point and plane defects studied, and the order/disorder at the top and bottom surfaces imaged. Furthermore, our results suggest that superlattice nucleation and growth occurred at the suspension/air interface and that the unit cells of some lattices are anisotropically deformed upon drying.

Adapted with permission from H. Friedrich, C. J. Gommès, K. Overgaag, J. D. Meeldijk, W. H. Evers, B. de Nijs, M. P. Boneschanscher, P. E. de Jongh, A. J. Verkleij, K. P. de Jong, A. van Blaaderen, D. Vanmaekelbergh, *Quantitative structural analysis of Binary Nanocrystal Superlattices by Electron Tomography*. Nano Letters **2009**, DOI: 10.1021/nl901212m. Copyright 2009 American Chemical Society.

6.1 Introduction

Bottom-up assembly of prefabricated building blocks into large, ordered structures by lowering of the free energy is a concept shared across several disciplines, from biology, supra-molecular chemistry to the crystallization of microcolloids. Particles in the nanometer size range are of special interest, as they bridge the worlds of molecular and micro-colloidal self-organization. In addition, the nanometer dimension crosses a number of natural physical length scales resulting in properties that strongly depend on the nanocrystal (NC) size and shape. For instance, semiconductor NCs show a discrete electronic structure and size-tunable opto-electrical properties on account of quantum confinement.¹

Crystallization of nanocolloids has led to a plethora of single-component and, more recently, binary superlattices of striking structural diversity, long-range order and beauty.²⁻⁷ Particularly binary nanocrystal superlattices, i.e. ordered structures of two sorts of nanocolloids that are metallic, insulating, semiconducting or magnetic in nature, hold promise for a series of novel materials with thermo-, magneto- or opto-electric applications.⁷⁻⁹ The special potential of binary systems, in which one type of NC is in close contact with another, lies in the interactions between the building blocks that can induce novel collective properties. A striking example has been published recently: NCs that are inherently insulating, when assembled in a binary superlattice, led to a material with strongly enhanced conductivity.⁷ From the evident analogy with atomically doped semiconductors like silicon, it is clear that such emerging material properties depend critically on the overall superlattice geometry, the distances between the NCs, and the density and nature of defects. Moreover, an understanding of the formation mechanism and control over the driving force(s), which is mainly lacking, requires a full 3D characterization of the binary superlattice structure, including its defects.

Techniques that analyze the spatial Fourier transform of a real space structure such as (small-angle) X-ray diffraction¹⁰ and electron crystallography¹¹ have proven to elucidate the average crystal lattice accurately. However, a drawback of these methods is that local, spatially resolved information cannot be obtained, which makes them not suitable for the study of superlattice boundaries and defects. In contrast, electron tomography, which has been employed in structural biology^{12,13} for many years and more recently in materials science^{14,15}, can provide local, spatially resolved information on the nanoscale and in 3D. Here, we show that ET^{16,17} can be extended to a comprehensive structural analysis of binary NC superlattices by quantifying individual NC coordinates, sizes, unit cell parameters and, furthermore, characterizing point and plane defects.

6.2 Experimental

Sample preparation. Four binary superlattices of AB_2 and AB_{13} stoichiometry (PbSe and CdSe NCs) and of AB_2 and AB stoichiometry (PbSe and Au NCs) were prepared as previously published.^{5,18-20} In short: mixed suspensions of trioctylphosphine oxide (TOPO)/hexadecylamine (HDA) capped CdSe and oleic acid (OA) capped PbSe nanocrystals (NCs) were prepared in tetrachloroethylene (TCE), while suspensions of dodecanethiol capped gold NCs and OA capped PbSe NCs were prepared in toluene in a oxygen and water free environment. By varying the NC concentrations in suspension different binary superlattices could be prepared. Colloidal crystallization proceeded by evaporating the solvent under reduced pressure (~ 10 mbar) at 70°C with the substrate kept at an angle of 30° to the horizontal. Carbon coated formvar films supported on Cu TEM grids were used as substrates. PbSe/CdSe NC structures of AB_2 and AB_{13} stoichiometry were mainly formed at a $c_{\text{CdSe}}/c_{\text{PbSe}}$ of 5 and 12, respectively.^{5,18} PbSe/Au structures of AB and AB_2 stoichiometry were formed at a $c_{\text{Au}}/c_{\text{PbSe}}$ ratio between 1 and 5.¹⁹ The particle concentration ratios were determined from absorption measurements.^{18,20-22}

Characterization. Electron tomography was performed in bright-field mode using a Tecnai 20 electron microscope with a LaB_6 electron source (FEI Company, Eindhoven). Images of the tilt-series were acquired over an angular range of $\pm 70^\circ$ at 2° increments on a Tietz $2k \times 2k$ CCD camera (TVIPS GmbH, Gauting) using Inspect3D software (FEI Company, Eindhoven). The nominal magnification was $29000\times$ corresponding to a pixel size of 0.27 nm . The defocus was set to -200 to -300 nm (nominal) to keep the entire object in underfocus throughout the tilt-series and an objective aperture of $40\ \mu\text{m}$ was inserted in the beam path. Images of the tilt-series were aligned with respect to a common origin and rotation axis using the PbSe or Au particles as fiducial markers. The aligned tilt-series was binned to 0.54 nm pixel size which is approximately the interpretable resolution at the experimental imaging conditions prior to reconstruction of the three dimensional volume (see also section 5.3, page 85). An example is provided in the supporting information (SI movie1) showing an aligned tilt series of the AB_{13} lattice acquired over an angular range of $\pm 70^\circ$ at 2° increments. The corresponding reconstruction of the AB_{13} lattice is displayed in SI movie2 by sequential numerical cross-sections parallel to the imaging plane at different heights. SI movie2 starts at the back side of the support film, moving upwards through the support film and the superlattice and then back downwards. Alignment and reconstruction by weighted backprojection was performed in IMOD.²³

The overall quantification of the electron tomograms encompassed two steps: (i) image analysis aiming at extracting the position and size of all nanoparticles in the reconstructed volume, and (ii) analysis of the particle positions and sizes in terms of lattice parameters, crystal structure and nearest neighbor distances. Structure and image analysis were carried out in Matlab 7.4 (The MathWorks, Inc.).

6.3 Image analysis

Image analysis proceeded in three steps. First, the position of all particles was obtained by template matching.^{24,25} Templates were defined as spherical dark regions (of value -1), surrounded by a bright shell (of value +1). This template model corresponds well with the appearance of the NC in the tomogram exposing dark cores and a bright rim. The bright rim results from underfocus condition during acquisition as well as the reconstruction point spread function. Templates were normalized so that the sum of all intensities in the template is zero. Normalization ensures a response of zero in a region of uniform intensity. The criterion for particle detection is a correlation larger than 0.5 between template and reconstruction.²⁶ To account for dispersion in the particle size distribution templates of variable size were employed. The centroids of the correlation peaks (> 0.5) are considered as the position of the particle. In the second step of image analysis the radius of the particles was determined. For each particle, the image intensity was radially averaged over the three horizontal slices closest to the particle center. The radial intensity average shows a distinct edge-like profile, going from low values in the center region (dark core) and increasing dramatically to high values in the shell region (bright rim). The radius of the particle is determined as the radial distance at which the intensity is exactly halfway between the minimum and maximum.²⁷ The third and final step of image analysis removed false positives. Four independent criteria were applied based on contrast, average intensity, size, and position to ensure proper detection for both NC classes independently. The presented methodology enabled us to characterize thousands of NC in each tomogram containing less than 5 % false positives for high-contrast PbSe and Au NC and around 10% false positives for the low-contrast CdSe NC. We estimate that, overall, approximately 90 % of the NCs were detected.

6.4 Structure analysis

While image analysis provided the position and radius of the individual NC in the reconstruction, this section deals with extracting the crystal structure from the data. To detect local variations, structure analysis was performed on multiple sub-regions of the tomogram as indicated in Figure 1. In a step preceding structure analysis, NC core diameters (d_{core}) were fitted assuming a Gaussian spread. In addition, the average soft shell thickness was calculated by subtracting the two NC core radii from their respective distance. The values presented in the Appendix on pages 130-133, Tables 1 to 4, take either the minimum soft shell thickness (t_{min} , nearest neighbour only) or an average over the three smallest soft shell thicknesses ($t_{3\text{NN}}$, three nearest neighbours) into account. Structure analysis included four successive steps, as explained in the following sub-sections.

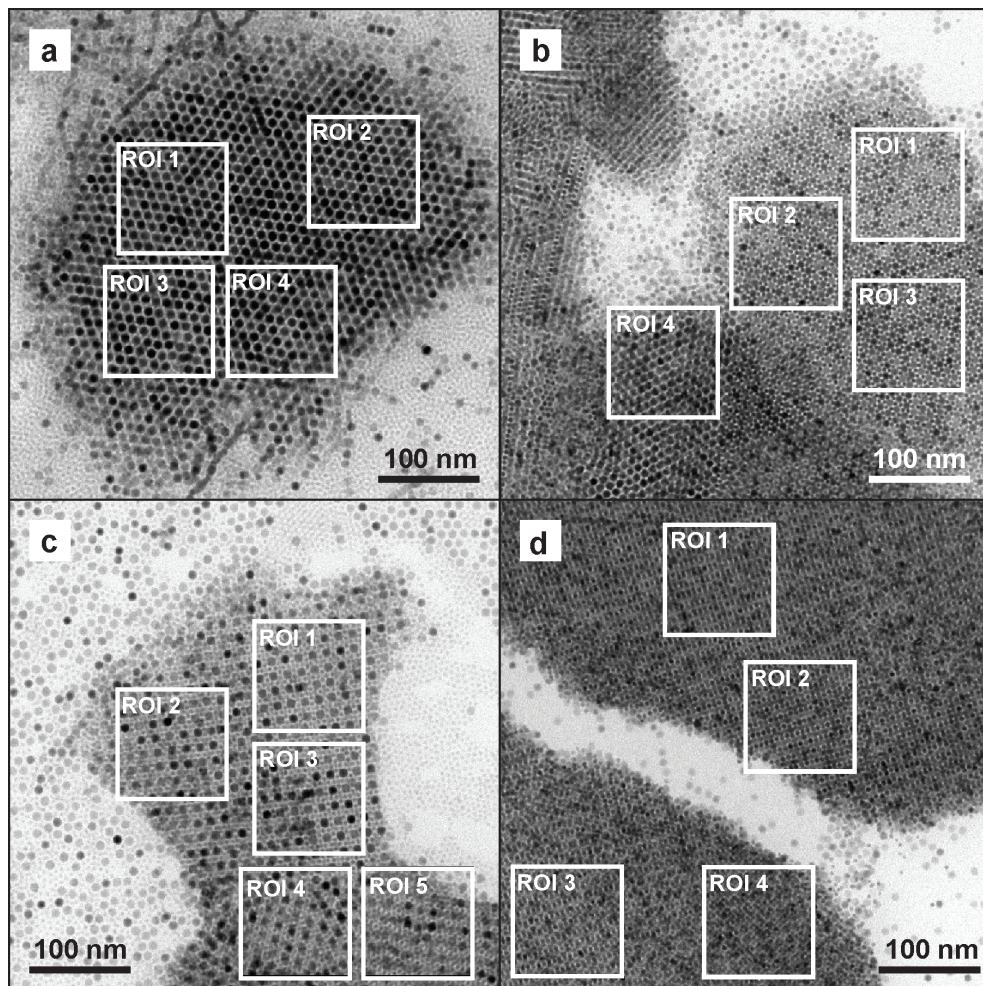


Figure 1. TEM images of examined superlattices at zero tilt and regions of interest (ROI) which were analyzed in terms of particle size, soft shell thickness, unit cell vectors and angles, and underlying crystallographic lattice. AB₂ lattice consisting of PbSe and CdSe NCs (a), AB₂ lattice consisting of PbSe and Au NCs (b), AB₁₃ lattice consisting of PbSe and CdSe NCs (c), and AB lattice consisting of PbSe and Au NCs (d).

6.4.1 Detection of crystalline clusters of particles

First, a 3-dimensional Voronoi tessellation is performed on the PbSe NC data in order to detect which particles are first neighbors to each other. The Voronoi tessellation divides space into cells defined as the locus of all points closer to a given particle than to any other. Two particles are then said to be neighbors if their Voronoi cells touch each other. Following other studies^{21,23}, the rotational symmetry of the configuration of closest neighbors to any particle is quantified using spherical harmonics with $l = 6$. For any particle i , we calculate

$$q_{6m}(i) = \frac{1}{B} \sum_{n=1}^{N_i} Y_{6m}(\hat{r}_{in}) \quad (1)$$

where \hat{r}_{in} is the unit vector pointing from particle i to its n th neighbor, N_i is the number of neighbors to particle i , Y_{6m} are the spherical harmonics with $l = 6$, and B is normalizing constant chosen so that:

$$\sum_{m=-6}^6 q_{6m}^*(i) q_{6m}(i) = 1$$

The rotational invariant Q_6 is calculated for each particle as

$$Q_6(i) = \sqrt{\frac{4\pi}{13} \sum_{m=-6}^6 |q_{6m}(i)|^2} \quad (2)$$

serving as a measure of the crystallinity around particle i . The particle having the largest value of Q_6 is found, corresponding to number i_{\max} .

To find the set of other particles that belong to same crystallite as particle i_{\max} , we calculate the complex inner product

$$C_q(i_{\max}, j) = \sum_{m=-6}^{+6} q_{6m}(i_{\max}) q_{6m}^*(j) \quad (3)$$

which is an objective measure of the similarity in rotational symmetry around particle j and particle i_{\max} . The crystallite containing particle i_{\max} is defined as the set of all touching particles with $C_q(i_{\max}, j) > 0.5$. As $C_q(i_{\max}, i_{\max}) = 1$, because of the normalization constant B in Equation 1, this cluster of particles necessarily contains i_{\max} .

6.4.2 Determination of the crystallite lattice parameters

When the detected crystalline cluster contains more than 50 particles, its structure is analyzed as follows. The crystalline cluster generally contains some holes, meaning that some of its particles are not detected. Before analyzing the structure, the holes have to be filled. For that purpose, letting \mathbf{x}_n be the 3-dimensionnal positions of the particles in the cluster, the function $F(\mathbf{x})$ is defined as

$$F(\mathbf{x}) = \sum_{c=1}^N \sum_{n=1}^N G_{\sigma}(\|\mathbf{x} - (\mathbf{x}_n - \mathbf{x}_c)\|) \quad (4)$$

where G_{σ} is a Gaussian with standard deviation σ . Equation 4 takes successively every particle of the cluster as the origin (sum over index c), and it creates a Gaussian function centered on the position of all other particles (sum over n) with respect to particle c . The maxima of function F are therefore expected to have the same translational symmetry as the cluster, with the gaps filled. Another advantage of using Equation 4 is that no particle is given a preferential role in the analysis. In practice, σ is chosen equal to the average particle radius.

On basis of function F the crystal structure is determined. Let $x(n)$, $y(n)$ and $z(n)$ be the coordinates of the n^{th} maximum of function $F(\mathbf{x} = [x, y, z])$. The relation between the lattice base vectors (\mathbf{a} , \mathbf{b} , \mathbf{c}) and the positions of the lattice points can be written in the matrix form

$$\begin{pmatrix} x(1) & y(1) & z(1) \\ \vdots & \vdots & \vdots \\ x(N) & y(N) & z(N) \end{pmatrix} = \begin{pmatrix} 1 & K(1) & L(1) & M(1) \\ \vdots & \vdots & \vdots & \vdots \\ 1 & K(n) & L(n) & M(n) \end{pmatrix} \begin{pmatrix} x_0 & y_0 & z_0 \\ a_x & a_y & a_z \\ b_x & b_y & b_z \\ b_x & c_y & c_z \end{pmatrix} \quad (5)$$

where $K(n)$, $L(n)$, $M(n)$ are the lattice indices, and (x_0, y_0, z_0) is the position of the origin. If the indices were known, Equation 5 would be a linear over-determined system, which could be solved in the least-square sense for the base vectors and the position of the origin. The problem is solved in two steps. First, the position of the 3 maxima of $F(\mathbf{x})$ which are the closest to $\mathbf{x} = 0$ are chosen as a first guess of the base vectors. After defining a suitable lattice based on linear combinations of the ‘guess’ base vectors, the indices K , L , M of each particle are calculated. Second, using these indices, Equation 5 is solved in the least-square sense to provide the final value of the base vectors.

6.4.3 Completing the crystallites based on its lattice parameters

Once the lattice parameters of a crystallite are known, the expected positions of all particles belonging to it is calculated from Equation 5, with K, L, M taking all possible integer values. The initial crystalline cluster considered in section 1 is then grown progressively, by adding one by one any particle that touches and that is close enough to a lattice node. At this stage, all particles that have already been assigned to a given crystallite are excluded from further analysis and step 1 is then repeated, starting from the remaining particle with the largest value of Q_6 to find additional crystalline regions.

The length and relative angles of the lattice vectors in the examined systems are provided in the Appendix on page 130-133, Tables 1 to 4. Subsequently, the unit cell filling fractions and NC size ratios were calculated based on particle size, soft shell thickness, unit cell vector length. These results, also shown in the Appendix on page 130-133 in Tables 1 to 4, illustrate that filling fractions and particle size ratios vary dramatically between the hard core and the different hard core plus soft shell approximations.

6.4.4 Statistical analysis of the unit cell

Based on the PbSe lattice points and vectors belonging to individual crystalline regions additional NC (CdSe, Au, PbSe) within the unit cell (UC) were analyzed with respect to their average position. Since not all NC within the lattice could be detected the statistical analysis was performed on arrangements having 7-8 PbSe NC in the eight corners of the UC and 1-2 CdSe or Au for AB_2 , 12-13 CdSe for AB_{13} and 3-4 Au + 1-2 PbSe for AB stoichiometries. The average lattice positions, for additional NC within the UC, were determined by k-means clustering and are listed in the Appendix on page 130-133, Tables 1 to 4. The fact that average crystallographic information can be provided independent of lattice contractions highlights again the versatility of the presented methodology.

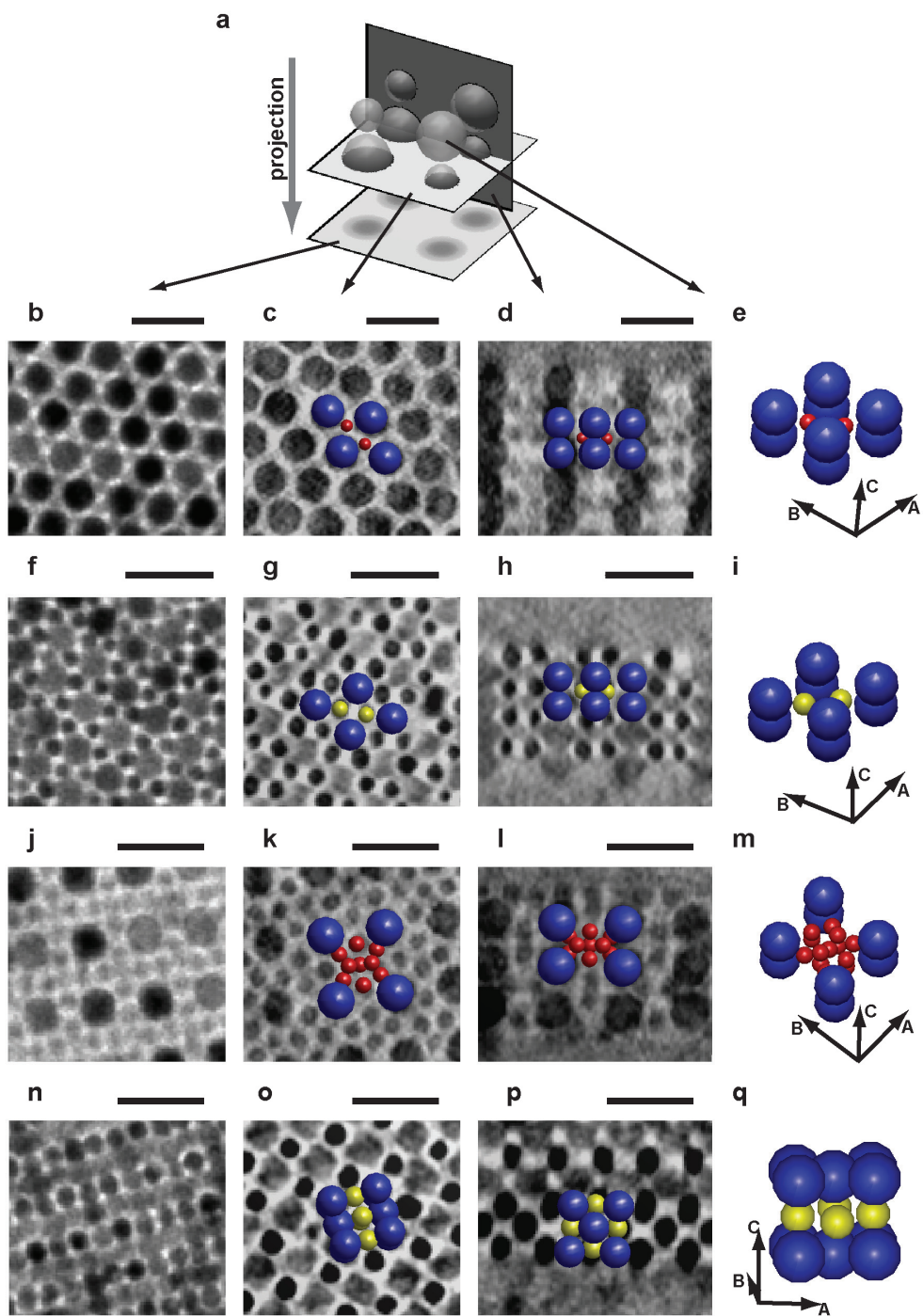
6.5 Results and Discussion

The crystallographic analysis of the AB_2 superlattice containing PbSe and CdSe NCs is summarized in Figure 2b-e. Please consult Figure 1a (page 105) and Table 1 (page 130) in the Appendix for more details. The lattice parameters varied less than 5 % between different sub-regions, NC core diameters were constant (9 nm PbSe; 3.4 nm CdSe), and a thickness of 4 to 5 unit cells was observed. The relative positions of the NCs in the unit cell confirmed ordering isostructural with AlB_2 (space group 191), however, with a strong contraction perpendicular to the substrate plane (C-vector). While in the [001] plane (Figure 2c) the PbSe NC are well separated by the organic ligand shell, in the [1-10] plane (Figure 2d) no gap between the NC cores is visible. The absence of a visible gap in the [1-10] plane results from

a compression of the organic ligand shell perpendicular to the support and from blurring by the reconstruction point spread function. The reason for the strong anisotropic contraction will be discussed below in context of superlattice formation.

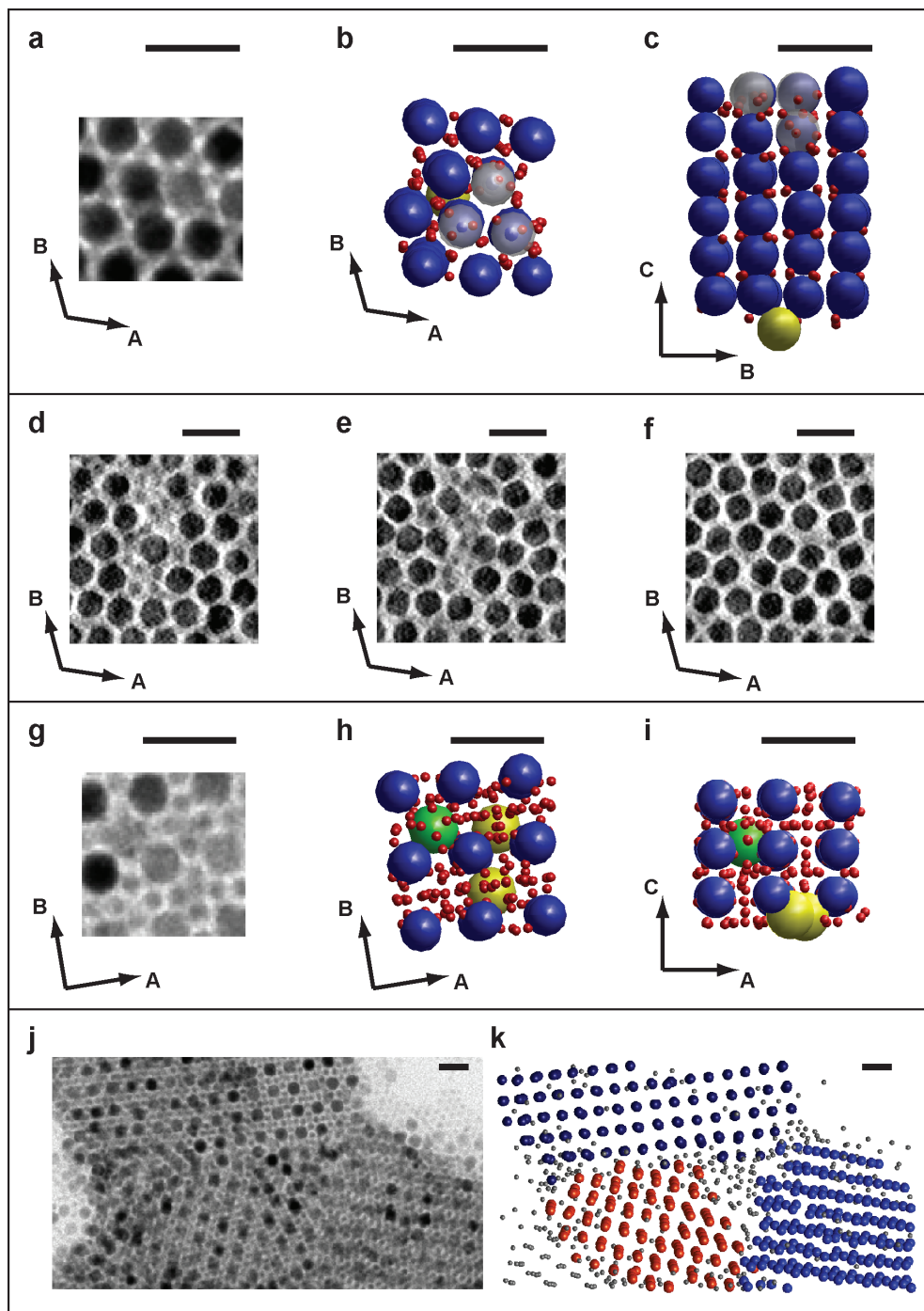
The crystallographic analysis of the second AB_2 lattice (7.1 nm PbSe; 3.7 nm Au; thickness 2 to 4 unit cells), likewise exposing $A1B_2$ ordering is displayed in Figure 2f-i. Additional details are presented in Figure 1b (page 105) and Table 2 (page 131) in the Appendix. Also in this case a strong contraction perpendicular to the substrate plane (C-vector) was detected. In some instances NC vacancies in the gold lattice (Figure 2g,h) or variations in crystal structure (Figure 1b, ROI4) were observed and are further discussed below in context of crystal defects.

Furthermore, we investigated lattices with AB_{13} stoichiometry (8.8 nm PbSe; 3.7 nm CdSe), which are most intriguing as two isomorphs exist. Previous TEM studies reported the occurrence of the cub-octahedral AB_{13} structure^{5,6}. Since this particular arrangement has a considerably lower filling fraction than the icosahedral AB_{13} isomorph, the suitability of the hard-sphere model²⁸ for the studied systems has been put into question. As in the previous reports, the TEM picture (Figure 2j) may equally give the impression that the structure is cub-octahedral. In contrast, the numerical cross-section (Figure 2k) reveals that the four CdSe closest to the [001] lattice plane do not form a square. Instead, the CdSe quadrangle is elongated in one direction, alternating by 90° degrees between neighboring cells. The numerical cross section displayed in Figure 2l slices through the PbSe and the two CdSe closest to the [010] lattice plane. The relative location of the CdSe NCs alternates by 90° between neighboring cells, as the CdSe are either being visible side by side or above each other. The observation of a 90° rotation in the CdSe arrangement between neighboring cells reveals without any doubt the icosahedral configuration. ET analysis of all other sub-regions (see Appendix Figure A.1 on page 134) shows that the densest AB_{13} structure, that is the icosahedral isomorph, prevails. A flawed analysis based on TEM images may arise from the complexity of the ico- AB_{13} lattice with a layer-wise rotation of the CdSe “cross motif” along the projection axis. The structure depicted in Figure 2j is one ico- AB_{13} unit cell thick (Figure 2l) which corresponds to the projection of two by 90° rotated cells. Analogous to the AB_2 examples, the AB_{13} lattices are strongly contracted perpendicular to the support resulting in a distance of 1-2 nm between the PbSe NC cores in this direction. More details are provided in Figure 1c (page 105) and Table 3 (page 132) in the Appendix.



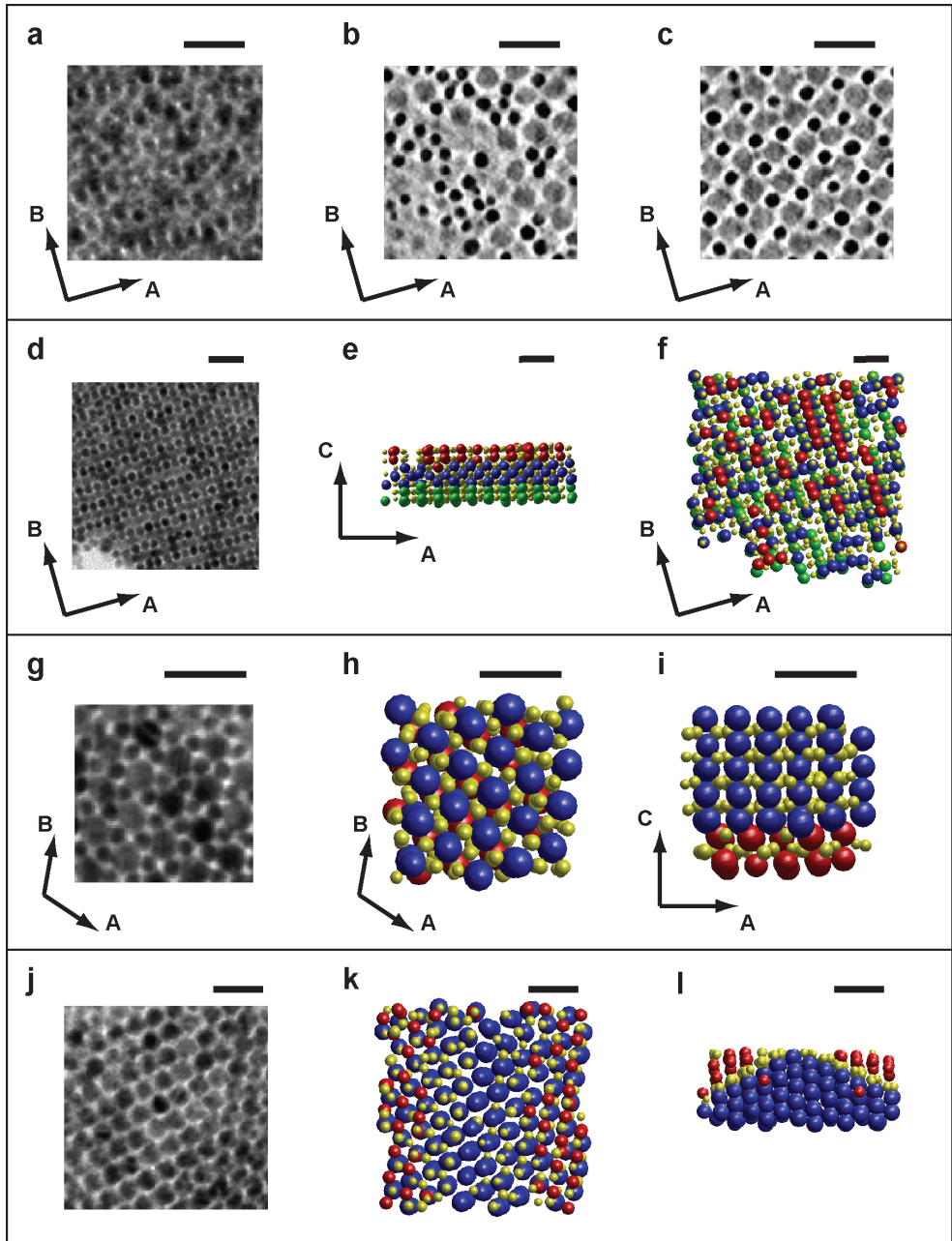
The last example presented in Figure 2n-q summarizes the crystallographic analysis of an AB superlattice formed by 6.9 nm PbSe and 4.6 nm Au NCs. Again, the TEM image (Figure 2n) is complex and prone to misinterpretation. The numerical cross-sections parallel (Figure 2o, [010] plane) and perpendicular (Figure 2p, [001] plane) to the support film illustrate that a superlattice isostructural with CuAu (space group 123) is present. The stacking of lattice planes perpendicular to the support film contains a 90 degree rotation between the first and second unit cell layer (Figure 2p), responsible for the complex TEM projection pattern. The examined AB superlattice was 2 to 3 unit cells thick. The lattice parameters did not vary by more than 4% between different regions. Strikingly, we find no contraction perpendicular to the support film as for the superlattices discussed above. Please refer to Figure 1d (page 105) and the Appendix, Table 4 on page 133, for additional information.

Figure 2. Crystallographic analysis of binary superlattices with AB₂, AB₁₃, and AB stoichiometry. (a) cartoon explaining the relationship between the panels below: TEM image (left), numerical cross-section through 3D reconstruction (3D intensity map) parallel to imaging plane (left center), numerical cross-section perpendicular to imaging plane (right center), and unit cell showing the nanocrystal cores with lattice vectors (right). AB₂ superlattice of 9 nm PbSe (blue) and 3.4 nm CdSe (red) NCs (b–e) with: TEM image along (001) direction at zero tilt (b), cross-section through [001] plane of PbSe NCs, the CdSe NCs are ½ unit cell higher (c), cross-section through [1-10] plane of PbSe and CdSe NCs (d), and AB₂ unit cell (e). AB₂ superlattice of 7.1 nm PbSe (blue) and 3.7 nm Au (yellow) NCs (f–i) with: TEM image along (001) direction at zero tilt (f), numerical cross-section parallel to [001] plane through Au NCs (g), cross-section parallel to [1-10] plane through PbSe and Au NCs (h), and AB₂ unit cell (i). ico-AB₁₃ superlattice of 8.8 nm PbSe (blue) and 3.8 nm CdSe (red) NCs (1/8th unit cell) with: TEM image along (001) direction at zero tilt (j), cross-section parallel to [001] plane through PbSe (dark gray) and four nearest CdSe (light gray) (k), cross-section parallel to [010] plane through PbSe and two nearest CdSe (l), and 1/8th of ico-AB₁₃ unit cell (m). AB superlattice of 6.8 nm PbSe (blue) and 4.6 nm Au (yellow) NCs (n–q) with: TEM image along (010) direction at zero tilt (n), cross-section through [010] plane of PbSe (dark gray) and Au (black) (o), cross-section through [001] plane of PbSe and Au NCs (p), and AB unit cell (q). Scale bars are 20 nm.



In NC superlattices, as in atomic crystals, entropy dictates and gives a lower bound on the number and types of crystallographic defects, such as NC vacancies and substitutions. Kinetic effects during the superlattice growth can, however, significantly increase their number. In Figure 3 we illustrate on superlattices of PbSe and CdSe NCs that ET is also extremely valuable to discern crystal defects. While the TEM image (Figure 3a) suggests a defect-free AB_2 superlattice, ET analysis (Figure 3b,c) revealed more than one crystallographic defect. In this case PbSe NC vacancies were occupied by multiple CdSe NCs and a surface-adsorbed PbSe NC was found between the superlattice and the support film. Figure 3d-f illustrates a disorder/order transitions between the first, second, and third PbSe layer from the surface of the superlattice. In Figure 3g-i examples of defects in an AB_{13} lattice are displayed. While the TEM image (Figure 3g) provides only limited insight, ET results (Figure 3h,i) clearly show that a PbSe NC had substituted multiple CdSe NCs and that two surface-adsorbed PbSe NC were present. Furthermore, multiple crystalline domains (Figure 3j,k) were resolved in the AB_{13} superlattice. From Figure 3j (lower part) it also becomes clear that TEM images are difficult to interpret if the electron beam direction does not coincide with a crystal axis.

Figure 3 Examples of defects in binary superlattices composed of PbSe and CdSe NCs. TEM image of AB_2 of PbSe and CdSe along (001) direction at zero tilt lattice (a), ET analysis showing PbSe (blue), CdSe (red), substituted PbSe (semitransparent white), and surface-adsorbed PbSe (yellow) (b,c). Numerical cross-sections (parallel to (001) direction) through PbSe NCs in AB_2 lattice showing first (d), second (e), and third (f) PbSe layer from surface. TEM image of AB_{13} superlattice along (001) direction at zero tilt (g), and ET analysis showing PbSe in blue, CdSe in red, intra-crystalline PbSe in green (substitution) and surface-adsorbed PbSe in yellow (h,i). Intergrowth of multiple AB_{13} crystallites showing TEM image at zero tilt (j), and ET analysis showing three PbSe lattices in black, blue, and orange (k). Scale bars are 20 nm.



TEM imaging of an underlying lattice can also be significantly obstructed by NCs randomly adsorbed on the top or bottom surfaces. This situation is exemplified in Figure 4a, presenting a TEM image that suggests a disordered NC film. ET slices reveal, however, that this is due to one layer of surface adsorbed NCs (Figure 4b) on the bottom of a defect-free AB superlattice (Figure 4c). Alternatively, electron diffraction or analysis of the TEM image by Fast Fourier Transform (Appendix, Figure A.2, page 135) will expose the underlying lattice periodicity but not the disordered layer as shown in Figure 4b. Besides point defects and order/disorder transitions, plane defects could also be inferred by ET. For example, Figure 4d-f display an AB lattice with grain boundaries parallel to the support surface which are characterized by the above mentioned rotation of the unit cell over 90 degrees from layer to layer. Likewise, in the AB₂ superlattice, composed of PbSe and Au NCs, a horizontal shift by half a unit cell (Figure 4g-i), and a partially demixed region (Figure 4j-l, ROI4 in Figure1b) were detected.

Figure 4 Examples of defects in binary superlattices composed of PbSe and Au NCs. TEM image of AB lattice along (001) direction at zero tilt (a), Numerical cross-sections through first Au NC layer from support (b), and through second Au NC layer from support (c). TEM image of AB lattice along (010) direction at zero tilt (d), and ET analysis showing PbSe belonging to different crystallites (layers) in red, blue, green and Au NC in yellow. TEM image of AB₂ lattice along (001) direction at zero tilt (g) and ET analysis with PbSe belonging to different crystallites in blue, red and Au in yellow (h,i). TEM image at zero tilt of demixed region, ROI 4 in Figure1b (j), and ET analysis showing PbSe pyramid in blue, additional PbSe in red and Au in yellow (k,l). Scale bars are 20 nm.

The discussion of crystal defects concludes with an example from an AB_2 structure composed of PbSe and Au NCs. Although invisible in the TEM image (Figure 5a) of the 2-3 unit cell thick specimen, the numerical cross-section (Figure 5b) and the corresponding ET analysis (Figure 5c) clearly reveal a substitutional defect. Contrary to the fact that a PbSe NC has been replaced by a smaller Au NC, the PbSe lattice appears to be stretched around the point defect. The magnitude of displacement for the PbSe NCs is represented in Figure 5c,e as a color change from blue (on lattice) to green (~ 2.5 nm of lattice). A larger overview of the same region is presented in Figure 5d,e with the substitution indicated by a red dot. From Figure 5e it is evident that the displacement becomes larger closer to the left and the bottom boundary of the displayed region which we attribute to an overall bending of the superlattice. One can envision that developments towards strain field mapping could bridge the gap between the 2D atomic²⁹ and 3D micro-colloidal³⁰ equivalent. Furthermore, quantifying defect densities by visual inspection (e.g. 3.6 % Au NC vacancies were found in the AB_2 lattice), or even better by automated routines, seems an obvious extension for the future.

Furthermore, being able to study the top and bottom surfaces by ET, can give important information regarding the nucleation and growth mechanism. Figure 6a-d shows a TEM image of the AB_{13} superlattice together with three numerical cross-sections perpendicular to the support film. The surface I on top of the cross-sections (Figure 6b-d) corresponds to the suspension/air interface, surface II to the suspension/support interface, and surface III to the opposing side of the TEM support film. It can be seen that interface I is mainly well ordered (Figure 6b-d), while interface II displays surface-adsorbed NCs (Figure 6c) and unfinished NC layers (Figure 6d). An unfinished layer means in this context that PbSe NCs are present in crystallographic positions in the fourth layer from the top while not all positions in the fourth layer are occupied by PbSe NCs. Similar observations can be made for AB_2 lattices (Figure 6e-h, Figure 7a-d) and AB lattices (Figure 7e-h, Figure 4a-c showing disorder order transition of the suspension/support interface). Additional material is provided in the Appendix, on pages 136-139, Figure A.3 to A.6, showing numerical cross-sections parallel to the three interfaces of each superlattice. Overall, the suspension/air interface was mainly well-ordered and continuous while step edges and disordered layers are found at the suspension/support interface. This provides strong evidence that the nucleation of the binary NC superlattices was not initiated at the suspension/support interface. A very recent study concluded that superlattices crystallize at the suspension/air interface and then deposit as a floating interfacial layer onto the substrate.³¹ Reports of experiments with casted drops of NC suspensions support this idea.³² Likewise, microcolloid crystallization induced by evaporating the solvent can also be initiated at the solvent/air interface.³³

The superlattice most likely has grown laterally along the interface and downwards during further evaporation of the solvent. Superlattice growth becomes 'confined' when the bottom surface gets close to the support film. In this view, the suspension/support interface

(denoted II in the perpendicular cross-sections (Figure 6b-d,f-h and Figure 7b-d,f-h) provide indications of the superlattice growth close to a wall when the NCs were depleted. The contraction of the superlattice in the direction perpendicular to the support film is then tentatively explained by an anisotropic response to forces of the evaporating solvent retracting through the superlattice during drying.^{31,34} Regarding the possible use of NC superlattices, we anticipate that, e.g., anisotropic lattice contractions and layer-wise rotations of the unit cell must have a dramatic effect on charge carrier generation and transport.

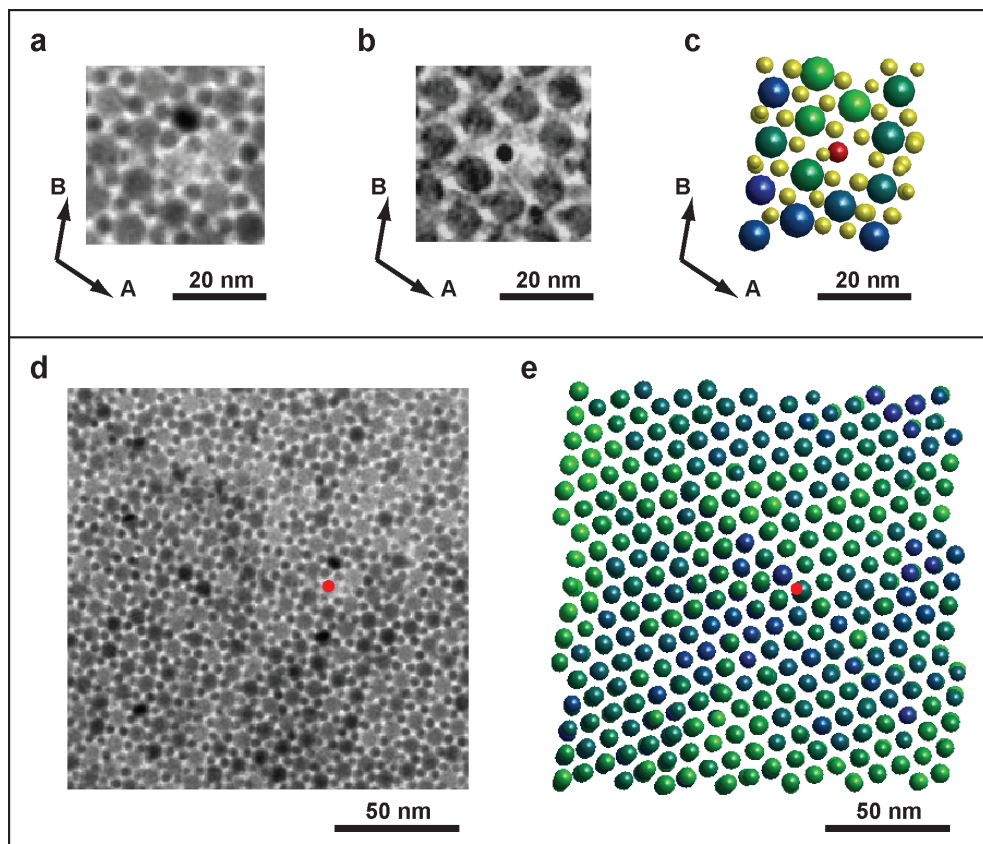


Figure 5 TEM image of AB_2 superlattice consisting of PbSe and Au NCs along (001) direction at zero tilt (a), numerical cross-section through reconstruction parallel to imaging plane with Au substitution in black and stretched PbSe lattice in dark gray (b), and ET analysis with PbSe color coded relative to displacement from lattice (blue=on lattice, green=2.5nm off lattice), Au on lattice in yellow and Au replacing PbSe in red. TEM overview along (001) direction at zero tilt (d) and displacement map of same region with PbSe NCs color coded from blue to green depending on their distance to the next lattice point (e). PbSe in blue are on the lattice and PbSe that are 2.5 nm off their respective lattice position are shown in green. The substitution is indicated by a red dot in panels d and e.

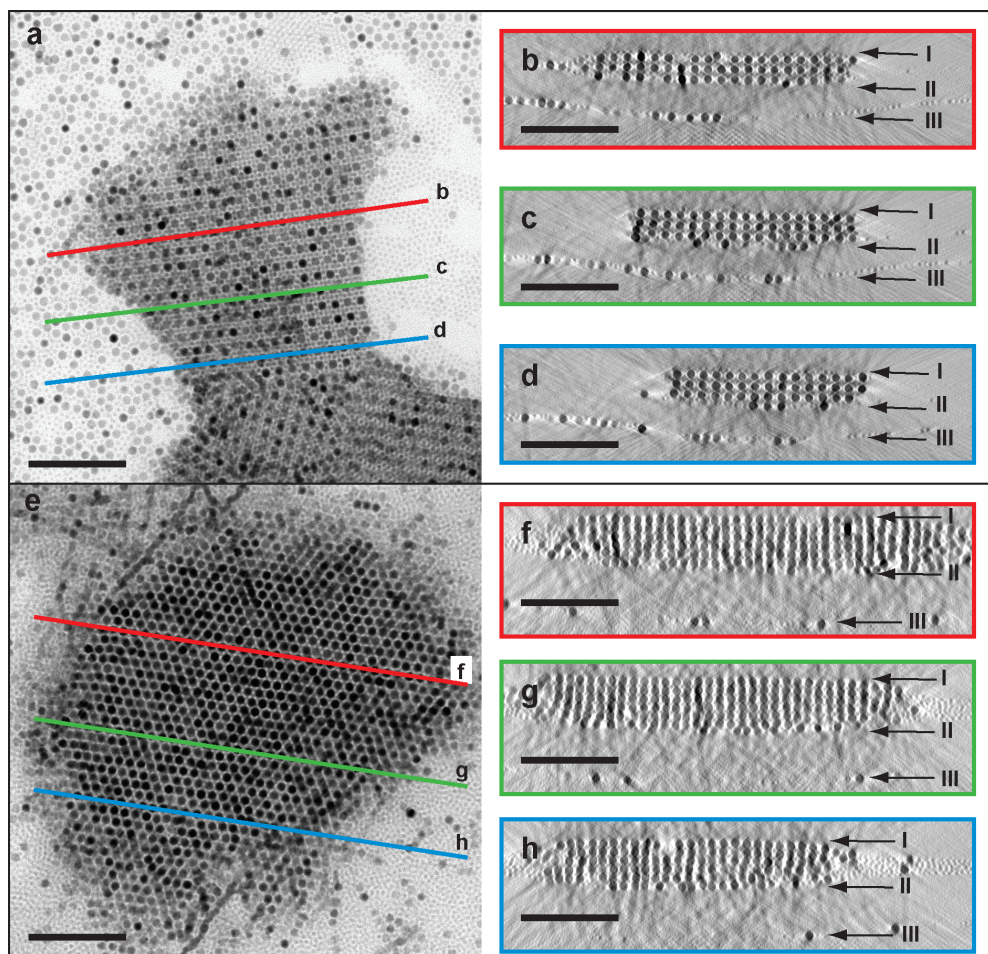


Figure 6. Interface structure of superlattices consisting of PbSe and CdSe NCs. TEM image of AB_{13} lattice at zero tilt (a) with positions of numerical cross-sections perpendicular to the imaging plane indicated in red, green, and blue (b-d). TEM image of AB_2 lattice at zero tilt (a) with positions of numerical cross-sections perpendicular to the imaging plane indicated in red, green, and blue (f-h). Interfaces are indicated by arrows, I (suspension/air), II (suspension/support), and III (opposing side of TEM support film). Scale bars are 100 nm.

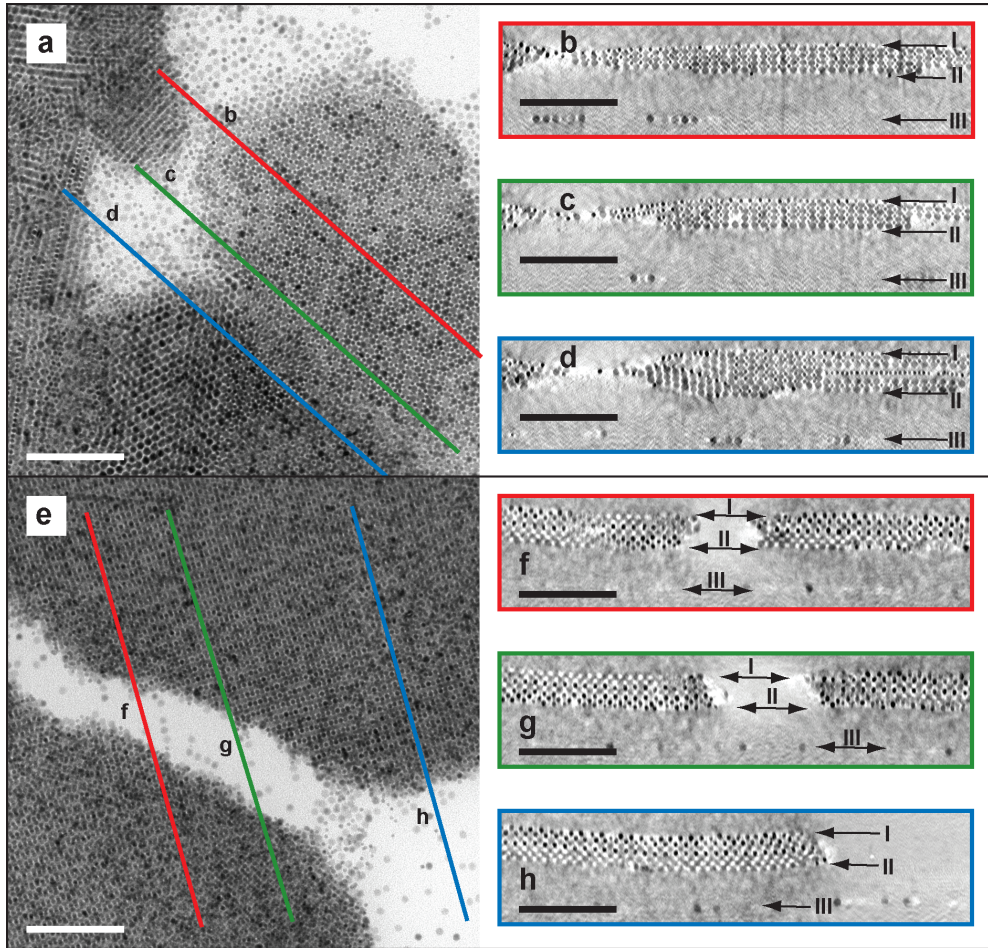


Figure 7. Interface structure of superlattices consisting of PbSe and Au NCs. TEM image of AB_2 lattice at zero tilt (a) with positions of numerical cross-sections perpendicular to the imaging plane indicated in red, green, and blue (b-d). TEM image of AB lattice at zero tilt (e) with positions of numerical cross-sections perpendicular to the imaging plane indicated in red, green, and blue (f-h). Interfaces are indicated by arrows, I (suspension/air), II (suspension/support), and III (opposing side of TEM support film). Scale bars are 100 nm.

6.6 Conclusions

We have shown that electron tomography and image analysis can achieve single NC detection and, thus, is an indispensable method for a quantitative in depth real space study of (binary) nanocrystal superlattices. ET provides accurate lattice parameters of a given superlattice, unambiguously revealing the crystal structure including possible distortions. Furthermore, the ability to detect defects and their effect on the surrounding lattice will be instrumental in a microscopic understanding of emerging materials properties.⁷⁻⁹ In addition, real space analysis already has given clues to crystal nucleation and growth mechanisms, which can be improved by arresting these processes via, e.g., a fast temperature quench. We further anticipate that, as in the microcolloid equivalent where quantitative 3D optical microscopy on a single particle level has led to new insights into fundamental problems such as the glass transition³⁵⁻³⁷, crystallization³⁰ and finally to a determination of inter particle potentials³⁸, electron tomography will be instrumental in extending this knowledge to the nanoscale.

Supporting Information Available: Media files showing an aligned tilt-series (SImovie1) and the corresponding 3D reconstruction (SImovie2) of the AB13 lattice are available free of charge via the Internet at <http://pubs.acs.org>.

Acknowledgements

I would like to thank Cedric Gommès, Karin Overgaag, Hans Meeldijk, Wiel Evers, Bart de Nijs, Mark Boneschanscher, Alfons van Blaaderen, and Daniel Vanmaekelbergh for a very stimulating collaboration on the exquisite binary nanoparticle superlattices. Cedric Gommès is specially acknowledged for the core of the image and structure analysis part and Daniel Vanmaekelbergh and Alfons van Blaaderen for their contributions to the manuscript, critical comments and support throughout this project. Microscopy was performed at the Electron Microscopy group Utrecht (EMU) with a special thanks to Hans Meeldijk, Misjael Lebbink, and Theo van der Krift.

References

- (1) Weller, H. *Adv. Mater.* **1993**, *5*, 88.
- (2) Kiely, C. J.; Fink, J.; Brust, M.; Bethell, D.; Schiffrin, D. J. *Nature* **1998**, *396*, 444.
- (3) Rogach, A. L. *Angew. Chem. Int. Ed.* **2004**, *43*, 148.
- (4) Shevchenko, E. V.; Talapin, D. V.; Kotov, N. A.; O'Brien, S.; Murray, C. B. *Nature* **2006**, *439*, 55.
- (5) Overgaag, K.; Evers, W.; de Nijs, B.; Koole, R.; Meeldijk, J.; Vanmaekelbergh, D. *J. Am. Chem. Soc.* **2008**, *130*, 7833.
- (6) Shevchenko, E. V.; Talapin, D. V.; O'Brien, S.; Murray, C. B. *J. Am. Chem. Soc.* **2005**, *127*, 8741-8747.
- (7) Urban, J. J.; Talapin, D. V.; Shevchenko, E. V.; Kagan, C. R.; Murray, C. B. *Nat. Mater.* **2007**, *6*, 115-121.

- (8) Gur, I.; Fromer, N. A.; Geier, M. L.; Alivisatos, A. P. *Science* **2005**, *310*, 462.
- (9) Talapin, D. V.; Murray, C. B. *Science* **2005**, *310*, 86.
- (10) Connolly, S.; Fullam, S.; Korgel, B.; Fitzmaurice, D. *J. Am. Chem. Soc.* **1998**, *120*, 2969.
- (11) Sakamoto, Y.; Kaneda, S.; Terasaki, O.; Zhao, D. Y.; Kim, J. M.; Stucky, G.; Shim, H. J.; Ryoo, R. *Nature* **2000**, *408*, 449.
- (12) Koster, A. J.; Grimm, R.; Typke, D.; Hegerl, R.; Stoschek, A.; Walz, J.; Baumeister, W. *J. Struct. Biol.* **1997**, *120*, 276.
- (13) McIntosh, R.; Nicastro, D.; Mastronarde, D. *Trends Cell Biol.* **2005**, *15*, 43.
- (14) Friedrich, H.; de Jongh, P. E.; Verkleij, A. J.; de Jong, K. P. *Chem. Rev.* **2009**, DOI: 10.1021/cr800434t.
- (15) Midgley, P. A.; Ward, E. P. W.; Hungria, A. B.; Thomas, J. M. *Chem. Soc. Rev.* **2007**, *36*, 1477.
- (16) Park, J. B.; Lee, J. H.; Choi, H. R. *Appl. Phys. Lett.* **2007**, *90*, 093111.
- (17) Ahrenkiel, S. P.; Yu, P. R.; Murphy, J. E.; Nedeljkovic, J. M.; Donohoe, B. S. *J. Microsc.-Oxford* **2008**, *230*, 382.
- (18) Evers, W. MA thesis, Condensed Matter and Interfaces, Debye Institute for Nanomaterials Science, Utrecht University, 2008.
- (19) de Nijs, B. MA thesis, Condensed Matter and Interfaces, Debye Institute for Nanomaterials Science, Utrecht University, 2008.
- (20) Overgaag, K. PhD thesis, Condensed Matter and Interfaces, Debye Institute for Nanomaterials Science, Utrecht University, 2008.
- (21) Moreels, I.; Lambert, K.; De Muynck, D.; Vanhaecke, F.; Poelman, D.; Martins, J. C.; Allan, G.; Hens, Z. *Chem. Mater.* **2007**, *19*, 6101.
- (22) Yu, W. W.; Qu, L. H.; Guo, W. Z.; Peng, X. G. *Chem. Mater.* **2003**, *15*, 2854.
- (23) Kremer, J. R.; Mastronarde, D. N.; McIntosh, J. R. *J. Struct. Biol.* **1996**, *116*, 71.
- (24) Frangakis, A. S.; Bohm, J.; Forster, F.; Nickell, S.; Nicastro, D.; Typke, D.; Hegerl, R.; Baumeister, W. *Proc. Nat. Acad. Sci. U.S.A.* **2002**, *99*, 14153.
- (25) Bohm, J.; Frangakis, A. S.; Hegerl, R.; Nickell, S.; Typke, D.; Baumeister, W. *Proc. Nat. Acad. Sci. U.S.A.* **2000**, *97*, 14245.
- (26) Lebbink, M. N.; Geerts, W. J. C.; van der Krift, T. P.; Bouwhuis, M.; Hertzberger, L. O.; Verkleij, A. J.; Koster, A. J. *J. Struct. Biol.* **2007**, *158*, 327.
- (27) Gommès, C. J.; Friedrich, H.; Wolters, M.; de Jongh, P. E.; de Jong, K. P. *Chem. Mater.* **2009**, *21*, 1311.
- (28) Eldridge, M. D.; Madden, P. A.; Frenkel, D. *Nature* **1993**, *365*, 35.
- (29) Hytch, M. J.; Snoeck, E.; Kilaas, R. *Ultramicroscopy* **1998**, *74*, 131.
- (30) Schall, P.; Cohen, I.; Weitz, D. A.; Spaepen, F. *Nature* **2006**, *440*, 319.
- (31) Smith, D. K.; Goodfellow, B.; Smilgies, D. M.; Korgel, B. A. *J. Am. Chem. Soc.* **2009**, *131*, 3281-3290.
- (32) Bigioni, T. P.; Lin, X. M.; Nguyen, T. T.; Corwin, E. I.; Witten, T. A.; Jaeger, H. M. *Nat. Mater.* **2006**, *5*, 265.
- (33) Li, W. J.; Fu, T.; He, S. L. *Mater. Sci. Eng., A* **2006**, *441*, 239.
- (34) Klotz, M.; Albouy, P. A.; Ayrat, A.; Menager, C.; Grosso, D.; van der Lee, A.; Cabuil, V.; Babonneau, F.; Guizard, C. *Chem. Mater.* **2000**, *12*, 1721.
- (35) van Blaaderen, A.; Wiltzius, P. *Science* **1995**, *270*, 1177.
- (36) Weeks, E. R.; Crocker, J. C.; Levitt, A. C.; Schofield, A.; Weitz, D. A. *Science* **2000**, *287*, 627.
- (37) Kegel, W. K.; van Blaaderen, A. *Science* **2000**, *287*, 290.
- (38) Royall, C. P.; Leunissen, M. E.; van Blaaderen, A. *J. Phys.: Condens. Matter* **2003**, *15*, S3581.



Chapter 7

Summary and Outlook

Electron tomography (ET) is a powerful method for the real-space three-dimensional (3D) characterization of nanostructured materials. Over the past decade, developments in instrumentation and automation have encouraged its application throughout the biological, chemical and physical sciences. In chapter 2, the application of ET to heterogeneous catalysts and related nanostructured materials was reviewed. From the presented examples it became evident that knowing a materials 3D morphology significantly aids in understanding its physico-chemical properties. Moreover, the potential to extract quantitative information on constituent phases by image analysis of electron tomograms was recognized as a next key step. The remaining chapters of this thesis aimed at the development of ET towards a quantitative imaging tool for nanostructured materials. In Chapter 3 we employed a combination of ET, N₂-physisorption and XRD to investigate NiO/SBA-15 model catalysts. Differences in the dispersion of the nickel oxide phase arising from differences in the gas atmosphere during thermal decomposition of the nickel nitrate in the pores of the support were revealed. While thermal decomposition in air and He atmospheres led to sintering and transport of the nickel precursor phase to form rod-like NiO particles, in an NO/He atmosphere exclusively small NiO particles were created. Image analysis by manual segmentation illustrated the formation of cavities between pairs of rod-like NiO particles confined within the same SBA-15 mesopore, thus rationalizing the shape of the hysteresis loop in the N₂-physisorption isotherms. Moreover, the micropores in the silica wall permitted NiO on the support exterior and in neighboring mesopores to be connected by bridges. A more detailed study of NiO structures on the support exterior showed their porous nature and quantified the specific surface area (25-40 m² g⁻¹), relevant information for application in catalysis. The highest dispersion of the NiO, maximizing the number of catalytically active sites, was achieved in an NO/He atmosphere. A quantitative analysis of this catalyst was presented in chapter 4. NiO particle locations, sizes (~ 4 nm), and nearest neighbor distances (~ 2 nm) were obtained by manual segmentation. Furthermore, the local NiO loading was determined by combining structural parameters from local (ET) and bulk (N₂-physisorption, XRD) characterization. In NiO filled pores the local loading was almost twice the applied average which was compensated by a large percentage of unfilled pores. For catalytic applications the observed high local loading combined with a high dispersion is remarkable. However, more research on uniform filling of the SBA-15 mesopores by the nickel nitrate precursor during the preceding impregnation and drying steps is required. Aided by ET, these studies will further increase our understanding and boost control over the individual steps of catalyst preparation. In addition, investigations of unloaded supports unraveled their local structure, e.g. corrugation of SBA-15 mesopores¹ or tunable mesopore accessibility in ordered mesoporous organosilica², that may significantly impact catalyst preparation. Since manual segmentation is a rather labor intensive approach, automated image analysis procedures were implemented. Chapter 5 focused on threshold-based segmentation of electron tomograms. To this end, a criterion for automated (and thus reproducible and operator-independent) determination of the segmentation threshold was proposed and subsequently validated in experiments and numerical simulations.

Au and Ru particles as small as 1 nm were detected and quantified to obtain size distributions over tens to thousands of particles. For a Ru/carbon nanotube catalyst differences in particle size depending on the location of the Ru particle, i.e. inside (1-4 nm) or outside the tube (1-3 nm), were found. Overall, 80 vol% of the Ru was located inside the tube at a local catalyst loading of 3.2 wt%. This information is essential since the curvature of the nanotube wall might significantly influence the particles catalytic performance. For the Au@zirconia system structural details of the porous zirconia shell were revealed and not only the Au (~ 18 nm) but also the ZrO₂ (~ 5 nm) particle sizes measured. While automated thresholding of electron tomograms offers detection and quantification irrespective of object shape and size, these two parameters can be taken into account in model-based approaches. Chapter 6 presented a quantitative model-based analysis of four binary nanoparticle superlattices composed of PbSe, CdSe and Au nanocrystals (NC). For thousands of NCs in each tomogram particle coordinates were determined by cross-correlation with multiple synthetic templates and core diameters measured from the radially averaged intensity profile.¹ Positional order and local bond-order parameters were utilized to locate individual crystallites for which lattice vectors, unit cell positions, and neighbor distances were calculated and crystallographic point/plane defects studied. Information such as the observed anisotropic deformation of some unit cells after drying is indispensable to understand the properties that emerge from assembly into superlattices. In addition, ET results on the order/disorder at the top and bottom surfaces suggested that superlattice nucleation and growth occurred at the suspension/air interface. In the future application of ET for the real space analysis of mono component, binary, and ternary NC superlattices of known (deduced from TEM) or unknown symmetry are expected. We further anticipate that, as for microcolloids, where quantitative 3D optical microscopy has led to fundamental insights into crystallization, the glass transition, and inter-particle potentials, ET will be instrumental in extending this knowledge to the nanoscale. In this thesis a number of examples and approaches to obtain quantitative structural information by image analysis of electron tomograms are given. With a wealth of nanostructural data at hand, the challenge ahead lies in directly relating this information to the nanomaterials properties. ET delivers fundamental insights into the local 3D morphology of complex nanostructured materials and will contribute to a more rational design in the future.

References

- (1) Gommès, C. J.; Friedrich, H.; Wolters, M.; de Jongh, P. E.; de Jong, K. P. *Chem. Mater.* **2009**, *21*, 1311.
- (2) Vercaemst, C.; Friedrich, H.; de Jongh, P. E.; Neimark, A. V.; Goderis, B.; Verpoort, F.; van der Voort, P. *J. Phys. Chem. C* **2009**, *113*, 5556.

Samenvatting

Electron Tomografie (ET) is een effectieve methode voor het karakteriseren van de driedimensionale nanostructuur van vaste stoffen. In het afgelopen decennium hebben ontwikkelingen in automatisering en instrumentatie geleid tot toepassingen op biologisch, chemisch en fysisch gebied. In hoofdstuk 2 is een overzicht gegeven van de toepassing van ET op heterogene katalysatoren en aanverwante materialen. Uit de getoonde voorbeelden wordt duidelijk dat de kennis van de driedimensionale-structuur aanzienlijk bijdraagt tot het begrip van de fysisch-chemische eigenschappen. Een belangrijk element is bovendien de mogelijkheid om via beeldanalyse kwantitatieve informatie over de samengestelde vaste fasen te verkrijgen. De volgende hoofdstukken van dit proefschrift richten zich op de ontwikkeling van ET als techniek om kwantitatief de nanostructuur van materialen in beeld te brengen. In hoofdstuk 3 hebben we gebruik gemaakt van ET, N₂-fysisorptie en röntgendiffractie om NiO/SBA-15 modelsystemen te onderzoeken. Zo is aangetoond dat de verdeling van nikkeloxyde deeltjes in de poriën van het dragermateriaal verandert als gevolg van verschillen in de gasatmosfeer tijdens de thermische ontleding van nikkelnitraat. Terwijl thermische ontleding in lucht en/of in helium atmosfeer aanleiding geeft tot sintering en transport van het nikkelhoudend materiaal om uiteindelijk tot vorming van staafvormige deeltjes te leiden, worden tijdens ontleding in NO/He atmosfeer uitsluitend kleine NiO deeltjes gevormd. Beeldanalyse door handmatige segmentatie toonde het ontstaan van lege ruimtes aan tussen de staafvormige NiO deeltjes binnen eenzelfde SBA-15 mesoporie, waarmee de hysteresis in de N₂-fysisorptie isotherm verklaard kan worden. Bovendien geven de microporiën in de siliciumdioxidewanden van de SBA-15 drager aanleiding tot vorming van verbindingen van het NiO aan de buitenzijde van de drager en dat in de aangrenzende mesoporiën. Een meer gedetailleerd onderzoek van de NiO deeltjes aan het buitenoppervlak van de drager toont hun poreuze structuur en geeft kwantitatieve informatie over het specifiek oppervlak (25-40 m² g⁻¹), hetgeen relevante informatie voor toepassingen in de katalyse is. De hoogste dispersie van de NiO (het maximale aantal katalytisch actieve plaatsen) wordt bereikt in een NO/He atmosfeer. Een kwantitatieve analyse van een op deze manier bereide katalysator is gepresenteerd in hoofdstuk 4. Van de NiO deeltjes zijn de locaties, de afmetingen (~ 4 nm) en de naaste-buur afstanden (~ 2 nm) bepaald door handmatige segmentatie. Verder is de lokale NiO belading bepaald door de structurele parameters van de lokale (ET) en van de 'bulk' (N₂-fysisorptie en XRD) karakterisering te combineren. In de met NiO gevulde poriën is de lokale belading bijna tweemaal zo hoog als het gemiddelde, hetgeen gecompenseerd wordt door het hoge percentage onge vulde poriën. Dankzij ET zullen deze studies een beter begrip geven en het beheersen van de individuele stappen in de katalysator bereiding verbeteren. Bovendien heeft onderzoek aan kale dragermaterialen de lokale structuur getoond, zoals bijvoorbeeld het gegolfde oppervlak van de mesoporiën van het SBA-15¹ of bij de variable toegankelijkheid van de mesoporiën van geordende mesoporeuze organosilicaverbindingen², die de katalysator bereiding significant beïnvloedt. Aangezien handmatige segmentatie een nogal arbeidsintensieve

methode is, zijn geautomatiseerde beeldanalyse procedures toegepast. Hoofdstuk 5 richt zich op electron tomogrammen die gebaseerd zijn op segmentatie via een drempelwaarde. Hiertoe is er een criterium voorgesteld voor geautomatiseerde (en dus reproduceerbare en gebruikers-onafhankelijke) bepaling van de segmentatie drempelwaarde. Dit criterium is vervolgens gevalideerd in experimentele en numerieke simulaties. Goud en ruthenium deeltjes met een grootte van ~ 1 nm zijn gedetecteerd en deeltjesgrootteverdelingen van tientallen tot duizenden deeltjes werden verkregen. Bij een Ru/koolstof nanobuis katalysator werden variaties in deeltjesgrootte gevonden die afhankelijk waren van de locatie van het Ru-deeltje: namelijk binnenin (1-4 nm) en aan de buitenkant van de buizen (1-3 nm). Globaal genomen werd er 80 vol% van het ruthenium binnenin de buis aangetroffen bij een totale belading van 3,2 gew%. Deze informatie is essentieel aangezien de kromming van de wand van de nanobuisjes de katalytische activiteit van de deeltjes sterk kan beïnvloeden. Bij het zirconiumdioxide-ge dragen goud systeem werden de structurele details van de zirconiumdioxide schil aangetoond en werd de deeltjesgrootte van zowel de Au (~ 18 nm) als van de ZrO₂ deeltjes (~ 5 nm) gemeten. Hoewel de geautomatiseerde drempelwaarde methode van electron tomogramdetectie de mogelijkheid tot kwantificering biedt, ongeacht de vorm en de grootte van een deeltje, kunnen deze twee parameters meegenomen worden in een model-gebaseerde aanpak. Hoofdstuk 6 toont een kwantitatief model-gebaseerde analyse van superroosters van vier verschillende binaire systemen van nanodeeltjes samengesteld uit PbSe, CdSe en Au nanokristallen (NK). Van duizenden NK werden met beeldanalyse in elk tomogram zowel de coördinaten mbv kruiscorrelatie met meerdere synthetische sjablonen als de kerndiameter bepaald uit het straalsgewijs gemiddelde intensiteitsprofiel. Positionele klassering en parameters voor het lokale bindingstype zijn gebruikt om de individuele kristallieten te lokaliseren waarvan de rooster vectoren, eenheidscel posities en de aangrenzende afstanden zijn berekend en kristallografische punt- en vlakdefecten zijn bestudeerd. Informatie over bijvoorbeeld de waargenomen anisotrope vervorming van enkele eenheidscellen na droging is onmisbaar om de fenomenen te begrijpen die optreden tijdens de vorming van superroosters. Daarnaast suggereerden de ET resultaten m.b.t. de orde/wanorde op de boven- en ondervlakken dat de nucleatie en de groei van het superrooster plaatsvindt aan het vloeistof/lucht grensvlak. In de toekomst worden toepassingen verwacht van ET voor de analyse van enkele, binaire en ternaire NK-superroosters van bekende (verkregen via TEM) of onbekende symmetrieën. Verder anticiperen wij dat, net als bij microcolloïden waar kwantitatieve 3D-optische microscopie geleid heeft tot fundamenteel inzicht in kristallisatie, voor de glastransitie en de potentiaal tussen deeltjes onderling, ET het instrument zal zijn dat zal leiden tot vergelijkbare inzichten op nanoschaal. In dit proefschrift zijn een aantal voorbeelden en methoden gegeven om kwantitatieve structurele informatie middels beeldanalyse van electron tomogrammen te verkrijgen. Met een rijkdom aan beschikbare nano-structuur gegevens, ligt voor de toekomst de uitdaging in het direct relateren van deze informatie aan de eigenschappen van de nanomaterialen. ET levert fundamentele inzichten in de lokale 3D morfologie van de complexe nanostructuur van materialen en zal bijdragen aan het meer rationeel ontwerpen hiervan in de toekomst.

Acknowledgements

I would like to thank Nuria, Matthia, Mariska, Petra, Mathijs, Hans, John, and Arie for the translation of the summary.

References

- (1) Gommès, C. J.; Friedrich, H.; Wolters, M.; de Jongh, P. E.; de Jong, K. P. *Chem. Mater.* **2009**, *21*, 1311.
- (2) Vercaemst, C.; Friedrich, H.; de Jongh, P. E.; Neimark, A. V.; Goderis, B.; Verpoort, F.; van der Voort, P. *J. Phys. Chem. C* **2009**, *113*, 5556.

Appendix

Table 1 ET analysis of AB₂ superlattice consisting of PbSe and CdSe NCs.

Particle size distribution and shell thickness (normal distribution) in nm

Region	PbSe d _{core}	PbSe t _{min}	PbSe t _{3NN}	CdSe d _{core}	CdSe t _{min}	CdSe t _{3NN}
ROI 1	9.0±0.3	-0.3±0.7*	0.5±0.5	3.4±0.5	1.1±0.4	1.4±0.3
ROI 2	9.0±0.3	-0.4±0.9*	0.5±0.6	3.4±0.5	1.2±0.4	1.5±0.3
ROI 3	9.0±0.3	-0.4±0.7*	0.5±0.5	3.4±0.5	1.1±0.3	1.5±0.2
ROI 4	9.0±0.3	-0.4±0.7*	0.5±0.6	3.3±0.5	1.1±0.4	1.4±0.3

Unit cell vector length and average displacement (rms) from lattice in nm

Region	A [nm]	B [nm]	C [nm]	Volume [nm ³]
ROI 1	11.2±0.8	11.7±0.6	8.4±1.0	956
ROI 2	11.6±0.7	11.4±0.7	8.4±0.9	982
ROI 3	11.2±0.7	11.5±0.6	8.4±0.9	970
ROI 4	11.4±0.6	11.7±0.6	8.0±1.1	928

Unit cell vector angles in degrees

Region	AB [°]	BC [°]	CA [°]
ROI 1	119.9	91.7	88.8
ROI 2	117.8	90.0	90.5
ROI 3	116.2	91.1	88.5
ROI 4	118.4	86.4	90.3

Unit cell filling fractions (ρ) and size ratios (γ)

Region	$\rho(d_{\text{core}})$	$\rho(d_{\text{core}}+t_{\text{min}})$	$\rho(d_{\text{core}}+t_{3\text{NN}})$	$\gamma(d_{\text{core}})$	$\gamma(d_{\text{core}}+t_{\text{min}})$	$\gamma(d_{\text{core}}+t_{3\text{NN}})$
ROI 1	0.439	0.451	0.586	0.379	0.517	0.508
ROI 2	0.428	0.439	0.584	0.376	0.533	0.512
ROI 3	0.436	0.448	0.587	0.374	0.520	0.507
ROI 4	0.458	0.466	0.614	0.368	0.512	0.497

CdSe position (mean±std) in unit cell of ROI 2 expressed in multiples of A,B,C

	A	B	C
CdSe 1	0.34±0.05	0.69±0.06	0.51±0.11
CdSe 2	0.63±0.05	0.28±0.06	0.49±0.09

* A negative minimum neighbor distance (t_{min}) which could be interpreted as penetration of the NC hard cores is unphysical. Instead it results from analyzing NC in terms of spheres which only approximates their actual shape of a faceted crystallite.

Table 2 ET analysis of AB₂ superlattice consisting of PbSe and Au NCs.

Particle size distribution and shell thickness (normal distribution) in nm

Region	PbSe d_{core}	PbSe t_{min}	PbSe $t_{3\text{NN}}$	Au d_{core}	Au t_{min}	Au $t_{3\text{NN}}$
ROI 1	7.1±0.4	0.2±0.7*	0.8±0.5	3.7±0.4	0.9±0.3	1.2±0.2
ROI 2	7.1±0.4	-0.2±0.7*	0.5±0.5	3.7±0.4	0.9±0.3	1.2±0.2
ROI 3	7.1±0.4	0.1±0.7*	0.7±0.5	3.7±0.4	0.9±0.3	1.2±0.3

Unit cell vector length and average displacement (rms) from lattice in nm

Region	A [nm]	B [nm]	C [nm]	Volume [nm ³]
ROI 1	9.8±0.4	10.1±0.4	7.2±0.5	630
ROI 2	10.2±1.1	10.3±0.9	6.5±0.7	594
ROI 3	9.9±0.4	10.0±0.4	6.7±0.8	581

Unit cell vector angles in degrees

Region	AB [°]	BC [°]	CA [°]
ROI 1	117.5	90.1	91.9
ROI 2	119.6	90.1	91.2
ROI 3	117.8	90.4	90.4

Unit cell filling fractions (ρ) and size ratios (γ)

Region	$\rho(d_{\text{core}})$	$\rho(d_{\text{core}}+t_{\text{min}})$	$\rho(d_{\text{core}}+t_{3\text{NN}})$	$\gamma(d_{\text{core}})$	$\gamma(d_{\text{core}}+t_{\text{min}})$	$\gamma(d_{\text{core}}+t_{3\text{NN}})$
ROI 1	0.388	0.502	0.616	0.524	0.633	0.628
ROI 2	0.408	0.469	0.593	0.525	0.662	0.641
ROI 3	0.410	0.506	0.626	0.522	0.645	0.634

Au position (mean±std) in unit cell of ROI 3 expressed in multiples of A,B,C

	A	B	C
Au 1	0.33±0.05	0.68±0.05	0.52±0.08
Au 2	0.65±0.05	0.32±0.05	0.51±0.09

* A negative minimum neighbor distance (t_{min}) which could be interpreted as penetration of the NC hard cores is unphysical. Instead it results from analyzing NC in terms of spheres which only approximates their actual shape of a faceted crystallite.

Table 3 ET analysis of AB₁₃ superlattice consisting of PbSe and CdSe NCs.

Particle size distribution and shell thickness (normal distribution) in nm

Region	PbSe d_{core}	PbSe t_{min}	PbSe $t_{3\text{NN}}$	CdSe d_{core}	CdSe t_{min}	CdSe $t_{3\text{NN}}$
ROI 1	8.8±0.3	0.1±0.7*	0.5±0.4	3.8±0.4	0.6±0.5	0.9±0.3
ROI 2	8.8±0.3	0.2±0.4*	0.5±0.3	3.8±0.4	0.6±0.4	0.9±0.3
ROI 3	8.8±0.3	0.1±0.4*	0.4±0.3	3.8±0.4	0.5±0.4	0.9±0.3
ROI 4	8.7±0.4	0.2±0.7*	0.6±0.4	3.6±0.4	0.7±0.5	1.1±0.3
ROI 5	8.7±0.3	0.2±0.8*	0.7±0.4	3.7±0.4	0.6±0.4	1.0±0.3

Unit cell vector length and average displacement (rms) from lattice in nm

Region	A [nm]	B [nm]	C [nm]	Volume [nm ³]
ROI 1	14.0±0.5	14.4±0.6	10.2±0.7	2059
ROI 2	13.7±0.5	14.7±0.4	9.8±0.7	1978
ROI 3	13.7±0.6	15.2±0.4	10.0±0.6	2081
ROI 4	13.9±0.5	14.2±0.6	11.1±0.9	2187
ROI 5	13.8±0.5	13.9±0.7	11.2±0.7	2053

Unit cell vector angles in degrees

Region	AB [°]	BC [°]	CA [°]
ROI 1	92.3	89.9	93.4
ROI 2	88.8	89.7	89.7
ROI 3	91.8	90.4	88.2
ROI 4	93.8	92.3	87.4
ROI 5	96.2	90.9	106.1

Unit cell filling fractions (ρ) and size ratios (γ)

Region	$\rho(d_{\text{core}})$	$\rho(d_{\text{core}}+t_{\text{min}})$	$\rho(d_{\text{core}}+t_{3\text{NN}})$	$\gamma(d_{\text{core}})$	$\gamma(d_{\text{core}}+t_{\text{min}})$	$\gamma(d_{\text{core}}+t_{3\text{NN}})$
ROI 1	0.358	0.459	0.555	0.433	0.491	0.512
ROI 2	0.373	0.488	0.583	0.432	0.486	0.510
ROI 3	0.347	0.437	0.530	0.433	0.488	0.514
ROI 4	0.307	0.413	0.513	0.416	0.479	0.502
ROI 5	0.331	0.435	0.543	0.422	0.483	0.500

* A negative minimum neighbor distance (t_{min}) which could be interpreted as penetration of the NC hard cores is unphysical. Instead it results from analyzing NC in terms of spheres which only approximates their actual shape of a faceted crystallite.

Table 4 ET analysis of AB superlattice consisting of PbSe and Au NCs.

Particle size distribution and shell thickness (normal distribution) in nm

Region	PbSe d_{core}	PbSe t_{min}	PbSe $t_{3\text{NN}}$	Au d_{core}	Au t_{min}	Au $t_{3\text{NN}}$
ROI 1	6.8±0.5	0.5±0.6*	1.0±0.5	4.6±0.4	1.3±0.3	1.6±0.3
ROI 2	6.8±0.4	0.5±0.6*	1.0±0.5	4.6±0.4	1.3±0.3	1.6±0.3
ROI 3	6.9±0.4	0.2±0.4*	0.6±0.3	4.6±0.4	1.3±0.3	1.6±0.2
ROI 4	6.9±0.4	0.6±0.6	1.0±0.5	4.4±0.5	1.2±0.4	1.6±0.4

Unit cell vector length and average displacement (rms) from lattice in nm

Region	A [nm]	B [nm]	C [nm]	Volume [nm ³]
ROI 1	10.9±0.6	10.4±0.5	10.5±0.6	1187
ROI 2	10.6±0.6	10.5±0.5	10.6±0.7	1175
ROI 3	10.7±0.4	10.8±0.4	10.5±0.4	1222
ROI 4	10.4±0.7	10.4±0.4	11.0±0.6	1174

Unit cell vector angles in degrees

Region	AB [°]	BC [°]	CA [°]
ROI 1	90.2	89.6	88.0
ROI 2	91.3	86.6	88.8
ROI 3	91.1	91.3	90.0
ROI 4	91.5	91.2	97.4

Unit cell filling fractions (ρ) and size ratios (γ)

Region	$\rho(d_{\text{core}})$	$\rho(d_{\text{core}}+t_{\text{min}})$	$\rho(d_{\text{core}}+t_{3\text{NN}})$	$\gamma(d_{\text{core}})$	$\gamma(d_{\text{core}}+t_{\text{min}})$	$\gamma(d_{\text{core}}+t_{3\text{NN}})$
ROI 1	0.224	0.353	0.420	0.682	0.824	0.808
ROI 2	0.226	0.352	0.420	0.670	0.797	0.791
ROI 3	0.224	0.332	0.384	0.662	0.824	0.813
ROI 4	0.221	0.345	0.410	0.647	0.765	0.768

PbSe and Au in face centered positions (mean±std) in unit cell of ROI 3 expressed in multiples of A,B,C

	A	B	C
Au 1	0.02±0.04	0.50±0.03	0.53±0.04
Au 2	0.48±0.05	0.49±0.03	1.00±0.05
Au 3	0.98±0.05	0.49±0.03	0.53±0.05
Au 4	0.49±0.04	0.50±0.03	0.05±0.05
PbSe 1	0.50±0.05	1.00±0.03	0.51±0.05
PbSe 2	0.50±0.05	0.01±0.03	0.51±0.03

* A negative minimum neighbor distance (t_{min}) which could be interpreted as penetration of the NC hard cores is unphysical. Instead it results from analyzing NC in terms of spheres which only approximates their actual shape of a faceted crystallite.

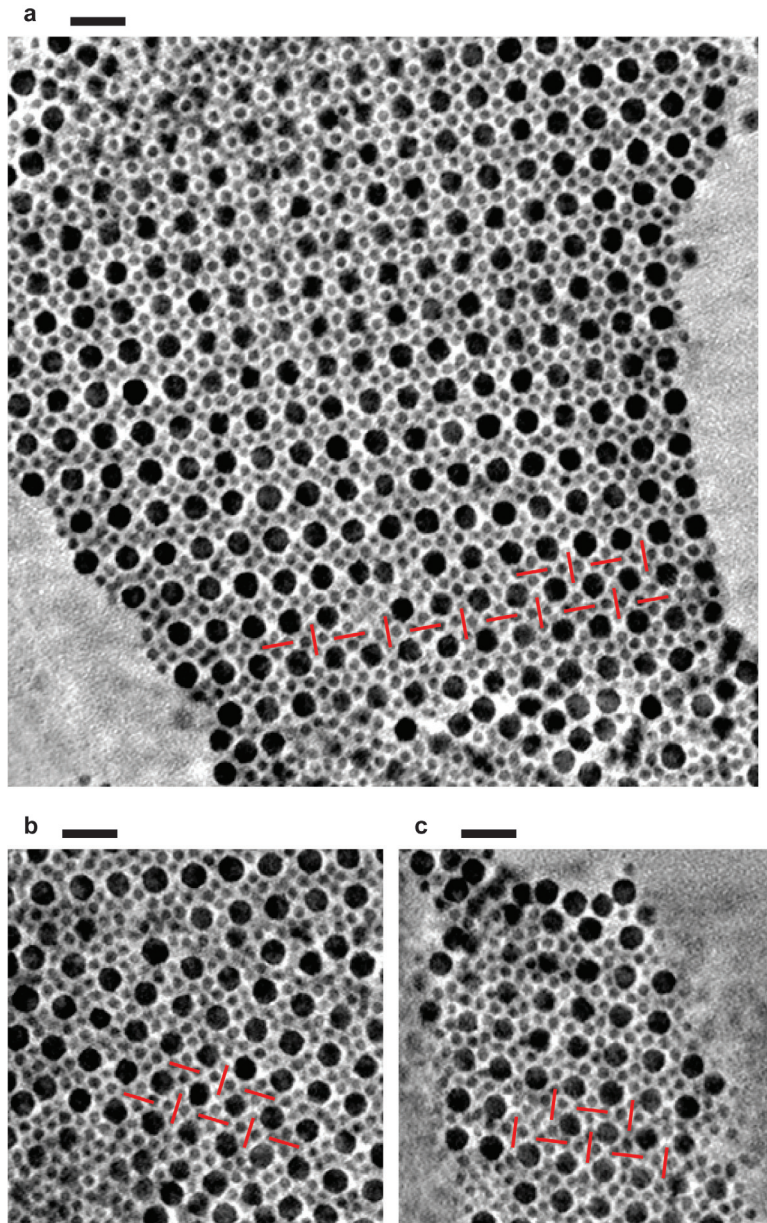


Figure A.1. Numerical cross-sections (interpolated from 0.54 nm/px) parallel to the [001] lattice planes of AB₁₃ lattices composed of PbSe and CdSe NCs. The cross-sections slice through the PbSe and the four CdSe closest to the [001] lattice plane. (a) crystallite in ROI 1 to 3, (b) crystallite in ROI 4, and (c) crystallite in ROI 5. As a visual guide the elongation of the CdSe quadrangle, alternating by 90° between neighbouring cells, is indicated by red lines. Scale bars are 20 nm.

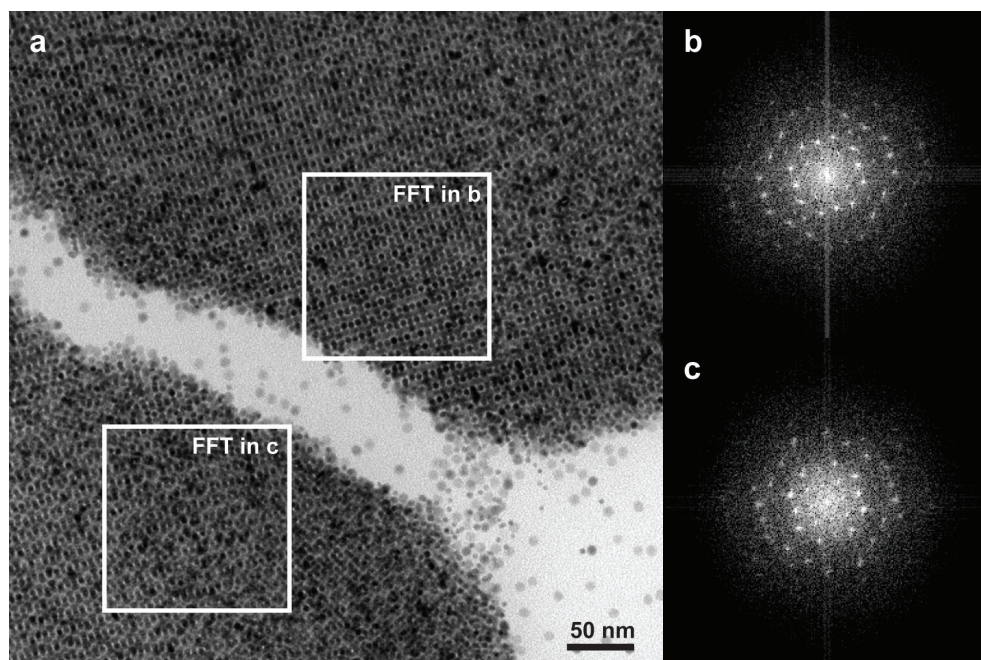


Figure A.2 TEM image along (010) direction at zero tilt of AB superlattice composed of PbSe and Au NCs (a), Fast Fourier Transforms (FFT) of indicated regions (b,c) illustrate the underlying periodicity.

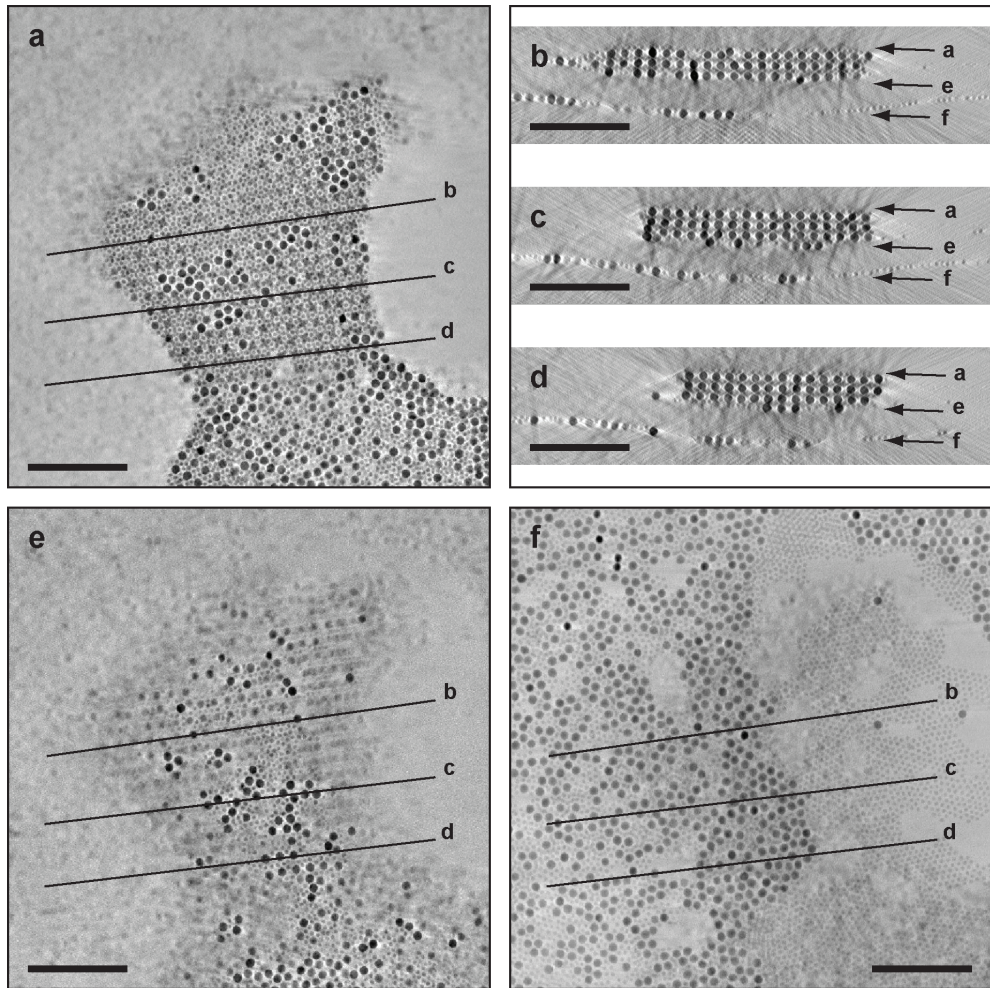


Figure A.3 Interface structure of AB_{13} superlattices consisting of PbSe and CdSe NCs. Numerical cross-sections parallel (a,e,f), and perpendicular (b-d) to the TEM support film illustrating the morphology of the suspension/air interface (a), suspension/support interface (e), and opposing side of TEM support film (f). The relative position of the sections are indicated by lines in a,e,f and by arrows in b-d. Scale bars are 100 nm.

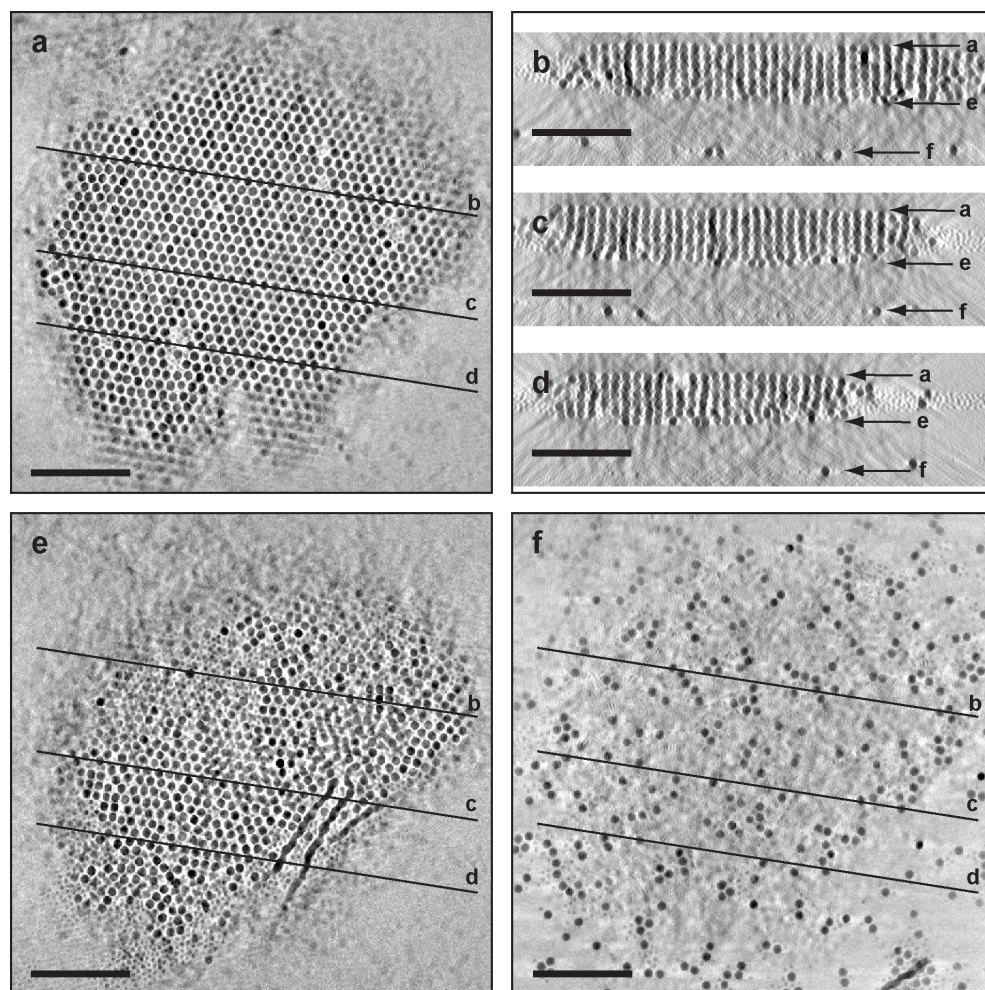


Figure A.4 Interface structure of AB_2 superlattices consisting of PbSe and CdSe NCs. Numerical cross-sections parallel (a,e,f), and perpendicular (b-d) to the TEM support film illustrating the morphology of the suspension/air interface (a), suspension/support interface (e), and opposing side of TEM support film (f). The relative position of the sections are indicated by lines in a,e,f and by arrows in b-d. Scale bars are 100 nm.

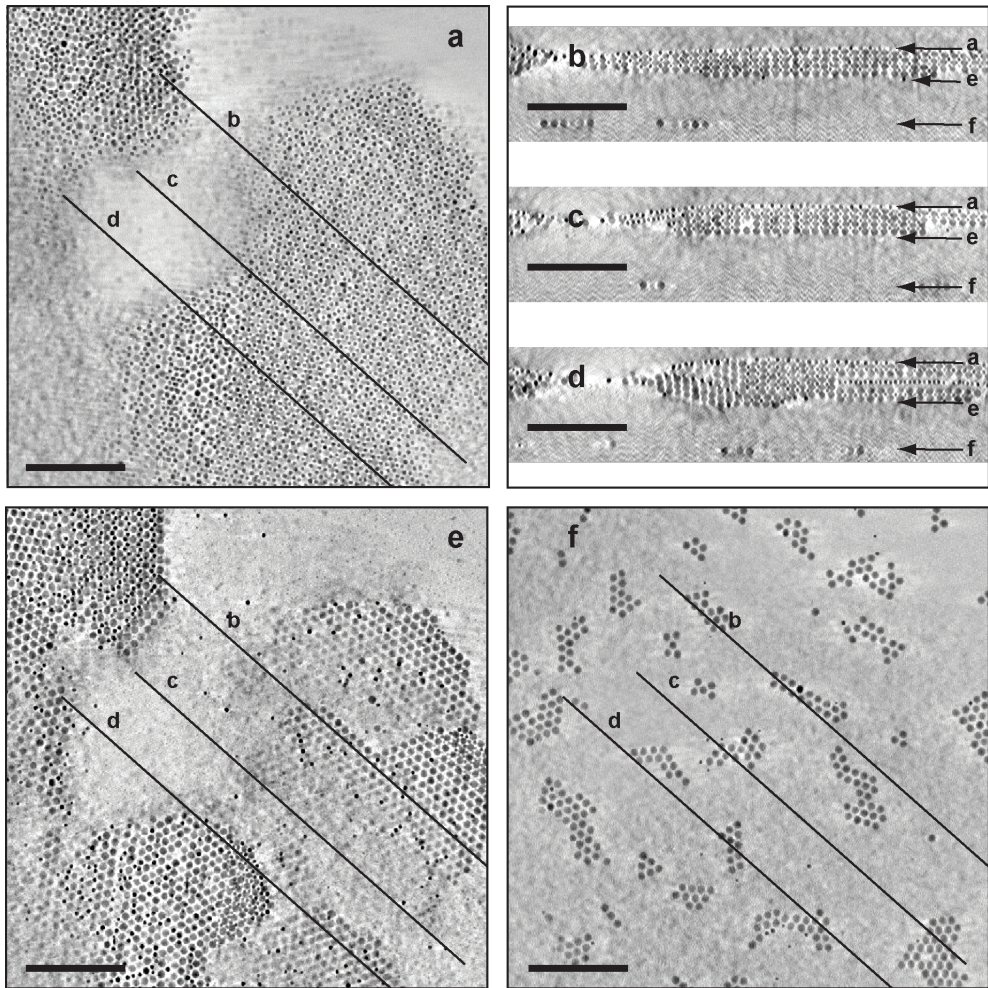


Figure A.5 Interface structure of AB_2 superlattices consisting of PbSe and Au NCs. Numerical cross-sections parallel (a,e,f), and perpendicular (b-d) to the TEM support film illustrating the morphology of the suspension/air interface (a), suspension/support interface (e), and opposing side of TEM support film (f). The relative position of the sections are indicated by lines in a,e,f and by arrows in b-d. Scale bars are 100 nm.

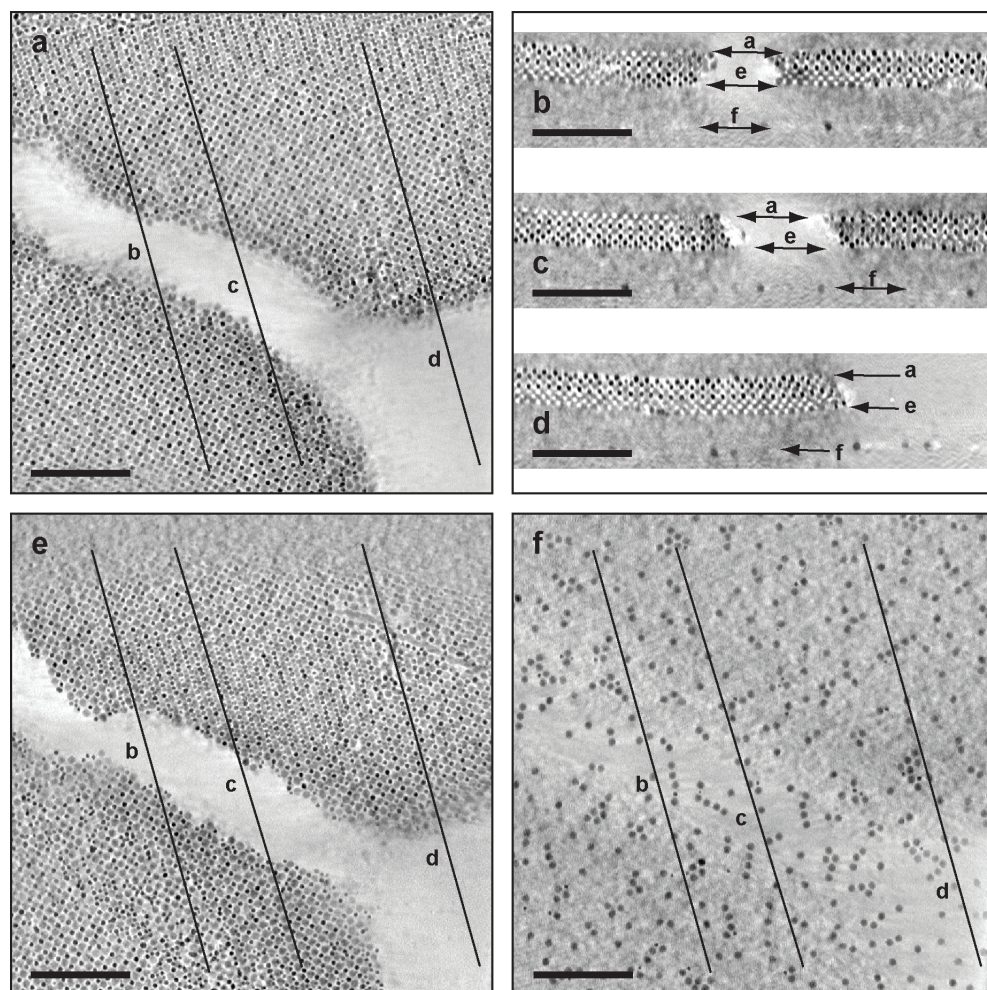


Figure A.6 Interface structure of AB superlattices consisting of PbSe and Au NCs. Numerical cross-sections parallel (a,e,f), and perpendicular (b-d) to the TEM support film illustrating the morphology of the suspension/air interface (a), suspension/support interface (e), and opposing side of TEM support film (f). The relative position of the sections are indicated by lines in a,e,f and by arrows in b-d. Scale bars are 100 nm.



List of publications

H. Friedrich, M. Paul, S. Guo, X. Pan, X. Bao, F. Schüth, P. E. de Jongh, A. J. Verkleij, K. P. de Jong *Quantifying the 3D Structure of Nanomaterials by Threshold-based Segmentation of Electron Tomograms*, in preparation.

H. Friedrich, C. J. Gommès, K. Overgaag, J. D. Meeldijk, W. H. Evers, B. de Nijs³, M. P. Boneschanscher, P. E. de Jongh, A. J. Verkleij, K. P. de Jong, A. van Blaaderen, D. Vanmaekelbergh *Quantitative structural analysis of binary nanocrystal superlattices by electron tomography*, Nano Letters **2009**, DOI: 10.1021/nl901212m.

H. Friedrich, P. E. de Jongh, A. J. Verkleij, K. P. de Jong *Electron Tomography for Heterogeneous Catalysts and Related Nanostructured Materials*, Chem. Rev. 109, **2009**, 1613-1629.

C. J. Gommès, H. Friedrich, M. Wolters, P. E. de Jongh, K. P. de Jong *Quantitative Characterization of Pore Corrugation in Ordered Mesoporous Materials Using Image Analysis of Electron Tomograms*, Chem. Mater. 21, **2009**, 1311-1317.

C. Vercaemst, H. Friedrich, P. E. de Jongh, A. V. Neimark, B. Goderis, F. Verpoort, P. van der Voort *Periodic Mesoporous Organosilicas Consisting of 3D Hexagonally Ordered Interconnected Globular Pores*, J. Phys. Chem. C 113, **2009**, 5556-5562.

J. R. A. Sietsma, H. Friedrich, A. Broersma, M. Versluijs-Helder, A. J. van Dillen, P. E. de Jongh, and K.P. de Jong *How nitric oxide affects the decomposition of supported nickel nitrate to arrive at highly dispersed catalysts*, J. Catal. 260, **2008**, 227-235.

E. Sacaliuc-Parvulescu, H. Friedrich, R. Palkovits, B. M. Weckhuysen, T. A. Nijhuis *Understanding the effect of postsynthesis ammonium treatment on the catalytic activity of Au/Ti-SBA-15 catalysts for the oxidation of propene*, J. Catal. 259, **2008**, 43-53.

J. Spinsby, H. Friedrich, P. R. Buseck *Volume and surface-area measurements using tomography, with an example from the Brenham pallasite meteorite*, Comp. Geosci. 34, **2008**, 1-7.

H. Friedrich, J. R. A. Sietsma, P. E. de Jongh, A. J. Verkleij, K. P. de Jong, *Measuring Location, Size, Distribution, and Loading of NiO Crystallites in Individual SBA-15 Pores by Electron Tomography*, J. Am. Chem. Soc. 129, **2007**, 10249-10254.

K. Adachi, S. H. Chung, H. Friedrich, P. R. Buseck *Fractal parameters of individual soot particles determined using electron tomography: Implications for optical properties* J.Geophys. Res. 112, **2007**, D14202.

K. P. de Jong, L. C. A. van den Oetelaar, E. T. C. Vogt, S. Eijsbouts, A. J. Koster, H. Friedrich, P. E. de Jongh *High-Resolution Electron Tomography Study of an Industrial Ni-Mo/ γ -Al₂O₃ Hydrotreating Catalyst*, J. Phys. Chem B. 110, **2006**, 10209-10212.

T. J. Zega, L. A. J. Garvie, I. Dodony, H. Friedrich, R. M. Stroud, P. R. Buseck *Polyhedral Serpentine Grains in CM Chondrites* Meteorit. Planet. Sci. 41, **2006**, 681-688.

L. van Poppel, H. Friedrich, J. Spinsby, P. R. Buseck *Electron Tomography of Nanoparticle Clusters and Implications for Atmospheric Lifetimes and Radiative Forcings of Soot*, Geophys. Res Lett. 32, **2005**, D24461

H. Friedrich, M. R. McCartney, P. R. Buseck *Comparison of intensity distributions in tomograms from BF TEM, ADF STEM, HAADF STEM, and calculated tilt series*, Ultramicroscopy 106, **2005**, 18-27.

H. Friedrich, B. Eienkel, L. Khouri, H. Lichte *Novel Concepts for Beam Splitters in Electron Holography*, Elektronenmikroskopie 23, **2003**, 8-12.

Acknowledgements

This PhD thesis has been made possible with the support of many people to whom I would like to express my gratitude in the following lines.

First of all, I would like to thank my advisors Krijn de Jong, Arie Verkleij, and Petra de Jongh; it has been a pleasure working with you. Krijn, you have been in the literal sense of the word a promoter, encouraging and guiding my scientific development over the past four years. Your broad scientific and industrial perspective on the field of catalysis as a whole has been a great stimulus. Arie, you provided a framework and integration into the electron microscopy unit, which has now become a second home to me. Petra, your enthusiasm and criticism have been a continuous motivation throughout the thesis.

Jelle Sietsma, Mariska Wolters, Johan den Breejen, and Tamara Eggenhuisen are kindly acknowledged for their skill in preparation and bulk characterization of the many samples that I could study from the field of model catalysts. The same holds true for Elena Parvulescu and Bert Weckhuysen whom I would like to thank for getting me involved in their research.

During the last four years I also had the opportunity to work with many colleagues from abroad. Not too surprisingly, one of the first joint projects led me back to Arizona State University and Peter Crozier who I would like to acknowledge for the environmental TEM experiments. I also owe gratitude to Cedric Gommès, who joined our group for one year as a research fellow of the University of Liege, for sharing his extensive knowledge on materials characterization, including image analysis of electron tomograms. Without your participation, chapter 6 would have been considerably different and not as invigorating as many of our lunch breaks.

Next, I would like to thank Carl Vercaemst and Pascal van der Voort from Gent University for a gratifying collaboration on the ordered mesoporous organosilicas. I also would like to acknowledge Michael Paul and Ferdi Schüth from the Max Planck Institute in Mühlheim for introducing me to a colloidal route of catalyst preparation and for providing the fascinating Au@zirconia catalyst. Furthermore, I would like to thank Shujing Guo, Xiulian Pan and Xinhe Bao from the Dalian Institute of Chemical Physics for the very intriguing and challenging Ru/carbon nanotube system. Carl, Michael, and Shujing, good luck with finishing your PhD thesis!

In addition, I would like to acknowledge two of our industrial partners, David Denley (Shell US, Houston) and Sander van Donk (Total, Feluy), for their continued interest in electron tomography. It was a pleasure working with you.

The most recent project (chapter 6 in this thesis) resulted from the joint effort of several groups from the Debye Institute for Nanomaterials Science of Utrecht University. I am grateful to Karin Overgaag, Wiel Evers, Bart de Nijs, Mark Boneschanscher, Alfons van Blaaderen, and Daniel Vanmaekelbergh for a stimulating collaboration on the truly exquisite binary nanoparticle superlattices.

A special thanks to Daniel Vanmaekelbergh and Alfons van Blaaderen for their contributions to the manuscript, critical comments and encouragement throughout this project. Here I would also like to thank the past and present members of the PhD commission of the Debye Institute for Nanomaterials Science (expressly Ingmar Swart, Dennis van Dorp, Ruud Bakker, Sandra Veen, Marijn Versteegh, Lukasz Karwacki, and Jan Hilhorst) for the excellent teamwork.

Harry Bitter and Frank de Groot are acknowledged for advancing my understanding of chemistry not only through the teaching assistant position that I shared with Niels Meis. I also would like to thank Tom Visser, Andrew Beale, Ad Mens, Vincent Koot, Marjan Versluijs-Helder, Fouad Soulimani, Ad van der Eerden, Dymph Seree and Monique Lamers for having an open ear to the many scientific and non-scientific matters that arise during a PhD. My past and present roommates Leendert Bezemer, Stefan van Dommele, Vendula Gabova, Regina Palkovits, Barbara Iacono, Lei Zhang, Maria Arias, Jovana Zecevic, and Mathijs Zandbergen, brought about a companionship and international flair that I am grateful for and that I am surely going to miss. By the same token, the regular outings with Leti, Lukasz, Andy, Matt, Ana, Philipp and many other members of the Inorganic Chemistry and Catalysis group have enriched the atmosphere with a warm and personal note.

The Electron Microscopy Unit of Utrecht University has over the past four years become a second home to me thanks to colleagues like Hans Meeldijk, John Geus, Willi Geerts, Misjael Lebbink, Theo van der Krift, Nuria Gimenez-Gil, Alya Yakushevskaya, Cveta Tomova, Chris Schneijdenberg, Elly van Donselaar, Wally Müller, and Bruno Humbel. Your expertise has unquestionably broadened my horizon as a microscopist.

At the end, I would like to acknowledge my family for their backing. Danke für die Geduld und Toleranz die Ihr mir entgegenbringt. Above all, a big kiss for Montse who has confidently shared with me the ups and downs of the past four years and hopefully many more to come.

Heiner Friedrich, August 2009.

Curriculum vitae

I received my MSc (2001) in Physics from the University of Dresden working on “Novel concepts for beam splitters in electron holography” at the Triebenberg Laboratory for High-Resolution Electron Microscopy and Holography. Between 2002 and 2005, I joined Prof. Peter Busecks group at Arizona State University (ASU) as research scientist to implement and apply electron tomography at the John M. Cowley Center for High-Resolution Electron Microscopy. Since 2005 my PhD research at Utrecht University under supervision of Prof. Krijn de Jong, Prof. Arie Verkleij, and Dr. Petra de Jongh has focussed on the quantitative three-dimensional characterization of nanostructured materials by electron tomography. The structures under investigation include silica, carbon nanotube, carbon nanofiber, and zirconia supported metal (oxide) particles; non-functionalized ordered mesoporous silica and organosilica; and more recently nanoparticle superlattices. The results which are described in part in this PhD thesis have been published in scientific journals, often in close contact with national and international collaborators. Besides my scientific occupation, I have been a member (2006-2008) and vice chairmen (2007-2008) of the PhD committee of the Debye Insitute for Nanomaterials Science, (co)organizing two symposia and (co)publishing two periodicals for the institute. As of September 2009 I will join the group of Dr. Nico Sommerdijk at the the Soft Matter CryoTEM Unit of Eindhoven University of Technology led by Prof. Bert de With.



“Everything that irritates us about others can lead us to an understanding of ourselves”

Carl Gustav Jung